Fabrication and Characterization of Porous Metal Emitters for Electrospray Applications

by

Robert S. Legge Jr.

Sc.B., Mechanical Engineering, Brown University, 2006

Submitted to the Department of Aeronautics and Astronautics
in partial fulfillment of the requirements for the degree of

Master of Science

at the

MASSACHUSETTS INSTITUTE OF TECHNOLOGY

June 2008

© Massachusetts Institute of Technology 2008. All rights reserved.

Author .....
Department of Aeronautics and Astronautics
May 18, 2008

Certified by .....
Prof. Paulo C. Lozano
Assistant Professor
Thesis Supervisor

Accepted by .....
Prof. David L. Darmofal
Associate Department Head/ Chair
Committee on Graduate Students

MASSACHUSETTS INSTITUTE OF TECHNOLOGY
AUG 0 1 2008
LIBRARIES

ARCHIVES

Fabrication and Characterization of Porous Metal Emitters for Electrospray Applications

by

Robert S. Legge Jr.

Sc.B., Mechanical Engineering, Brown University, 2006

Submitted to the Department of Aeronautics and Astronautics
on May 18, 2008, in partial fulfillment of the
requirements for the degree of
Master of Science

Abstract

Electrospray thrusters provide small, precise thrust with high power efficiencies and variable specific impulses from less than 1000s to over 4000s. The miniaturization and clustering of many emitters together is essential to increase the thrust density of electrospray devices in order to increase their domain of applicability in space. Electrospray emitter arrays have many advantages over existing electric propulsion devices including much lower mass per unit thrust and much lower volume per unit thrust than conventional ion and hall devices. Additionally, with emitter clustering, the thrust density can meet and even exceed that of hall or ion thrusters.

A method of micro-fabricating electrospray emitter arrays using modified conventional microfabrication technology is presented. The method is adaptable to different emitter materials and can be used to create ultra dense emitter arrays with microfabrication precision down to the micron level. One-dimensional linear emitter arrays with emitter separation as low as 500 μm have been fabricated out of porous tungsten and preliminary tests show that dense two-dimensional emitter arrays can be fabricated with emitter separations down to 300μm.

Experimental research that was conducted to characterize emitter array performance is also presented. Time of flight mass spectrometry was used to identify the emitted ion species from the device, which showed that the device operates in the ion emission regime. Current was collected as a function of applied voltage to show that the devices were able to operate with emitted current levels of 0.5 - 1.5 μA per emitter, even for dense arrays. Direct thrust measurements were performed to show that the amount of thrust attainable is on the order of 0.1 μN per μA of emitted current for extraction voltages of around 1900 V. A normalization scheme was implemented to compare performance of emitter arrays of different density and initial results from a numerical model has shown that the emitters might be limited by fluid transport.

Thesis Supervisor: Prof. Paulo C. Lozano
Title: Assistant Professor

Acknowledgments

There are many people that I would like to thank for their support in this phase of my life. First, I would like to thank my advisor and mentor, Professor Paulo Lozano, for the countless hours that he has spent working with me. His door was always open for me and he was always ready and willing to enthusiastically help me advance my research and life. I am continually in awe of your many achievements and zeal for learning.

I would like to thank my sources of funding and I am ever grateful for the financial support from the Karl Chang Innovation Fund and the Aero/Astro Fellowship awarded to me.

I would like to acknowledge and thank my colleagues and friends in the Space Propulsion Lab at MIT. Dan, Taki, Justin, and Tanya, thank you for being great officemates who were always up for grabbing some food and fooling around, and who kept me at least a little bit sane. Dan, I would like to thank you in particular for your help as well having a companion to commiserate with. Blaise, thanks for being a great mentor during my first year who showed me the ropes and taught me a lot about microfabrication, electrosprays and more...

I would also like to thank my girlfriend Sarah for her everlasting love and support during the last six months which included some of the most stressed out periods in my life. Thanks also for helping me proofread my thesis as well as giving me something perfect to think about. Robert and Anthony, thanks so much for being great roommates who are always caring and considerate. I always knew that when things got difficult at the lab, I could always have some fun at home.

Finally I want to thank my family, Katie, Dad, Mom, Gary, Lisa and Corey who have always been there for me. Thanks for setting me on the right path because I couldn't have gotten here without your support. Mom and Dad, the desire to make you proud has been one of the driving forces in my life. I want to thank my grandparents as well for always providing me with a great place to visit, whether it be the cottage or the beach in Venice. Oh, and Maximus, thanks for being soo cute.

Contents

1 Introduction **21**

1.1 Introduction to Electrospray Sources 21

1.1.1 Electrospray History 22

1.1.2 Electrospray Applications 23

1.2 Overview of Space Propulsion 23

1.2.1 Rocket Fundamentals 23

1.2.2 Chemical Thrusters 25

1.2.3 Electrically Augmented Thrusters 26

1.2.4 Electric Thrusters 26

1.3 The Case for Electrospray Arrays 28

1.3.1 Electrospray Clustering Model 28

1.3.2 Specific Area Comparison 31

1.3.3 Specific Mass and Specific Volume Comparison 34

1.4 Electrospray Thruster Applications 38

2 Electrospray Characteristics **41**

2.1 Basic Physics 41

2.1.1 Surface Charge and Relaxation Time 41

2.1.2 Taylor Cone Formation 42

2.1.3 Emitted Current and Starting Voltage 44

2.1.4 Field Evaporation of Ions 46

2.1.5 Electrospray Efficiency 48

2.1.6 Droplet vs. Ion Emission 50

2.2 Types of Electrospray Emitters 52
2.3 Fluid Transport in Porous Emitters 55
2.3.1 Darcy's Law and Fluid Conductivity 56
2.3.2 The Discretization of Darcy's Law 56
2.3.3 Model Geometry and Boundary Conditions 58
2.3.4 Initial Model Results 62
2.4 Ionic Liquid Properties 64

3 Fabrication Technology **67**
3.1 Basic Micromachining 67
3.1.1 Adding Material 69
3.1.2 Removing Material 70
3.1.3 Transferring Geometry 71
3.1.4 Bonding Components 71
3.2 Electrochemical Etching Theory 72
3.2.1 Electrochemical Etching Kinetics 75
3.2.2 Electrochemical Etching of Tungsten 76
3.2.3 Electrochemical Etching of Titanium 77

4 Emitter Fabrication **79**
4.1 Previous Work 79
4.2 Emitter Material 81
4.3 Fabrication Considerations 82
4.4 Fabrication Process 82
4.4.1 Blocking the Porosity 83
4.4.2 Applying the Mask 85
4.4.3 Patterning the Mask 86
4.4.4 Etching Tungsten 86
4.5 Fabrication Refinements 87
4.6 Fabrication Examples 91
4.6.1 Linear Arrays of Different Packing Density 91

4.6.2 Linear Array Thruster 91

5 Experimental Techniques **95**

5.1 Time-of-Flight Mass Spectrometry 95

5.2 Emitted Current Measurements 100

5.3 Thrust Measurements 102

5.4 Vacuum System and Lab Facilities 103

5.5 High Voltage Current Measurements 104

6 Experimental Results **107**

6.1 Experimental Overview 107

6.2 Initial Emitter Results 107

6.2.1 Emitted Current 107

6.2.2 Time of Flight 108

6.3 One-Dimensional Demonstration Thruster 112

6.3.1 Thrust and Current Measurements 112

6.4 One-Dimensional Packing Density 114

6.4.1 1D Emitter Array Performance 116

6.4.2 Normalization of Data 116

6.4.3 Long Duration Testing 121

7 Conclusions and Future Work **123**

7.1 Two Dimensional Arrays 123

7.1.1 Emitter Array Fabrication 124

7.1.2 Initial Extractor Fabrication 127

7.1.3 Thruster Concept 128

7.2 Recommendations for Future Work 131

7.2.1 Emitter Array Fabrication 131

7.2.2 Other Suggested Research Areas 135

7.3 Conclusion 135

List of Figures

1-1 Capillary Electrospray Emitter Setup 22

1-2 Rocket Technologies 24

1-3 Arcjet Schematic 26

1-4 Ion Engine Schematic 27

1-5 Hall Thruster Schematic 28

1-6 2D Emitter Geometry 29

1-7 Emitter-Extractor Geometry 30

1-8 Space Charge Limited Current Density 33

1-9 Specific Area vs Emitter Separation 34

1-10 Simplified Thruster Geometry 34

1-11 Specific Mass vs Emitter Separation 36

1-12 Specific Volume vs Emitter Separation 36

2-1 Taylor Cone Schematic 43

2-2 Emitter Starting Voltage Modeled in Prolate Spheroidal Coordinates 44

2-3 Image Charge Model to Model Ion Evaporation 47

2-4 Polydispersive Efficiency of EMI-BF_4 and EMI-IM 51

2-5 Operational Performance in the Mixed Ion-Droplet Regime 52

2-6 Electrospray Emitter Types 53

2-7 Micro Capillary Electrospray Device 54

2-8 Finite Difference Computational Domain 55

2-9 Intrinsic Permeability as a Function of Average Pore Diameter 57

2-10 Numerical Stencil Used to Model Flow 58

2-11 Numerical Domain and Boundary Conditions 59
2-12 Schematic of Fluid Flow Driven by Capillary Forces 59
2-13 Critical Radius as a Function of Emitted Current 61
2-14 Schematic of Fluid Flow Driven by Capillary Forces and Dynamic Pressure 62
2-15 Pressure Drop Across Porous Emitter and Driving Pressure vs. Emitted Current 63
2-16 Maximum Supported Current as a Function of Average Pore Diameter 64
2-17 Conductivity of Various Ionic Liquids as a Function of Temperature . 66
2-18 Dynamic Viscosity of Various Ionic Liquids as a Function of Temperature 66

3-1 Sample MEMS Devices 68
3-2 Etch Shape Evolution 70
3-3 Photolithography Process 72
3-4 Electrochemical Cell Diagram 73
3-5 Electrochemical Shape Evolution 76

4-1 Needle Emitter Arrays 79
4-2 Sheet Emitter Arrays 80
4-3 Porous Tungsten Samples 81
4-4 Fabrication Process Overview 83
4-5 Blocking the Porosity 84
4-6 Applying the Polyimide Layer 85
4-7 Patterning the Polyimide 86
4-8 Etching Tungsten 87
4-9 Emitter Fabrication Pictures 88
4-10 Polyimide Mask Problems 90
4-11 Electrolyte Flow Etch Setup 91
4-12 1D Emitter Arrays with Varying Emitter Separation 92
4-13 Linear Array Thruster Assembly 93
4-14 49 Emitter Electrospray Thruster 94

5-1 Single Gate Time-of-Flight 96
5-2 Oscilloscope TOF Display for Steady State 97
5-3 Sample TOF Experimental Results 98
5-4 Time of Flight with Droplets 99
5-5 Current Measuring Setup 100
5-6 Sample Experimental Voltage Sweep 101
5-7 Averaging Current Measurements 102
5-8 SPL Vacuum Chamber and Electronics 103
5-9 High Voltage Current Measuring Device Schematic 105
5-10 High Voltage Current Measuring Device PCB 105
5-11 Gain Response for the HV Converter 106

6-1 Current vs. Voltage Plots for Small Emitter Arrays 108
6-2 Time of Flight Results for EMI-BF_4 109
6-3 TOF Signal Spread for EMI-BF_4 in the Negative Mode 111
6-4 TOF Signal Spread for EMI-BF_4 in the Positive Mode 111
6-5 Time of Flight Results for EMI-IM 112
6-6 TOF Signal Spread for EMI-IM in the Negative Mode 113
6-7 Thrust Measurements for a 49 Emitter Array 113
6-8 Current vs. Applied Voltage for a 49 Emitter Array 115
6-9 Specific Impulse for a 49 Emitter Array 116
6-10 Current vs. Applied Voltage for 1D Linear Emitter Arrays 117
6-11 Emitted Current Normalization Parameters 118
6-12 Reduction of Emitter Tip Electric Field vs Emitter Separation 119
6-13 Normalized data showing the three emitter arrays with differing packing density 120
6-14 Long Duration Emitter Test Current Profile 121
6-15 Long Duration Emitter Test with Emitted Current Decay 122

7-1 2D Emitter Array Tungsten Media 124
7-2 Transparency Masks for a Two Dimensional Emitter Array 125

7-3 Polyimide Masking Layer for a Two Dimensional Emitter Array . . . 125
7-4 Polyimide Masking Layer During Etch 126
7-5 2D Emitter Shape Evolution 126
7-6 Fabricated 2D Emitter Arrays 127
7-7 Transparency Masks for Slit and Hole Extractors 128
7-8 Polyimide Masks For Tungsten Extractors 128
7-9 Initial Etched Extractor Samples 129
7-10 5984 Emitter Thruster Concept 130
7-11 Two-Dimensional Array Showing Polyimide Contamination 132
7-12 Vapor Pressure of Iodine as a Function of Temperature 133
7-13 Modified Sintering Process 134
7-14 Two-Dimensional Array Showing a Non-Uniform Etch 134

List of Tables

1.1 Comparison of Physical Thruster Characteristics 33
1.2 Clustering Performance Comparison 37
1.3 Clustering Performance Comparison with Titanium 38

2.1 Beam Ions for EMI-BF_4 and EMI-IM 50
2.2 Polydispersive Calculation Input Parameters 50

3.1 Microfabrication Milestones 68
3.2 Standard Electrode Potentials 73
3.3 Titanium Etching Chemistries 77

4.1 1D Emitter Packing Array Characteristics 92

5.1 SPL Electronic Equipment 104
5.2 High Voltage Current Measurement Ranges 106

6.1 Emitted Beam Composition for EMI-BF_4 109
6.2 Emitted Beam Composition for EMI-IM 112
6.3 1D Emitter Performance Characteristics 116
6.4 1D Emitter Properties and Non-Dimensionalization Parameters . . . 120

Nomenclature

Acronyms

DRIE Deep Reactive Ion Etching

FWHM Full Width Half Max

HVPS High Voltage Power Supply

IL Ionic Liquid

MEMS Micro electro-mechanical systems

NHE Normal Hydrogen Electrode

PCS Power Conditioning System

PR Photoresist

TOF Time Of Flight Mass Spectrometry

Constants

α_T	Taylor Cone Half Angle	49.29 degrees
ϵ_0	Permittivity of Free Space	8.854187e(-12) $F\,m^{-1}$
F	Faraday Constant	96485.3415 $C\,mol^{-1}$
g_0	Gravitation Acceleration	9.81 $m\,s^{-2}$
h_p	Planck's Constant	6.625e-34 $J\,s$
k	Boltzmann Constant	1.3806504 x 10^{-23} J K^{-1}

Variables

ΔG	Free Energy of Solvation	J
ΔP_{cap}	Capillary Pressure Drop	Pa
ΔP_{dyn}	Dynamic Pressure Drop	Pa
Δt	TOF Transit Time	s
$\dot{m}$	Mass Flowrate	$kg\,s^{-1}$
$\hat{q}$	Flow Density	$m\,s^{-1}$

$\widetilde{F}$	Thrust Density	$N\,m^{-2}$
$\widetilde{N}$	Emitter Density	m^{-2}
$\widetilde{i}_n$	Normal Current Density	$C\,m^{-2}\,s^{-1}$
A_{ch}	Characteristic Area	m^2
c	Exit Velocity	$m\,s^{-1}$
D	Diffusivity	$m^2\,s^{-1}$
d	Emitter Spacing	m
d_e	Grid Spacing	m
E_n	Normal Electric Field	$V\,m^{-1}$
F	Force	N
f	Ion Current Fraction	
f_m	Ion Mass Fraction	
G	Gibbs Free Energy	$J\,mol^{-1}$
H	Hydraulic Head	m
h	Emitter - Extractor Distance	m
I^*	Characteristic Current	$C\,s^{-1}$
I_B	Beam Current	$C\,s^{-1}$
I_T	Total Current Through Power Supply	$C\,s^{-1}$
I_{SP}	Specific Impulse	s
I_t	Total Impulse	$N\,s$
j	Current Density	$C\,s^{-1}\,m^{-2}$
K	Hydraulic Conductivity	$m\,s^{-1}$
L	Emitter Length	m
M	Molecular Weight	$g\,mol^{-1}$
m_i	Ion Mass	kg
m_p	Propellant Mass	kg
n	Number of Moles	
n_v	Valence of Dissolution	
P	Pressure	Pa
Q	Flowrate	$m^3\,s^{-1}$
q	Charge	C

Q_0	Reaction Quotient	
r_1	Critical Taylor Cone Radius	m
R_c	Radius of Curvature	m
r_t	Ionic Emission Area Radius	m
V^*	Characteristic Voltage	V
V_a	Accelerating Voltage	V
V_s	Emitter Starting Voltage	V
V_{op}	Emitter Operating Voltage	V
χ	Emitter Packing Density	$\# mm^{-1}$
δ	Etch Rate	$m\,s^{-1}$
η_E	Electrical Efficiency	
η_i	Ionization Efficiency	
η_p	Polydispersive Efficiency	
η_T	Total Efficiency	
η_{tr}	Transmission Efficiency	
γ	Surface Tension	$N\,m^{-1}$
κ	Curvature	m^{-1}
κ	Electrical Conductivity	$Si\,m^{-1}$
κ	Intrinsic Permeability	m^2
μ	Dynamic Viscosity	Pas
μ	Mobility	$m^2\,V^{-1}\,s^{-1}$
ϕ	Electric Potential	V
ϕ_a	Accelerating Potential	V
ϕ_B	Beam Potential	V
ψ	Clustering Field Reduction Fraction	
σ_f	Free Surface Charge Density	$C\,m^{-2}$
θ	Electrochemical Current Efficiency	
θ_c	Contact Angle	rad
ξ	Specific Charge Ratio	
ϵ	Dielectric Constant	

Chapter 1

Introduction

1.1 Introduction to Electrospray Sources

A simple capillary electrospray emitter setup is shown in Figure 1-1. An applied potential between an extractor electrode and conductive liquid inside a capillary causes a liquid meniscus at the end of the capillary to deform into a conical shape. This structure is called a Taylor cone in honor of G.I. Taylor who first derived a mathematical model to describe the phenomenon in 1964[46] for certain conditions. The apex of the cone emits a jet of charged liquid which breaks up into charged droplets. These droplets are then accelerated by means of an electrostatic force to a final exit velocity. In thruster applications, the electrostatic force applied to the charged droplets is equal but opposite to the resulting thrust felt by the thruster device. In cases where the local electric field at the tip of the Taylor cone is high enough, the electrostatic pull overcomes the ion surface energy and ions are extracted directly from the liquid. This causes the ions to be accelerated through the potential and achieve a much higher exit velocity than charged droplets, which is a more efficient propulsion system in terms of propellant consumption, albeit at the expense of lower thrust. A more detailed analysis of the physics behind electrospray operation can be found in Section 2.1.

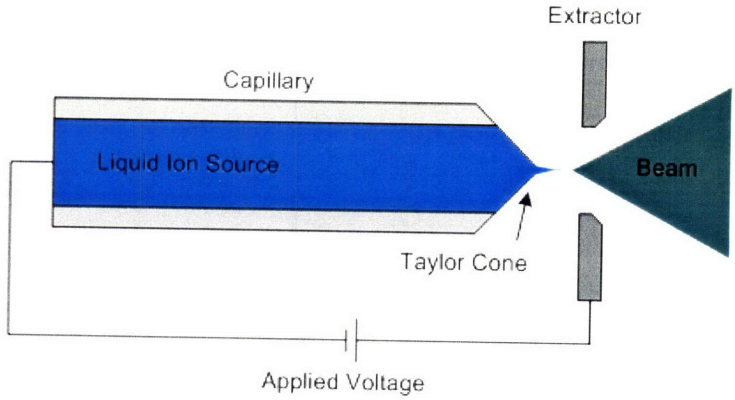

Figure 1-1: Capillary Electrospray Emitter Setup

1.1.1 Electrospray History

Interest in electrospray sources originated with the work of John Zeleny in 1914. He studied the visual formation of cone-jet structures using a diluted solution of hydrochloric acid[48]. However, it was not until 1964 that G.I. Taylor developed a theoretical model to explain how the cone-jet forms and operates[46]. He modeled the cone as a balance between electrical traction forces caused by the external electric field and surface tension forces of the liquid. At about this time, interest in using electrosprays as an alternative to ion engines for in-space propulsion started to pick up because of their ability to create droplets with a large mass to charge ratio[6]. This is appealing because it is known that, by increasing the particle mass, you could effectively increase the thrust density of the devices. Back then, the mass-to-charge ratios were so large that the resulting acceleration voltages turned out to be rather large (up to 100 kV[36]) with performance much less than ion engines[37]. Because of this, thruster research largely went dormant. In the late 1980's, John Fenn conducted research involving the mass spectrometry of biomasses, a effort that won him the Nobel Prize in Chemistry in 2002. This event, combined with the first synthesis of new ionic liquids [ILs] in the late 1990's, ushered in new interest in electrospray propulsion research. Ionic Liquids are molten salts at room temperature and have been shown to be able to emit in the purely ionic regime for extraction voltages well under 2 kV[42,

34]. More information about IL's can be found in Section 2.4. Additionally, new advances in emitter geometry have allowed for devices to use passively fed externally wetted as well as emitters fabricated from porous materials[24]. Porous materials allow for higher flowrates and thrust than externally wetted devices. Current advances in microfabrication technology allow for the miniaturization of individual emitters and the close packing of emitters to increase thrust density[30, 24].

1.1.2 Electrospray Applications

Electrospray sources are used for a variety of non-space applications, including: mass spectrometry for biological molecules[12], micro scale atomizers for fuel injection[9, 10], and even sources of electrostatically charged droplets for thin film deposition and painting[16]. Electrospray technology is also appealing as a source of ion beams for both micromachining[19] and molecular imaging applications[11]. In addition, electrospray sources have been used recently in electrospinning applications, where they can create uniform fibers of nano-scale dimensions[44].

1.2 Overview of Space Propulsion

1.2.1 Rocket Fundamentals

Rockets provide propulsive force through the acceleration of stored propellant. This is different than jet propulsion where part of the propellant (the oxidizer) is taken from the atmosphere. Rockets are not only required for launching spacecraft into orbit, but for a wide variety of in-space propulsive tasks including: orbital maneuvers, north-south station keeping, orbit altitude maintenance, and interplanetary travel. There are two primary types of rockets used for in-space propulsion applications, which include chemical rockets where the propulsive power is derived solely from chemical energy stored in the propellant, and electrical rockets where the propulsive power is generated by an electric power source. There are also a few devices which are primarily chemical in nature but utilize electrical power to augment their performance.

Figure 1-2 shows the various technologies currently available for in-space propulsion.

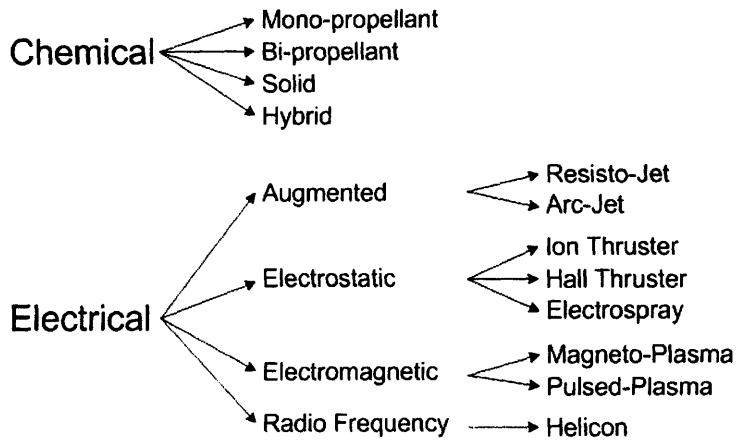

Figure 1-2: Rocket Technologies

Rocket performance in terms of propellant consumption efficiency is measured in terms of specific impulse [I_{SP}], which is a figure of merit with units of seconds. I_{SP} is defined as the total impulse per unit weight of propellant[45] and can be written as:

$$I_{SP} = \frac{\int_0^t F\,dt}{g_0 \int \dot{m}\,dt} \tag{1.1}$$

For the special case in which the propellant mass flow rate and thrust are constant Equation 1.1 is written as a function of the total impulse and total propellant mass:

$$I_{SP} = \frac{I_t}{m_p g_0} \tag{1.2}$$

The thrust of a rocket is equal to the change in momentum of the spent propellant in the frame of reference of the rocket, and is expressed as the propellant mass flowrate times the effective exhaust velocity. This allows us to relate the specific impulse to the effective exhaust velocity as follows:

$$I_{SP} = \frac{c}{g_0} \tag{1.3}$$

The following sections give a brief overview of some technologies for in space propulsion. More detailed information is available elsewhere[45, 15].

1.2.2 Chemical Thrusters

Chemical rockets can be broken down into a number of differing technologies, each with their own specific requirements and suited purposes. Cold gas thrusters accelerate an inert pressurized gas through a nozzle to produce thrust. While they do not use stored chemical energy to produce thrust we will include them in this section. They are specifically suited to small satellites with modest ΔV requirements. They are very cheap to construct and test, and offer simplified design and operation. This is at the expense of performance, which in terms of effective exhaust velocity, is from 300 to 700 m/s [I_{SP} = 30-70s]. Monopropellant thrusters use a single fuel that is decomposed in a catalyst bed to provide a high temperature gas which is then accelerated in a nozzle to exit speeds from 1500 m/s to over 2250 m/s [I_{SP} = 150-220s]. Typical propellants include nearly pure Hydrogen Peroxide and Hydrazine. Bipropellant thrusters combine fuel with oxidizer to release bond energy to heat up the gas which is then accelerated in a nozzle. Performance of these rockets is, in general, greater than the performance of monopropellants, but the devices are considerably more complex and are therefore suited to larger rockets, although this may depend on the pressurization system employed (gas pressurized or turbomachinery pressurized). The space shuttle main engine is a bipropellant rocket that runs on LOX and LH2 and achieves exit velocities of up to 4500 m/s [I_{SP} = 455 s]. Solid motors operate by burning a solid propellant mixed with oxidizer and other additives contained within a lightweight casing. These hot and pressurized byproducts are then accelerated through a nozzle to exit speeds from 2800 to 3000 m/s [I_{SP} = 280-300s]. Once started up, the motor cannot be shut down until complete depletion of the propellant, and the only way to throttle the motor is by molding the solid propellant so that the burning area varies with time. They can, however, give a large amount of thrust which is important in booster maneuvers.

1.2.3 Electrically Augmented Thrusters

Electrically augmented thrusters are essentially chemical (or cold gas) thrusters where energy is added to the propellant stream just prior to the expansion to enhance performance. There are two main types of these thrusters including resistojets and arcjets. The resistojet is simply a cold gas or monopropellant thruster in which an electric heating element is used to increase the temperature of the gas, thus decreasing the flowrate at a constant pressure. The addition of thermal energy into the propellant ultimately increases specific impulse. The limiting factor in the operation of resistojets is that the temperature of the chamber is limited by material considerations. It has been shown, however, that 40 percent increases of specific impulse are possible without adding much complexity[37]. Arcjets get around the materials limitation by directly heating the gas stream. The basic setup is shown in Figure 1-3 and consists of a pointed cathode located coaxially in the fluid flow just before the nozzle throat. A voltage is applied between the cathode and the nozzle so that an arc forms in the middle of the nozzle throat. Since there is virtually no fluid flow though the superheated arc this effectively reduces the total mass flowrate while maintaining the same exit area, which therefore increases the specific impulse. Performance with hydrogen can be greater than 1000 s[36].

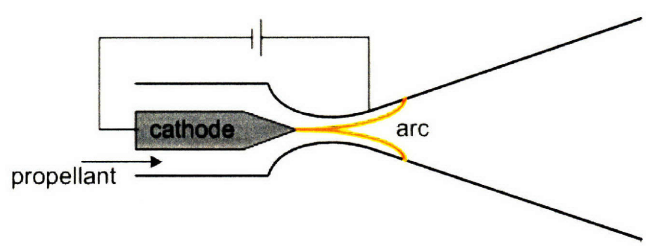

Figure 1-3: Arcjet Schematic

1.2.4 Electric Thrusters

The two categories for electric thrusters are electrostatic thrusters and magnetic thrusters. Electrostatic thrusters accelerate charged masses through an electrical

potential to produce thrust. Three primary classes of electrostatic thrusters exist: ion thrusters, hall thrusters and electrospray thrusters. In an ion thruster, shown in Figure 1-4, the gaseous propellant (usually argon or xenon) is ionized by electron bombardment or RF. Electrons are emitted from a cathode and are confined by magnetic fields to increase the residence time in the ionization region. After ionization, some ions migrate to the acceleration grids and fall through the potential drop to produce thrust. Ion engines typically have specific impulses in the 3000 to 4000 s range with power efficiencies as high as 75 percent.

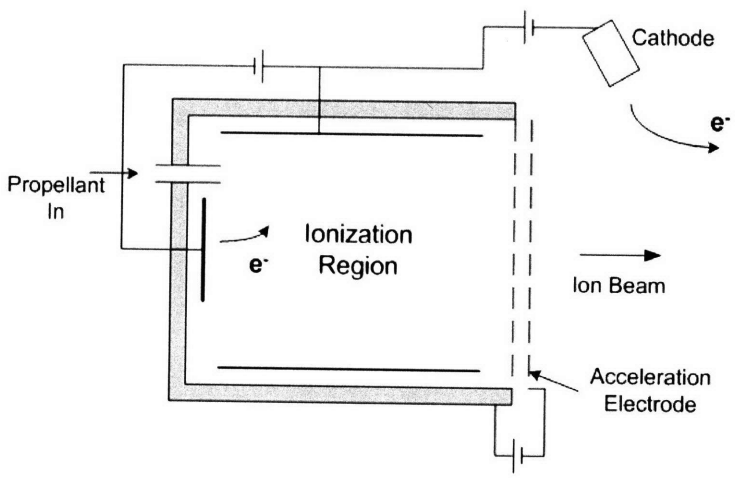

Figure 1-4: Ion Engine Schematic

A hall thruster operates slightly differently than an ion thruster. In a hall thruster, as shown in Figure 1-5 with axial symmetry, a neutral gas (usually argon or xenon) is injected into an annular chamber. It is ionized by electrons executing an annular $\vec{E}$ x $\vec{B}$ drift. The ions then axially accelerate through an electric potential between the external cathode and an anode near the beginning of the annular chamber. A hall thruster typically has specific impulses in the 1500 to 2500 s range and has an overall power efficiency of up to 60 percent.

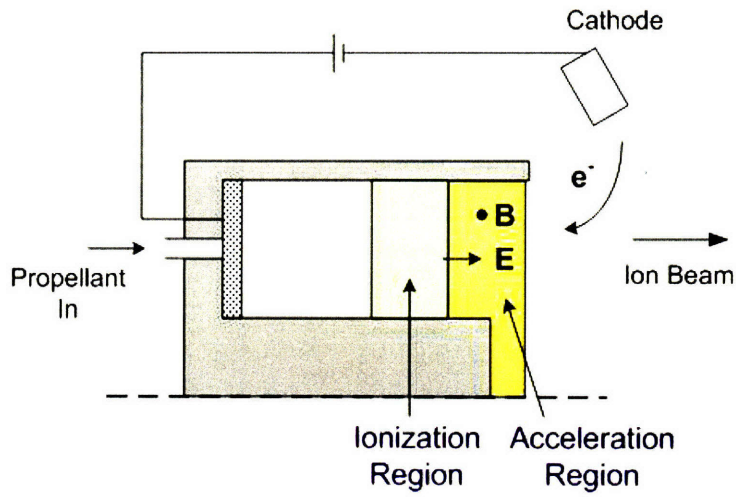

Figure 1-5: Hall Thruster Schematic

1.3 The Case for Electrospray Arrays

Conventional electrospray thrusters occupy a unique position among electric propulsion devices by offering thrust down to the nN level, with unique precision, high operational efficiency and specific impulse. One way to increase thrust and improve other figures of merit is to pack many individual emitters into arrays. The following section will construct a model to analyze the effect of clustering on electrospray thruster performance and to compare the performance with other electric propulsion technologies. Electrospray thrusters have great potential on three figures of merit including: specific area $[\frac{m^2}{N}]$, specific mass $[\frac{kg}{N}]$, and specific volume $[\frac{m^3}{N}]$.

1.3.1 Electrospray Clustering Model

The model will be built around a two-dimensional electrospray emitter array comprised of many conical emitters. The main components in the thruster are: the emitter array, the extractor plate, and the porous fuel tank. The emitter arrays and fuel tank are fabricated out of porous tungsten while the extractor is made of non-porous tungsten. For this model, it is assumed that the extractor is attached and aligned to the emitter array using a lightweight holder which on first pass will roughly

doubles the overall thruster weight and volume.

Several interactions must be lumped together to sufficiently model the effect that emitter clustering has on performance. First, it has been experimentally observed that small emitters will emit the same current as larger emitters given the same extraction voltage. This is true because the geometry at the tip is nearly independent of the overall, macroscale emitter geometry, and stays constant with miniaturization. Experimental data shows that the emitted current is on the order of 0.2-2 uA per emitter under normal operating conditions.

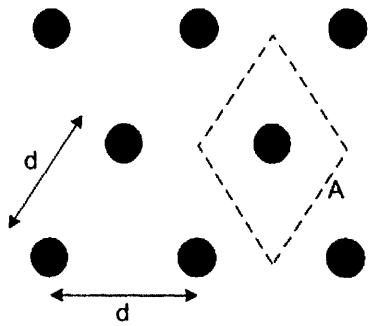

Figure 1-6: 2D Emitter Spacing

In a two dimensional emitter array with a triangular packing and emitter separation d, as shown in Figure 1-6, a relation for the emitter density $[\widetilde{N}]$ is written as a function of the effective emitter area A, which is then written as a function of the emitter separation distance alone.

$$\widetilde{N} = \frac{1}{A} = \frac{2}{d^2\sqrt{3}} \tag{1.4}$$

Since the current per emitter stays constant through the clustering process, the current density $[j]$ will scale proportional with the emitter density.

$$\widetilde{j} = \left(\frac{2}{d^2\sqrt{3}}\right) I_{Tip} \tag{1.5}$$

Where I_{Tip} is the current emitted from a single emitter. Second, as the distance

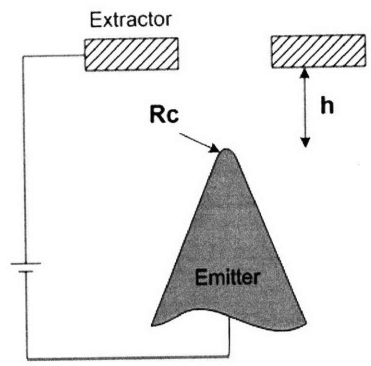

Figure 1-7: Emitter-Extractor Spacing Geometry

between the extractor and the emitters is reduced, the corresponding extraction voltage will be reduced. The starting voltage, or minimum voltage needed to see an appreciable amount of current emitted, is given in the following relation and is dependent on the liquid surface tension (γ), the emitter-extractor distance (h), and the radius of curvature of the emitter tip (R_c) (shown in Figure 1-7).[36]:

$$V_s = \sqrt{\frac{\gamma R_c}{\epsilon_0}} \ln\left(\frac{4h}{R_c}\right) \tag{1.6}$$

To simplify the model and link the starting voltage to the emitter separation distance the approximation is made that the emitter-extractor distance [h] is related to the emitter separation, and that the operational voltage is roughly 1.5 times higher than the starting voltage. We also specify that the emitter-extractor distance should never allow for emitted beam impingement caused by a beam spreading angle of θ_B. As the emitters become smaller, we want the extractor to be closer to the emitter tips to reduce the effect of neighboring emitters on emitter tip electric field. This is to preserve the field strength at the tip without having to apply very large extractor voltages.

$$h = min\left(0.4d, \frac{D/2}{\tan\theta_B}\right)$$
$$V_{op} = 1.5V_s$$

To find how the thrust density [$\widetilde{F}$] scales with the emitter separation distance,

it is necessary to link the emitted current to the mass flow rate using the following relation where c is the exit speed of the ions (found through an ion energy balance). This balance assumes that only monodisperse ions are emitted, with energies centered around the operating voltage (V_{op}).

$$\tilde{F} = \frac{\dot{m}c}{A} = j\sqrt{\frac{2V_{op}}{q/m_i}} \tag{1.7}$$

1.3.2 Specific Area Comparison

As was illustrated earlier, both the hall thruster and the ion engine derive their thrust from electrostatic acceleration and primarily rely on ionized propellant in the gaseous phase. This places a limit on the amount of miniaturization possible for a given device due to the increased losses associated with confining plasma to a smaller volume.

In the ion engine, the presence of a non-neutral acceleration region limits the maximum current density. This maximum current density allowed due to space charge effects is modeled by the Child-Langmuir Law. The density limit as derived in the one dimensional case, for a given propellant, is a function of only the acceleration voltage (V_a) and the electrode spacing (d_e):

$$j = \frac{4}{9}\epsilon_0\sqrt{\frac{2q}{m_i}}\frac{V_a^{3/2}}{d_e^2} \tag{1.8}$$

The appearance of a maximum current density implies that there must also be a maximum obtainable thrust density. The thrust density can then be calculated for any given current density and is a function of the acceleration voltage and the electrode spacing.

$$\tilde{F} = \frac{8}{9}\epsilon_0\frac{V_a^2}{d_e^2} \tag{1.9}$$

This relation states that there is a maximum allowable thrust density for any given geometry. In the case of a gridded ion engine, the minimum electrode spacing is on the order of 0.5 to 1.0mm[36], due to fabrication considerations, and the voltages are on the order of 1-5 kV, which gives maximum thrust densities on the order of 200 N/m^2. This estimate is far too high in comparison to actual ion engine performance.

For hall thrusters, there is no space charge limitation due to the quasi-neutrality of the plasma. This allows the thrust density to be increased indefinitely barring other limiting mechanisms. In practice, as the thrust density is increased by increasing the flow rate of propellant, the efficiency of the system decreases and the potential for physically damaging ion sputtering increases. The efficiency decreases due to the elevated rate of electron collisions allowing for higher diffusion rates to the anode as well as the greater probability that either ions or electrons will be lost to the channel walls.

Electrospray thrusters do not suffer from the consequences of having gaseous plasma and they are not significantly hindered by space charge, even though it is still present. The space charge limitation is overcome by the fact that the emitter to extractor spacing can be very small for electrospray devices. In practice, we see at most 10 μA per emitter for an operating voltage of 2000 V and an emitter to extractor spacing of 400 μm. If we say that this emitter occupies a frontal area of 1.0 x 1.0 mm, then we arrive at a thrust density of 10 A/m^2. For comparison, the maximum current allowed by the space charge calculation is nearly 200 A/m^2, showing that we are far under this limit. If we use the electrospray miniaturization model to calculate the space charge limited thrust and the expected emitted thrust for an operating voltage of 1.5 times the starting voltage, we clearly see that we are not limited by space charge effects, as is shown in Figure 1-8.

Using the following properties for the ionic liquid $EMI - BF_4$: q/m = 500,000, $\gamma = 0.051$ N/m, and for some typical emitter geometry, $R_c = 20$ μm and I = 1 μA/emitter of extracted current, then we clearly see the effect of clustering on thrust density for small emitter spacing. For comparison to existing electrostatic thruster technologies, two mature thrusters have been chosen including NASA's Evolutionary

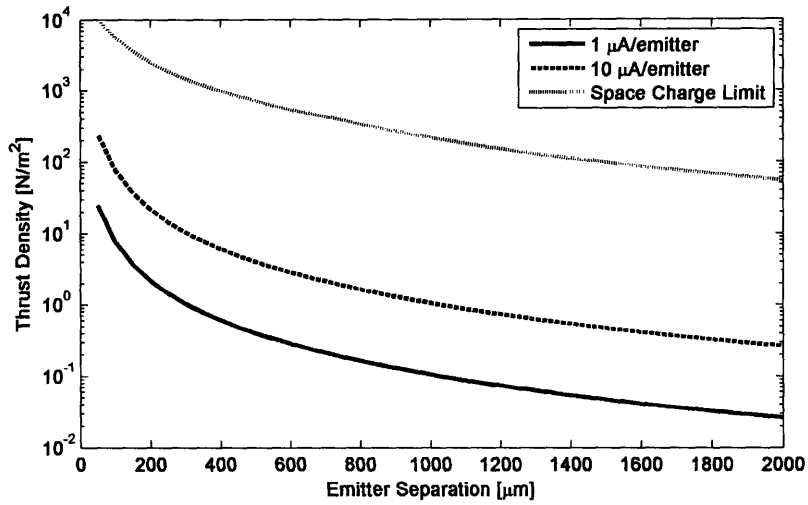

Figure 1-8: Space Charge Limited Current Density

	Thrust N	Mass kg	Volume m^3	Frontal Area m^2
BHT-1000 (Hall)	0.088	5.9	0.0015	0.062
NEXT (ION)	0.237	12	0.0251	0.126

Table 1.1: Comparison of Physical Thruster Characteristics

Xenon Thruster (NEXT) and Busek's BHT-1000 hall Thruster. Table 1.1 shows their nominal operating parameters.

If we plot the specific area, which is defined as the inverse of the thrust density, vs. the emitter separation as shown in Figure 1-9, we see that as the emitter separation decreases, the specific area decreases significantly. The specific areas of the BHT-1000 hall thruster and the NEXT ion engine are also plotted for comparison. With emitter separation distances of around 200 - 250 μm the electrospray specific area becomes comparable to that of the ion engine and hall thruster. The ability to decrease the specific area is one of the primary advantages of miniaturized electrospray array thrusters. Current research indicates that an emitter spacing of 300 μm can be achieved, and that further miniaturization is possible, see Section 7.1.

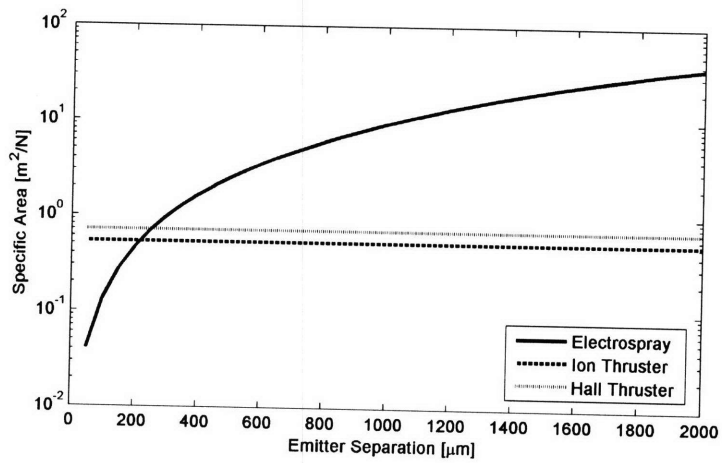

Figure 1-9: Effect of Emitter Separation on Specific Area

1.3.3 Specific Mass and Specific Volume Comparison

The specific mass and specific volume figures of merit are even more important than specific area in space applications, where both mass and volume are at a premium. If we use the model, along with a few more geometrical design values depicted in Figure 1-10, we can generate another comparison with conventional technologies.

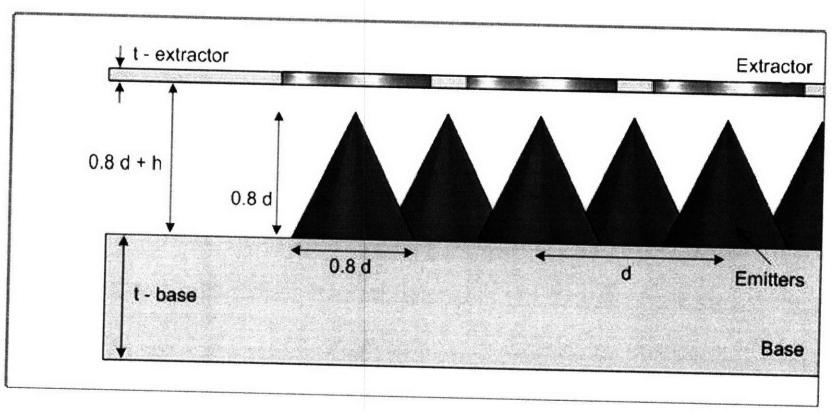

Figure 1-10: Simplified Thruster Geometry

We can calculate the mass per unit frontal area through the following formula where α_{base} is the void fraction of the porous metal, α_{ext} is the void fraction of the extractor, t_{base} is the thickness of the porous metal base, t_{ext} is the thickness of the extractor, and and all the materials used are tungsten.

$$
\begin{aligned}
\frac{m}{A} &= (BaseMass + ExtractorMass + EmitterMass)/A \\
&= \rho\left(\alpha_{base}t_{base} + \alpha_{ext}t_{ext} + \alpha_{emitter}\widetilde{N}V_{cone}\right) \qquad (1.10) \\
&= \rho\left(\alpha_{base}t_{base} + \alpha_{ext}t_{ext} + \alpha_{emitter}\frac{\pi\,(0.8)^3)}{6\sin\frac{\pi}{3}}d\right) \qquad (1.11)
\end{aligned}
$$

If we assume that the emitter rests on a 0.5 mm thick base of porous tungsten (0.7 percent solid) and that the extractor is made out of 0.05 mm thick solid tungsten sheet with a 75 percent solid fraction. Then, using a tungsten density of 19250 kg/m^3 we can then calculate the mass per unit area as:

$$
\frac{m}{A} = 7.459 + 4171.25d\left[\frac{kg}{m^2}\right] \qquad (1.12)
$$

This value excludes the propellant tank mass and the power conditioning system (PCS) mass. The propellant tank would be less massive in the case of electrosprays since the propellant is stored in an unpressurized vessel, as opposed to high pressure gas storage needed for xenon and argon in hall and ion thrusters. The PCS mass per unit power should be on the same order as the ion thruster due to similar voltage requirements, but could be considerably more than a hall thruster system when compared per unit power. Hall thrusters consume more power than electrospray arrays due to their lower efficiency, therefore the comparison may become closer. Using the model again, we see the specific mass ratio as a function of emitter separation and compare it to the ion and hall thruster performance in Figure 1-11.

We see that the proposed electrospray thruster array shows a significant advantage over the hall thruster and ion engine at emitter separations less than 1 mm. Electrospray technology is even more appealing if the thrust to volume ratio is studied. Using the geometry shown in the previous figure we can work out the volume per unit area as being:

$$
\frac{V}{A} = t_{base} + t_{ext} + d + h \qquad (1.13)
$$

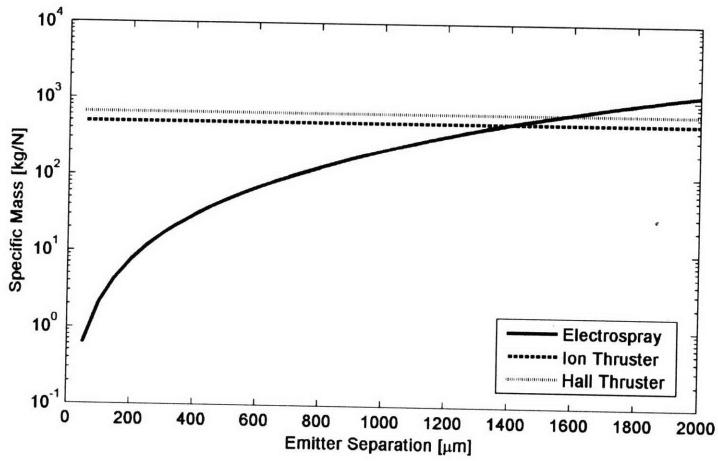

Figure 1-11: Effect of Emitter Separation on Specific Mass

$$\frac{V}{A} = 0.00055 + 1.4d \left[\frac{m^3}{m^2}\right] \tag{1.14}$$

Using the simplified model again, we show the specific volume relationship in Figure 1-12.

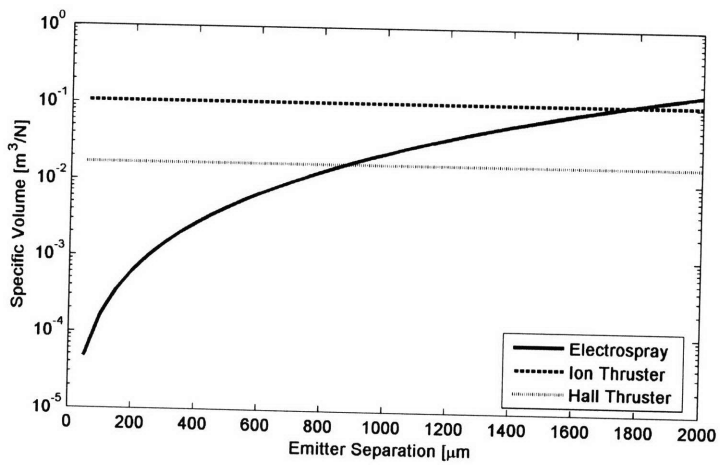

Figure 1-12: Effect of Emitter Separation on Specific Volume

It has been shown that the miniaturization and close packing of electrospray emitters significantly increases the applicability of the technology for in space propulsion. A direct comparison of an array with an emitter separation distance of 300 um is

	Specific Area $\left[\frac{m^2}{N}\right]$	Specific Mass $\left[\frac{kg}{N}\right]$	Specific Volume $\left[\frac{m^3}{N}\right]$
Electrospray	0.96	16.8	0.00146
BHT-1000 (Hall)	0.70	657.716	0.01570
NEXT (ION)	0.53	496.709	0.10605
BHT-1000/Electrospray	0.725	39.16	11.4
Nasa Next/Electrospray	0.55	29.57	72.5

Table 1.2: Clustering Performance Comparison with d = 300 μm

shown in Table 1.2.

This table illustrates some of the important advantages that clustered electrospray emitters could have over conventional electrostatic technologies. The electrospray thruster example needs slightly less frontal area per unit force as the BHT-1000 and NEXT thrusters. It is nearly 30 times less massive than the NEXT and almost 35 times less massive than the BHT-1000 for the same thrust. It also occupies slightly more than 11 times less volume as the BHT-1000 and almost up to 75 times less volume than the NEXT thruster. The advantage in the specific mass category could be even greater if less dense materials were used for the emitters and extractor. As we will see in Chapter 4, the emitter fabrication process is not limited to just tungsten, but could also be used with lighter metals such as titanium. Assuming a density of 4506 kg/m^3 and the same device dimensions used to calculate the specific mass for tungsten, we get the following relation for the mass per unit area as a function of emitter separation:

$$\frac{m}{A} = 1.7461 + 976.4d \left[\frac{kg}{m^2}\right] \tag{1.15}$$

Table 1.3 shows the specific mass comparison if titanium was used for the emitters and the extractor.

	Specific Mass $[\frac{kg}{N}]$	Increse from Titanium
Electrospray (Ti)	3.93	-
Electrospray (W)	16.8	4.27
BHT-1000 (Hall)	657.716	167.35
NEXT (ION)	496.709	126.38

Table 1.3: Clustering Performance Comparison with Titanium and d = 300 μm

1.4 Electrospray Thruster Applications

Electrospray propulsion is uniquely suited to many space missions given its specific performance described above. The following are areas in which electrospray devices are exciting:

1. Nano, Micro and Regular Satellite Main Propulsion
2. Fine Pointing for Space Telescopes
3. NSSK for GEO Satellites
4. Deep Space Missions

Nano, Micro and Regular Satellite Main Propulsion

Electrospray propulsion is an ideal solution for nano and pico satellite main propulsion given its large thrust-to-mass as well as large thrust-to-volume ratios and its inherent miniaturization potential. A typical nano satellite has a characteristic dimension of around 20 cm with a mass of 10 kg, which is smaller than most hall and ion thrusters! Furthermore, attempts at miniaturizing hall and ion thrusters has been met with severe difficulties in maintaining high overall efficiency. In addition, electrospray thrusters use propellant stored in the liquid state which saves propellant tankage mass and passively fed electrospray emitters do not require a pressurized propellant feed system.

Other small propulsion devices include: micro-scale cold gas thrusters[7], field emission electric propulsion (FEEP) and traditional colloid thrusters, suffer from other problems. Miniaturized cold gas thruster have very low performance (Isp $\approx$

30 s) and also need to store the low density propellant gas. FEEP devices require propellant heating and have higher operating voltages which complicate electronics and easily contaminate spacecraft surfaces. Colloid thrusters operate with specific impulses around 800 s, but suffer from complex propellant feed systems and also from spacecraft contamination to a lesser extent.

Fine Pointing for Space Telescopes

Due to the very small thrust of a single electrospray emitter, very precise fine pointing is possible for in space telescopes. In addition, electrospray thrusters typically need no conditioning time before operations, unlike many hall and ion devices which need conditioning time due to cathode operation procedures and FEEP devices which need to heat the liquid metal propellant. One example of a mission that needs very fine thrust control is the LISA Pathfinder mission. Two candidate technologies for the mission are a FEEP thruster and a colloid thruster. Electrospray sources would also be ideal for the mission, although voltage alternation might not be compatible with the thrust noise levels.

NSSK for GEO Satellites

With the fabrication of high density emitter arrays, electrospray technology becomes an option for GEO satellite orbit maintenance. It provides an efficient way to increase ΔV in terms of propellant mass and takes much less volume than conventional electric propulsion, or chemical propulsion since the heavy power processing system is part of the satellite payload.

Deep Space Missions

Potentially long duration missions with large ΔV requirements have historically been out of reach of electrospray propulsion given its small thrust amounts. With the miniaturization and packing of many emitters, the resulting thrust density is now on the order of what would be required on a mission.

Chapter 2

Electrospray Characteristics

2.1 Basic Physics

2.1.1 Surface Charge and Relaxation Time

The electrospray operational process is a balance between surface traction forces in the liquid caused by an external electric field and surface tension forces which are a property of the liquid itself. If we take the liquid as being a dielectric with dielectric constant (ϵ), then we can relate the electric field in the liquid (E_n^l) to the applied electric field outside (E_n^g) using Gauss' Law without free charges:

$$E_n^l = \frac{1}{\epsilon} E_n^g \tag{2.1}$$

The dielectric constant for certain liquids can be quite large, which implies that the electric field in the liquid is much less than the electric field outside. For perfect conductors we recover the zero field condition. This is because of the high mobility of free electrons that lead to very fast relaxation times. Although dielectrics with very high dielectric constants can still have non-zero electric fields in the tangential direction. Another important concept when modeling electrosprays is the concept of charge relaxation. Due to the finite mobilities of charged particles, the liquid will take some time to adjust to a change in the external electric field. The conductivity

of a material is the charge density multiplied by the lumped mobility.

$$\kappa = n\,e\left(\mu^{+} + \mu^{-}\right) \tag{2.2}$$

The rate of free surface charge density accumulation is equal to the conductivity times the liquid electric field:

$$j = \frac{d\sigma_f}{dt} = \kappa E_n^l \tag{2.3}$$

Again using Gauss' Law, we can obtain an expression for the free surface charge density:

$$\sigma_f = \epsilon_0 E_n^g - \epsilon\epsilon_0 E_n^l \tag{2.4}$$

By combining Equations 2.3 and 2.4 we obtain the following differential equation:

$$\frac{d\sigma_f}{dt} + \frac{\kappa}{\epsilon\epsilon_0}\sigma_f = \frac{\kappa}{\epsilon} E_n^g \tag{2.5}$$

The quantity $\left(\frac{\kappa}{\epsilon\epsilon_0}\right)^{-1}$ is known as the relaxation time and is a measure of how long it will take the liquid to respond to externally applied electric fields.

2.1.2 Taylor Cone Formation

When a conductive liquid is placed in an external electric field, surface traction forces will tend to pull on the liquid and deform it into a conical structure called the Taylor cone. A detailed study on the physics behind this phenomenon is explained elsewhere[46, 36]. If a balance is made between the electrical traction forces and surface tension forces shown in Figure 2-1, the normal electric field acting on the liquid surface is:

$$E_n = \sqrt{\frac{2\gamma \cot \alpha_T}{\epsilon_0 r}} \tag{2.6}$$

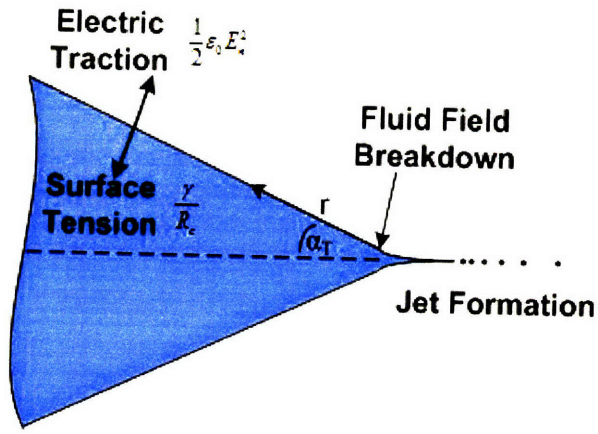

Figure 2-1: Taylor Cone Schematic

Where α_T is the Taylor angle. This angle is found analytically by solving Laplace's equation for the potential distribution using spherical coordinates. The solution includes Legendre Polynomials of the first (P) and second (Q) kind which are used to find the cone angle that gives constant potential on the liquid surface. The Taylor angle is found to be 49.29°.

Because of the liquid's finite conductivity, as the liquid flows to the tip of the cone it creates an electric field in the radial direction. When this field becomes comparable to the normal electric field, then the the cone equilibrium breaks down and a jet of charged liquid is emitted from the apex. In other words, as the liquid's local fluid residence time becomes comparable to the relaxation time, then the charges withing the liquid cannot react fast enough to counter the increasing external electric field. Because of this, the balance between surface tension and electrostatic traction is broken and the Taylor cone tip breaks down into a cone-jet.

2.1.3 Emitted Current and Starting Voltage

It has been shown experimentally[39] that in the cone-jet regime the amount of extracted current depends on the conductivity, the surface tension and the flowrate:

$$I = \frac{f(\epsilon)}{\sqrt{\epsilon}} (\gamma \kappa Q)^{1/2} \tag{2.7}$$

This relation is important in that is shows that the extracted current is independent of the fluid viscosity, the applied electric field and emitter geometry.

The starting voltage of a capillary emitter, operating in the droplet emission regime, is found by solving for the electric potential surrounding an emitter and then calculating the applied voltage needed to overcome the surface tension forces in the liquid. The potential surrounding the emitter is found by solving the Laplace equation ($\nabla^2 \phi = 0$). The problem is more easily solved if spheroidal prolate coordinates are used[36]. A potential difference is applied between an extractor plate located a distance h from the emitter tip as shown in Figure 2-2. The coordinate transform to x,y,z coordinates is shown below:

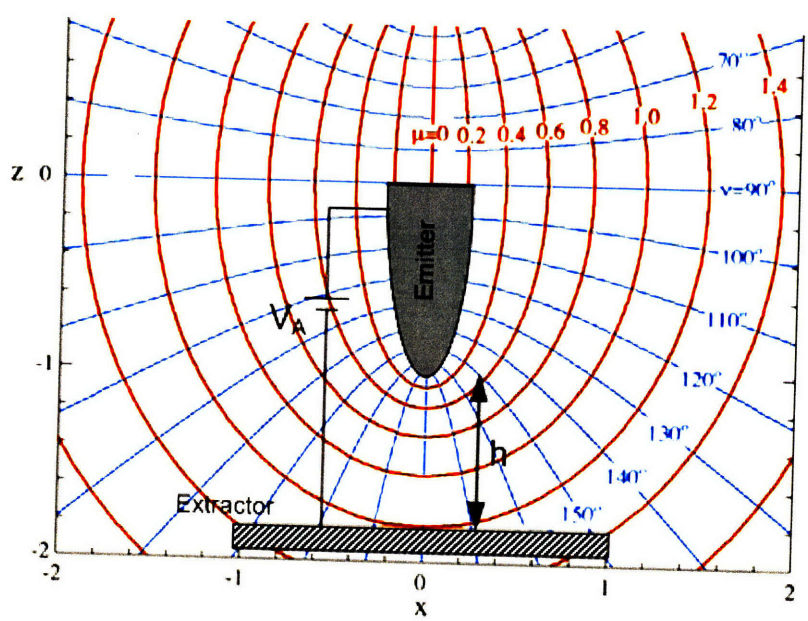

Figure 2-2: The Spheroidal Prolate Coordinate System (left) and The Emitter Geometry (right)

$$x = a \sinh \mu \sin \nu \cos \theta \tag{2.8}$$

$$y = a \sinh \mu \sin \nu \sin \theta \tag{2.9}$$

$$z = a \cosh \mu \cos \nu \tag{2.10}$$

Where μ and ν are shown in Figure 2-2 and θ is the azimuthal angle around the z-y intersection line. Laplace's equation can then be written in this coordinate system as:

$$0 = \frac{\partial}{\partial \mu}\left[\left(1-\mu^2\right)\frac{\partial \phi}{\partial \mu}\right] \tag{2.11}$$

Which can be solved using the boundary conditions of $\phi\left(\mu = \mu_0\right) = V$ and $\phi = 0$ at the extractor. The solution for the potential is then:

$$\phi = V\frac{\tanh^{-1}\mu}{\tanh^{-1}\mu_0} \tag{2.12}$$

And through some manipulations explained in detail elsewhere[36], we can then calculate the electric field at the emitter tip as being:

$$E = \frac{2V/R_c}{\ln\left(\frac{4h}{R_c}\right)} \tag{2.13}$$

The starting voltage is then found, if we assume that emission will start when the electric traction forces overcome the surface tension forces in the liquid to deform the liquid meniscus into a Taylor cone. The balance is written as:

$$\frac{1}{2}\epsilon_0 E^2 = \frac{2\gamma}{R_c} \tag{2.14}$$

Plugging in Equation 2.13, we can solve for V_s:

$$V_s = \sqrt{\frac{\gamma R_c}{\epsilon_0}}\ln\left(\frac{4h}{R_c}\right) \tag{2.15}$$

This is the same starting voltage that was used to calculate the starting voltage for the electrospray clustering model in Section 1.3.1. This solution typically overestimates the starting voltage and as a result is usually written as:

$$V_s = \sqrt{\frac{\gamma R_c}{\epsilon_0}} \ln\left(\frac{\beta d}{R_c}\right) \tag{2.16}$$

Where β is usually in the range of 2-4.

2.1.4 Field Evaporation of Ions

A second operating regime is characterized by the emission of ions from the apex of the emitter. Equation 2.6 shows that the normal electric field acting on the liquid surface increases with closer proximity to the apex of the Taylor cone. If this electric field increases sufficiently to overcome the ionic free energy before the cone breaks up to form a liquid jet, then the electrospray will operate in pure ionic mode. The extraction of ions from the surface of a liquid is an activated process, which means that at a critical value of the electric field, the rate at which ions are extracted increases significantly. The field current emitted per unit area found from statistical mechanics in equilibrium, assuming full charge relaxation, is given as[36]:

$$j = \epsilon_0 E_n \frac{kT}{h_p} e^{-\frac{\Delta G - G(E)}{kT}} \tag{2.17}$$

Where h_p is Planck's constant, ΔG is the free energy of solvation and $G(E)$ is the amount of free energy that is reduced for a given electric field. The field enhancement in the emission of ions has been theoretically determined using an image charge argument[27] which says that the ions are being pulled away from the liquid surface by the electric field while being pulled back in by their own image charge. Using a simple force balance for this model, as shown in Figure 2-3, we see that the net force is:

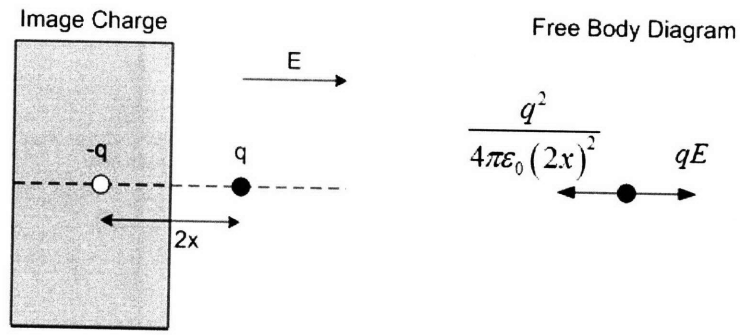

Figure 2-3: Image Charge Model to Model Ion Evaporation

$$F = -\frac{q^2}{4\pi\epsilon_0 (2x)^2} + qE \tag{2.18}$$

We can then define the work to bring the charge from a given position x to ∞ as being:

$$W = \int_x^{+\infty} F(x)dx \tag{2.19}$$

Which gives the potential energy with zero electric field at infinity:

$$W = -\frac{q^2}{16\pi\epsilon_0 x} - qE_n x \tag{2.20}$$

It is clear that this function exhibits a maximum value at some distance from the liquid surface. We can then solve for the maximum potential energy which is known as the shottky depression[27].

$$W = -\left(\frac{q^3 E_n}{4\pi\epsilon_0}\right)^{1/2} \tag{2.21}$$

And now substituting this back into the current density equation:

$$j = \epsilon_0 E_n \frac{kT}{h_p} e^{-\frac{1}{kT}\left(\Delta G - \left(\frac{q^3 E_n}{4\pi\epsilon_0}\right)^{1/2}\right)} \tag{2.22}$$

It is now easy to see that significant ion extraction from the surface occurs when $G(E)$ is roughly equal to ΔG. When this balance is made, the electric field necessary

can then be solved for and is given by:

$$E_n = \frac{4\pi\epsilon_0 \Delta G^2}{q^3} \tag{2.23}$$

It has been experimentally verified that for many common electrospray solvents, field evaporation occurs at a field strength of around $1 - 2$ V/nm[27], which corresponds to a ΔG of around $1.2 - 1.7$ eV.

2.1.5 Electrospray Efficiency

The total efficiency of an electric propulsion system can be defined as the ratio of usable jet power to input power:

$$\eta_T = \frac{\frac{1}{2}F^2/\dot{m}}{I_T V_a} \tag{2.24}$$

Where I_T is the total current going through the power supply and V_a is the accelerating potential. The individual sources of efficiency can be broken down into a few categories which contribute to the total efficiency as given by Equation 2.28[33]. The first is the efficiency of ionization (η_i), which captures the loss of neutral molecules which provide negligible thrust. Since the vapor pressure of ionic liquids is very small, and the extraction of propellant is entirely electrostatic, the loss of neutral liquid is negligible, giving $\eta_i \approx 1$. One factor that may reduce the efficiency of ionization is the fragmentation of ions in the acceleration region, although research is ongoing into characterizing this process. Another source of inefficiency has to do with the amount of beam current that is intercepted by the extractor or accelerator plates and is called the transmission efficiency (η_{tr}). This is primarily a function of emitter to extractor alignment and can be minimized with proper design and fabrication. The amount of current that is intercepted is generally less than 1%, see Section 6.4.1, which gives relatively high transmission efficiencies $\eta_{tr} \geq 0.99$.

In addition, the angular spreading of the ion beam after acceleration (η_θ) should be considered. It has been estimated that for a worst case scenario of a final beam with a

42° half angle, that $\eta_\theta \approx 0.9$, although typical beam spreading angles are on the order of 20°, giving $\eta_\theta \approx 0.975$. A fourth source of inefficiency has to do with the conversion of electrical power to the kinetic energy of the emitted species (η_E). This quantity measures the heating of the electrospray source itself as well as other inefficiencies and becomes more important as the power density of electrospray devices is increased, as with the two dimensional dense arrays introduced in Section 7.1. Unlike emitters operating in the droplet regime, ionic liquids have been shown to operate with low energy deficits, giving $\eta_E \approx 0.98$[33].

The last source of major inefficiency in the system relates to the composition of the beam and is called the polydispersive efficiency (η_p). It quantifies the wasted energy in accelerating particles with different charge to mass ratios. This efficiency can be easily quantified for the emission of two species using the following relation[28]:

$$\eta_p = \frac{\left[1 - \left(1 - \sqrt{\xi}\right) f_1\right]^2}{1 - (1 - \xi) f_1} \tag{2.25}$$

Where ξ is the ratio of the specific charges and f_1 is the fraction of one of the species:

$$\xi = \frac{\left(\frac{q}{m}\right)_2}{\left(\frac{q}{m}\right)_1} \tag{2.26}$$

$$f_1 = \frac{I_1}{I_1 + I_2} \tag{2.27}$$

The efficiency has a strong dependence on the specific charge ratio and will therefore be more of a factor for the ion-droplet mixed regime than for the ion regime containing two ionic species. Figure 2-4 shows the polydispersive efficiency plotted as a function of the monomer ion fraction for an emitter operating in the pure ion emission regime, producing the monomer and dimer for EMI-BF_4 and for EMI-IM in both polarities. The monomers and dimers corresponding to the two ionic liquids are shown in Table 2.1. Table 2.2 shows the input parameters to compute the polydispersive

Liquid	Mode	Monomer	Dimer
EMI-BF_4	(+)	$[EMI]^+$	$[EMI\text{-}BF_4][EMI]^+$
EMI-BF_4	(-)	$[BF]^-$	$[EMI\text{-}BF_4][BF]^-$
EMI-IM	(+)	$[EMI]^+$	$[EMI\text{-}IM][EMI]^+$
EMI-IM	(-)	$[IM]^-$	$[EMI\text{-}IM][IM]^-$

Table 2.1: Beam Ions for EMI-BF_4 and EMI-IM

Liquid (Mode)	Monomer q/m $[C/g]$	Dimer q/m $[C/g]$	ξ	f_m (Exp)	η_p
EMI-BF_4 (+)	869.2	312.2	0.359	0.4258	0.93
EMI-BF_4 (-)	1111.6	338.8	0.305	0.4913	0.94
EMI-IM (+)	867.7	192.0	0.221	-	-
EMI-IM (-)	344.3	143.7	0.417	0.524	0.955

Table 2.2: Polydispersive Calculation Input Parameters

efficiencies using Equation 2.25, which have been measured using time-of-flight mass spectrometry (Section 6.2.2). The values for η_p have also been tabulated according the the monomer ion current fraction experimentally found. Time of flight experiments for EMI-IM were not performed in the positive polarity so the polydispersive efficiency could not be estimated.

Combining the effects of all the efficiencies, as described by Lozano et. al.[33], we obtain the following relation for the total efficiency. The total efficiency for an electrospray source using EMI-BF_4 in the ion regime is generally above 86%, although this could be lower for EMI-IM in the positive mode due to the low polydispersive efficiency.

$$\eta_T = \eta_i \eta_{tr}^2 \eta_\theta \eta_E \eta_p \geq 0.86 \tag{2.28}$$

2.1.6 Droplet vs. Ion Emission

The operation of electrospray sources largely depends on a few parameters including liquid transport, the liquid conductivity and the magnitude of the electric field at the emission region. The emission of ions in some organic solutions is controlled

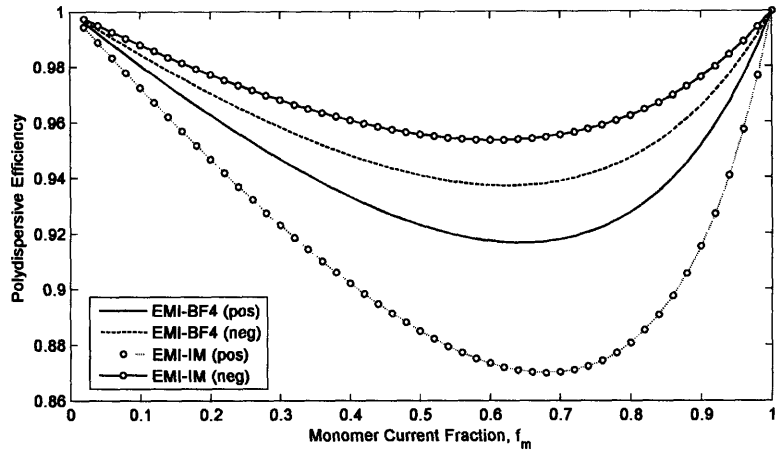

Figure 2-4: Polydispersive Efficiency of EMI-BF_4 and EMI-IM as a function of monomer current fraction

by the ratio of the conductivity to flowrate ratio (K/Q). For large values of K/Q, corresponding to either low flowrates and high liquid conductivities, ions will be produced. For small values of K/Q, corresponding to either low conductivities or large flowrates, droplets are emitted.

Since we have control over these parameters that set whether of not the device operates in ion or droplet regime, then the question is what regime is best suited for the mission requirements. Furthermore, electrospray sources have also been shown to work in the mixed ion-droplet regime which adds an additional element of control for the device's specific impulse and thrust, although there are severe efficiency reductions when operating in the mixed regime as was seen in Section 2.1.5. Electrospray sources operating in droplet regime produce more thrust but at a lower specific impulse, while sources operating in the ion regime produce less thrust with a higher specific impulse. Figure 2-5 shows the ion mass fraction, the polydispersive efficiency (η_p) and the specific impulse as a function of the ion current fraction (f_i), assuming that the specific mass ratio (ξ) = 0.02. This mass ratio corresponds to ions with a charge to mass ratio of 440 C/g (EMI-BF_4 emitting negative ions) and droplets with a charge to mass ratio of 10 C/g, which is commonly seen in capillary emitters. It is clear that η_p is unity when the beam composition is either all droplets or all ions. It reaches

a minimum of around 0.5 at $f_i = 0.85$, signifying a severe reduction in efficiency. In addition, the specific impulse reduction is even greater, reaching 50% of the pure ionic value for $f_i \approx 0.95$. This is significant in that the addition of a small fraction of droplets has large effects on both efficiency and specific impulse.

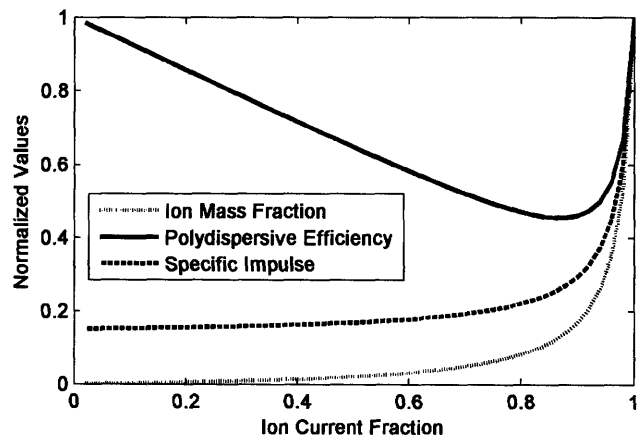

Figure 2-5: Operational Performance in the Mixed Ion-Droplet Regime

2.2 Types of Electrospray Emitters

The requirements of electrospray emitters are twofold: they must terminate in a region (typically a sharpened tip) that locally enhances the electric field, and they must provide some way to transport liquid to the tip. Today there are many different types of electrospray emitters including traditional capillaries, externally wetted emitters and internally wetted emitters as shown in Figure 2-6.

Capillary emitters provide liquid to the tip either by pressure or just using capillarity alone. Performance is characterized by relatively large flowrates which tend to make the device operate in the higher thrust but lower efficiency droplet mode. Miniaturization and array creation is made difficult by the need to create precise and repeatable high aspect ratio holes at the miniature level. Despite this difficulty, research is ongoing in the fabrication of dense capillary emitter arrays. Alexander et. al. at the University of London[5] has reported success in creating dense arrays

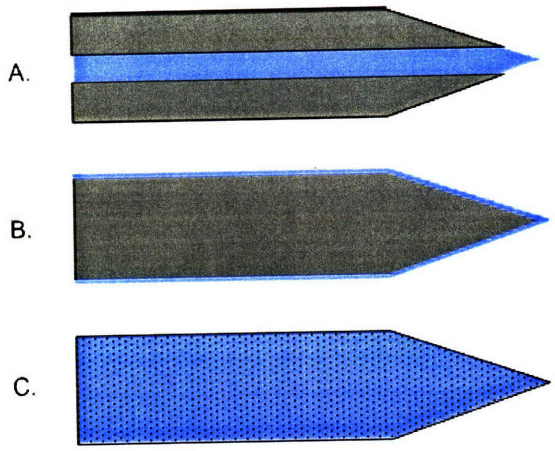

Figure 2-6: Electrospray emitter types: A. traditional capillary emitter, B. externally wetted emitter, C. internally wetted porous emitter

using a DRIE process in silicon. They have created miniaturized capillary emitters with an emitter separation of 250 μm, with a 19 emitter array shown in Figure 2-7. Single microfabricated capillaries were shown to operate in the droplet mode with Tri-Ethylene Glycol Solutions (TEG) Doped with NaI. Typical emitted currents ranged from 270 μm to 300 μm for applied extractor voltages of 8.02 kV to 9.5 kV. They report charge to mass ratios of 14 C/kg and an estimated thrust of 29.5 μN for an additional acceleration voltage of 2 kV provided by an accelerator electrode, and an array of 7 emitters. This would give a specific impulse of roughly 31 s, assuming a total emitted current of 1200 nA for 7 emitters, and an accelerating voltage of 2 kV. They estimate that with an ionic liquid, such as EMI-BF_4, specific impulses would be around 500 to 700 seconds, but with a reduction of thrust to 0.5 μN per emitter with a very high acceleration voltage of 20 kV. These results are derived from a paper in which limited data was made availible and should be used for insight only.

Another type of electrospray emitter relies on surface wetting alone to transport liquid to the emission region. These emitters allow electrospray devices to be miniaturized without the need to fabricate large aspect ratio holes, and do not suffer from numerous other problems including: gas blockages in the microfluidic network, difficulties in the Taylor cone formation that may lead to electrical shorting, and trouble regulating the flowrate to ensure ion emission. In externally wetted configurations

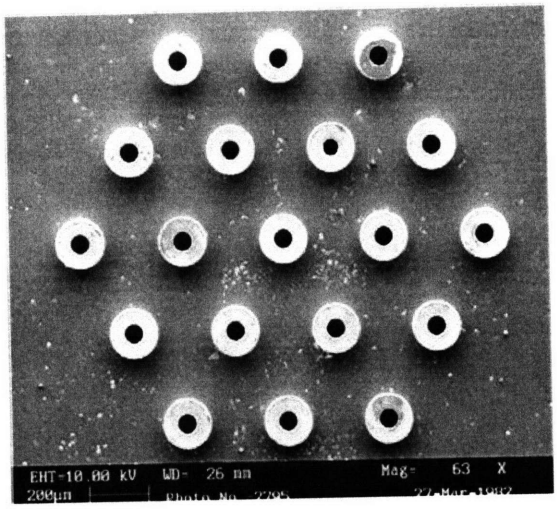

Figure 2-7: Micro Capillary Electrospray Device[5]

there is no risk of clogging as there is with capillaries and flowrates are low enough to allow the device to operate in the purely ionic regime.

Initial research was conducted in characterizing the performance of needle emitters fabricated out of tungsten, similar to those used in liquid metal ion sources. Initial results proved that pure ion emission was attainable, with current levels on the order of 200 - 300 nA[34]. Since the emitted current was quite low, it was then desirable to cluster many emitters together. In addition, it was experimentally found that flat ribbon emitters would support more flow to the emission site and therefore emitted more current. A device with many of these emitters was constructed to demonstrate emitter clustering[30], however, the fabrication method was not designed for miniaturization.

Research was also conducted into preparing very dense emitter arrays out of silicon since well established microfabrication techniques could be used. This work produced very repeatable emitter arrays, but had significant problems with liquid wetting, which led to unreliable performance[14]. In order to increase the amount of current that could be transported to the emission region, while allowing for the use of microfabrication techniques, research started on using porous tungsten as the emitter material. The use of a porous substrate, it was hypothesized, would allow for more

flow to the emitter tip, and therefore more emitted current and thrust. This is the research that is presented in this thesis.

2.3 Fluid Transport in Porous Emitters

A finite difference numerical scheme will model fluid flow through a porous emitter using the two-dimensional flow equation (Equation 2.29) combined with Darcy's Law. The simulation will be solved in two dimensions and will assume axial symmetry for the emitter, giving the emitter geometry as a cone with the end chopped off. The computational domain is shown in Figure 2-8 Inputs for the model will be a pressure head dirichlet boundary condition on the emitter tip to model the hydraulic pressure difference driving emission as well as various geometrical constants which detail the emitter porosity as well as fluid properties. The two dimensional steady state flow equation, found through mass conservation relations is:

$$\frac{\partial}{\partial x}\left(K_x(x)\frac{\partial}{\partial x}(H)\right)+\frac{\partial}{\partial y}\left(K_y(x)\frac{\partial}{\partial y}(H)\right)=0 \tag{2.29}$$

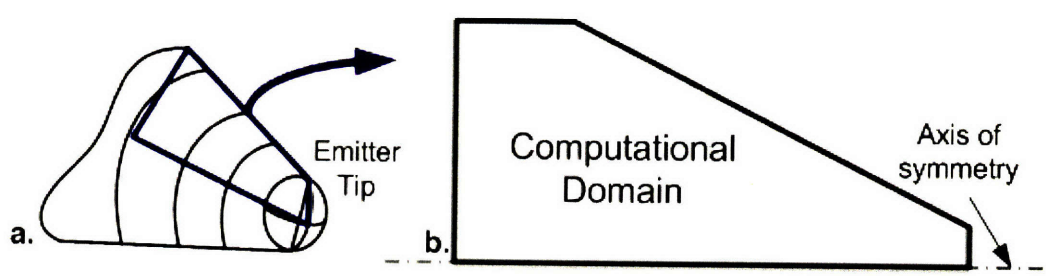

Figure 2-8: Finite Difference Computational Domain showing a. the whole conical emitter and b. the axis-symmetric numerical domain

Where K_x and K_y are the effective hydraulic conductivity of the liquid in the porous media. For this application, K will only vary in the x-direction so that in the second term, K_y can be considered a constant and taken out of the expression. If the hydraulic conductivities were constant throughout the emitter, the equation would simplify to the laplace equation for pressure head $\nabla^2 H = 0$.

2.3.1 Darcy's Law and Fluid Conductivity

The hydraulic conductivity for the system is dependent on both the pore diameter δ and on the viscosity of the fluid μ. K is considered a conductivity because it relates the gradient of the pressure head to the amount of fluid flow as seen in Equation 2.30. The larger K is, the higher the flowrate for a given pressure head gradient.

$$\hat{q} = -K\nabla H \tag{2.30}$$

Where $\hat{q}$ is the flux of volume of the liquid. The hydraulic conductivity is expressed as:

$$K = \frac{\kappa \rho g_0}{\mu} \tag{2.31}$$

Where κ $[m^2]$ is the intrinsic permeability of the porous substrate, μ $[Pa : s]$ is the dynamic viscosity of the fluid, ρ $[kg/m^3]$ is the density of the fluid and g_0 is the gravitational constant at sea level.

The intrinsic permeability of the porous media depends on many factors including the average pore diameter, the complexity of flow channels, the relative Reynolds number of the flow, etc... It is a quantity that is best found experimentally, although some analytical solutions exist for the case where the average pore diameter is known. For this analysis, data provided by Mott Corporation, a porous metal supplier, was used to estimate the intrinsic permeability as a function of average pore size. Figure 2-9 shows the experimentally found intrinsic permeability as a function of average pore diameter.

2.3.2 The Discretization of Darcy's Law

The discretization scheme used is a standard central difference scheme in the non varying porosity direction and a central difference scheme using a staggered grid to

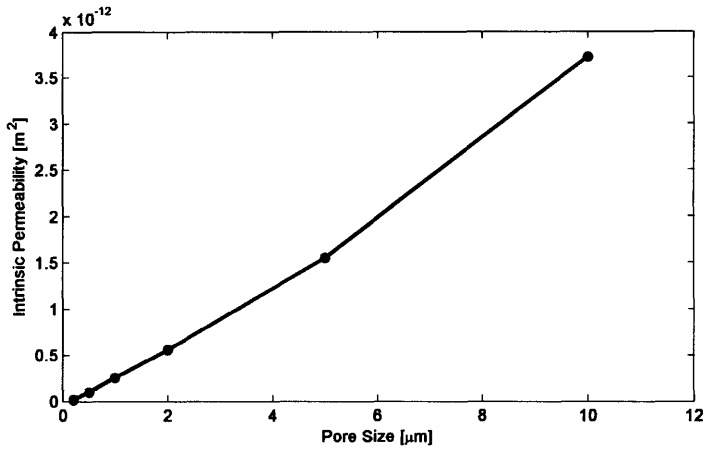

Figure 2-9: Intrinsic Permeability as a Function of Average Pore Diameter

approximate the porosity gradient in the directions of varying porosity. The flow equation can be re-written as:

$$0 = \frac{\partial}{\partial x}\left(K\left(x\right)H_x\right) + K\left(x\right)H_{yy} \tag{2.32}$$

The term in the y direction is trivial, since the hydraulic conductivity does not vary in this direction, and will be approximated using the following central difference scheme:

$$H_{yy} = \frac{H_{i,j+1} + 2H_{i,j} + H_{i,j-1}}{\left(\Delta y\right)^2} \tag{2.33}$$

The term in the x direction is a little more complicated. We start off by defining the quantity V as the hydraulic conductivity times the forward finite difference approximation for the derivative of H:

$$V = K\left(x\right)H_x = K_{i+\frac{1}{2},j}\left(\frac{H_{i+1,j} - H_{i,j}}{\Delta x}\right) \tag{2.34}$$

And then the derivative of this expression in the x direction is approximated by a backward step approximation:

$$V' = \frac{V_{i,j} - V_{i-1,j}}{\Delta x} \tag{2.35}$$

$$V' = \frac{K^+ H_{i+1,j} - (K^+ - K^-) H_{i,j} + K^- H_{i-1,j}}{(\Delta x)^2} \tag{2.36}$$

Where $K^+ = K_{i+\frac{1}{2}}$ and $K^- = K_{i-\frac{1}{2}}$. Figure 2-10 shows a graphical description of the modified 5 point stencil used in the above numerical approximation.

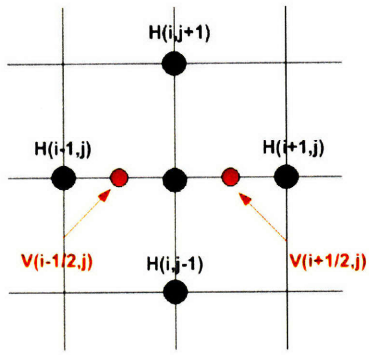

Figure 2-10: Numerical Stencil Used to Model Flow

2.3.3 Model Geometry and Boundary Conditions

The computational domain is shown in Figure 2-11 where the fluid enters the base of the emitter from a reservoir at zero pressure and exits from the base of the emitter, driven by an overall difference in pressure head $-\Delta H$. The right side, as well as the flat top piece, are modeled with homogeneous dirichlet boundary conditions to model the constant head of the fluid reservoir. The left side is modeled with a uniform dirichlet boundary corresponding to $-\Delta H$. The diagonal side of the emitter as well as the bottom are modeled as neumann conditions with zero-flow, since no fluid will exit the porous emitter except at the tip. The bottom is an axis-symmetric line and is also modeled as a neumann no flow boundary due to symmetry.

The fluid flow through the porous electrospray emitter is driven by a net pressure drop caused by capillary forces and dynamic pressure from the flow at the tip of the Taylor Cone as well as the excess of electric pressure over the surface tension at the meniscus. The boundary condition of the right hand side depends on two distinctly different operational regimes. The first regime occurs when the porous material is

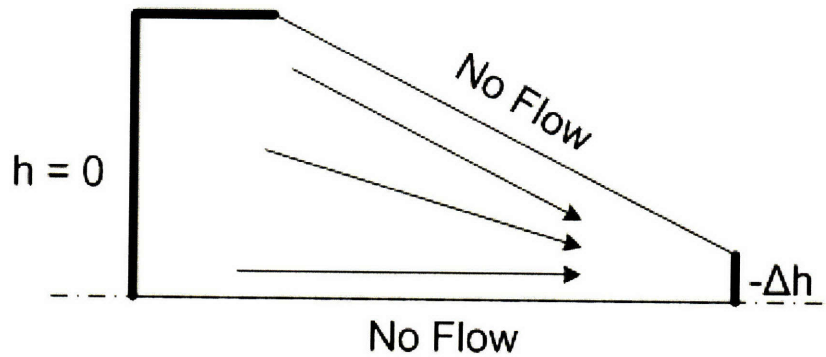

Figure 2-11: Numerical Domain and Boundary Conditions

only partially filled with liquid and the second regime occurs when the emitter array is attached to an external reservoir of liquid, and therefore, the porous emitters are always full of liquid.

In the first regime, the driving pressure for fluid flow is generated only by the dynamic pressure difference located at the tip of the Taylor cone and the excess electrical pressure, because capillary forces are balanced everywhere as shown in Figure 2-12. If we assume that the Taylor cone terminates in a region with area A, and this is where the mass flux occurs, then we can write the total flowrate of fluid (Q) passing through the cone as a function of the emitted current (I) and the characteristic area (A) and the charge to mass ratio of the emitted ions $\left(\frac{\bar{q}}{m}\right)$:

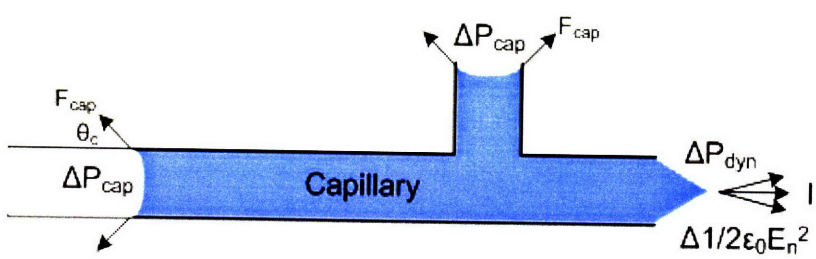

Figure 2-12: Schematic of Fluid Flow Driven by Capillary Forces

$$Q = \frac{I}{\left(\frac{\bar{q}}{m}\right)\rho} A_{ch} \tag{2.37}$$

Where A_{ch} is the area of a circular region with radius r_t. This radius can be estimated using a balance between the current density given by Equation 2.17 for the field evaporation, and the amount of current that is measured experimentally I:

$$\frac{I}{\pi r_t^2} = \epsilon_0 E \frac{kT}{h_p} e^{-\frac{\Delta G - \sqrt{\frac{e^3 E}{4\pi\epsilon_0}}}{kT}} \tag{2.38}$$

If we then use the critical Taylor electric field introduced in Section 2.6 as E:

$$E = \sqrt{\frac{2\gamma \cot\theta_T}{\epsilon_0 r_1}} \tag{2.39}$$

Where r_1 is measured from the tip of the Taylor cone along the surface of the liquid and is related to r_t by the following relation:

$$r_1 = \frac{r_t}{\sin\theta_T} \tag{2.40}$$

We can then create a function of known parameters that can be solved for the radius r_t for different emitted current values:

$$\frac{I}{\pi r_t^2} = \epsilon_0 \sqrt{\frac{2\cot\theta_T \gamma}{\epsilon_0 r_t}} \frac{kT}{h_p} e^{-\frac{\Psi}{kT}} \tag{2.41}$$

Where Ψ is:

$$\Psi = \Delta G - \frac{e^{\frac{3}{2}\left(\frac{2\cot\theta_T}{\epsilon_0 r_t}\right)^{\frac{1}{4}}}}{\sqrt{4\pi\epsilon_0}} \tag{2.42}$$

Figure 2-13 shows the dependence of r_t on the amount of emitted current given $\Delta G = 1.2$ eV. Using this calculated radius and the known emitted current, we can solve for the pressure difference caused by the dynamic pressure as:

$$\Delta P_{dyn} = \frac{1}{2}\rho \left(\frac{I}{(\bar{q}/m)\,\pi r_t^2}\right)^2 \tag{2.43}$$

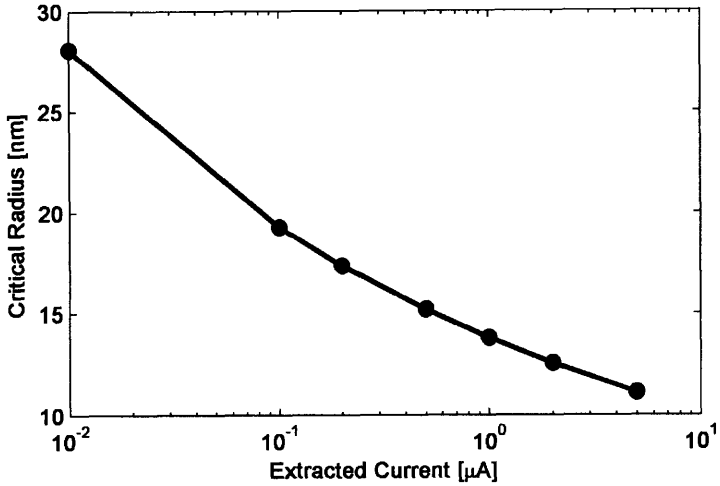

Figure 2-13: Critical Radius as a Function of Emitted Current

And the pressure head is then computed by:

$$\Delta H = \frac{\Delta P_{dyn}}{\rho g_0} + \Delta \frac{1}{2} \epsilon_0 E_n^2 \tag{2.44}$$

In the second regime where the liquid fills the entire porous sample, the capillary pressure, the dynamic pressure and the excess electrical pressure drive the flow within the fluidic network. Consider the simplified diagram of an emitter idealized as a capillary connected to a fluid reservoir is shown in Figure 2-14. The capillary forces, and hence pressure drop, is not balanced by another pressure drop upstream of the emission region in this example. This causes an increase in the pressure difference that is driving the flow. This capillary force will result in a restoring capillary pressure differential in addition to that of the dynamic pressure and excess electrical traction pressure contributions, giving the total pressure drop ΔP equal to:

$$\Delta P = \frac{F_{cap}}{A_{cap}} + \Delta P dyn + \Delta \frac{1}{2} \epsilon_0 E_n^2 \tag{2.45}$$

Where F_{cap} is the capillary force and $Acap$ is the area of the liquid meniscus. If we take the area as just the cross sectional area of the capillary:

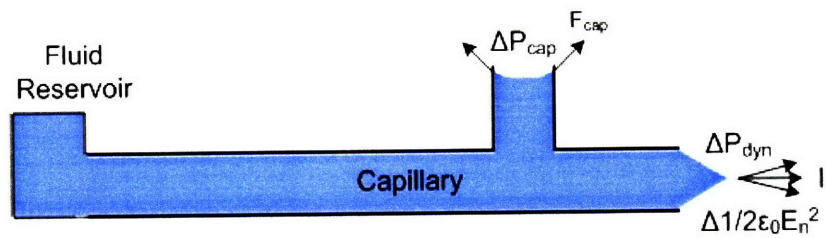

Figure 2-14: Schematic of Fluid Flow Driven by Capillary Forces and Dynamic Pressure

$$A_{cap} \approx \pi r_{cap}^2 \tag{2.46}$$

And the force is:

$$F_{cap} = 2\pi r_{cap} \cos\theta_c \tag{2.47}$$

Then the pressure difference caused by the capillary forces alone is:

$$\Delta P_{cap} = \frac{2\gamma \cos\theta_c}{R_c} \tag{2.48}$$

And the total pressure drop is:

$$\Delta P = \frac{2\gamma \cos\theta_c}{R_c} + \Delta P_{dyn} \tag{2.49}$$

The pressure head is then then computed by Equation 2.44.

2.3.4 Initial Model Results

A simple calculation shows that the pressure difference caused by the capillary forces are orders of magnitude greater than the forces created by the dynamic pressure and excess electrical pressure (both of which are of similar magnitude). If we assume that r_t is on the order of 10 nm and the amount of current emitted is 1μA, then

the corresponding pressure differential due to dynamic pressure calculated by Equation 2.43 using EMI-BF_4 is roughly 36 kPa. The magnitude of the capillary pressure using EMI-BF_4 and a contact angle of 25°, and a pore diameter of 0.5μm is given by Equation 2.48 as 380 kPa, which is roughly an order of magnitude greater than the dynamic pressure and excess electrical pressure.

For the case in which the porosity is partially filled we calculate where the pressure drop across the porous emitter becomes equal to the dynamic pressure and the excess electrostatic pressure for a given current. Figure 2-15 shows the pressure drop across the emitter for two different average pore diameters and the driving pressure plotted for different currents. We see that the pressure drop curve crosses the driving pressure curve at a single current value. This plot is significant in that at low flowrates where the driving pressure and the pressure drop across the emitter are of the same order, then we can expect that liquid will have a hard time overcoming the capillary forces to reach the emission site. In practice, we normally operate at much higher current levels, so we don't see this effect. Additionally, we usually operate with the porosity filled, which will be discussed in the next section.

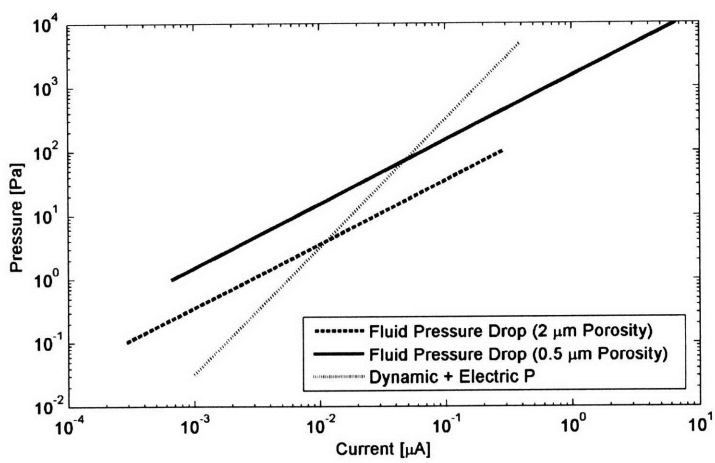

Figure 2-15: Pressure Drop Across Porous Emitter and Driving Pressure vs. Emitted Current

For the second case, it is interesting to calculate what the maximum current levels that can be supported with the capillary pressure driven flow only. Figure 2-16 shows

the maximum current level as a function of pore diameter. We see that the current levels are roughly two orders of magnitude over the emitted current experimentally seen, which indicates that we are not limited by fluid flow in this case. In addition, we see that the maximum current increases with increasing average pore size. This is counterintuitive because as the pore size increases, the capillary pressure difference decreases, however, the fluid conductivity does increase significantly which accounts for the increase in current.

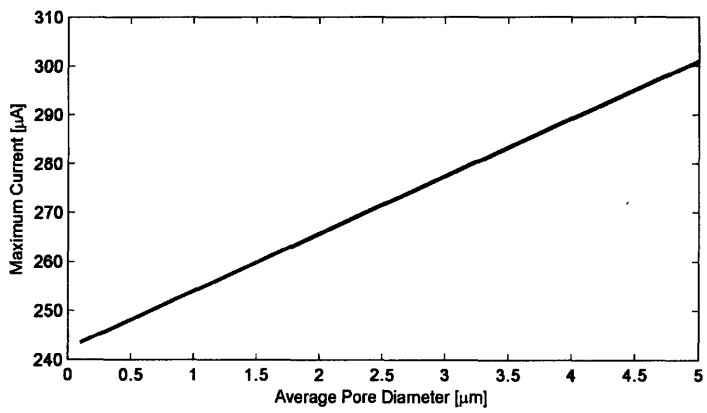

Figure 2-16: Maximum Supported Current as a Function of Average Pore Diameter

2.4 Ionic Liquid Properties

Ionic liquids are molten salts at room temperature and are comprised of only ions, much like a pure sodium chloride melt. They display many desirable properties, which make them excellent candidates for use with externally wetted electrospray devices. They posses relatively high conductivities, negligible vapor pressures (even at high temperatures), as well as non-reactive with common materials. They are stored in liquid form with no pressurization systems, they are not flammable and do not pose a significant risk of causing problems with other spacecraft systems, although care must be used when handling some ionic liquids due to toxicity. Some ionic liquids are, however, sensitive to moisture and can therefore be contaminated when exposed to atmosphere.

This section provides physical data for the common ionic liquids used in electrospray devices, including: 1-ethyl-3-methylimidazolium tetrafluoroborate (EMI-BF_4), 1-ethyl-3-methylimidazolium bis(trifluoromethylsulfonyl)imide (EMI-IM), and 1-ethyl-3-methylimidazolium bis(pentafluoroethyl) sulfonylimide (EMI-Beti).

EMI-BF_4

The freezing point of EMI-BF_4 is approximately 12.0 - 12.5deg C, although it has a strong tendency to supercool[17]. The conductivity, like most liquids, rises with temperature as shown in Figure 2-17, while the kinematic viscosity is reduced with an increase in temperature as shown in Figure 2-18. The specific conductivity at room temperature is 1.3 Si/m and the dynamic viscosity is 0.043 Pa s. EMI-BF_4 has a density 1271 kg/m^3 and a surface tension of 52 dyn/cm at room temperature.

EMI-IM

The melting point of EMI-IM is -15 deg C although it also displays a supercooling tendency, with measurable ionic conductivity well below this temperature[4]. The specific conductivity at room temperature is 0.84 Si/m and the dynamic viscosity is 0.028 Pa s. EMI-IM has a density 1517 kg/m^3 and a surface tension of 41 dyn/cm at 20°C.

EMI-Beti

EMI-Beti is an ionic liquid that has a much higher viscosity and a much lower conductivity than EMI-BF_4 or EMI-Im. The specific conductivity at room temperature is 0.34 Si/m and the dynamic viscosity is 0.061 Pa s. The melting point of EMI-Beti is -1 deg C. EMI-Beti has a density 1600 kg/m^3 and a surface tension of 28.75 dyn/cm at 21°C[8].

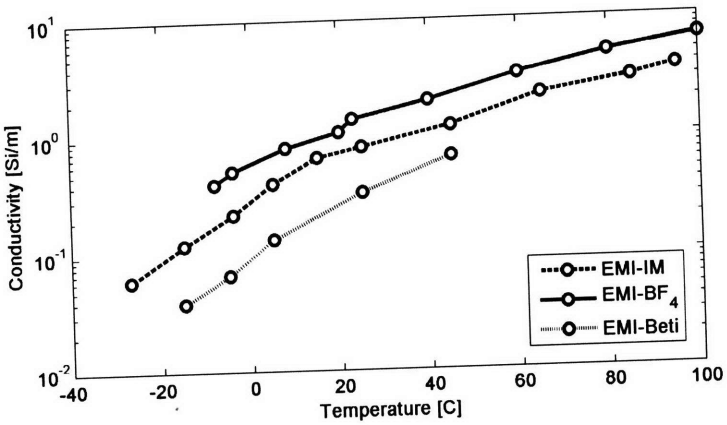

Figure 2-17: Conductivity of Various Ionic Liquids as a Function of Temperature[4]

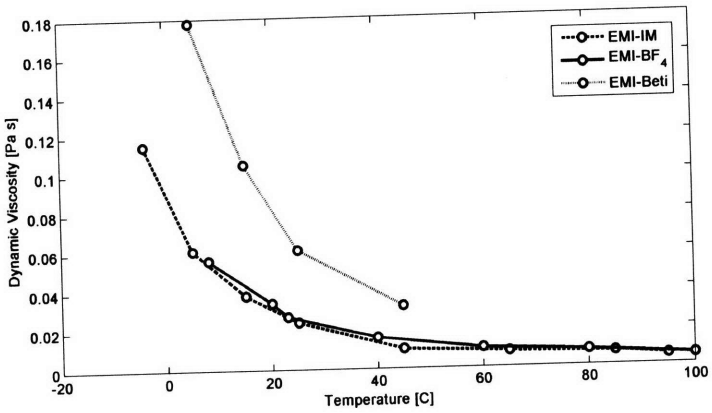

Figure 2-18: Dynamic Viscosity of Various Ionic Liquids as a Function of Temperature[4]

Chapter 3

Fabrication Technology

3.1 Basic Micromachining

The term microfabrication refers to the collection of materials, procedures and tools utilized to create micro and nano scale structures. Progress in this field was first initiated by the need to miniaturize components in the semiconductor industry, and it has now expanded into many other disciplines. Micro electro-mechanical systems (MEMS) research increased the fabrication toolset to include ways to create small devices capable of many things including: causing movement (micro actuators), sensing movement and pressure (accelerometers, pressure sensors), separating biomolecules (microfluidic bioseparation), etc... This section will give a quick overview of some of the most common microfabrication techniques in use today as preparation for the sections to come. Since the development of MEMS technology in the early 1960's many important devices have made use of the technology (Table 3.1)[43].

While some techniques in microfabrication are essentially modified conventional macro-fabrication processes, others are distinctly unique to MEMS. The two major categories of MEMS techniques are: bulk micromachining and surface micromachining. In bulk micromachining, material is selectively removed to create structures where the remaining material constitutes the structural material. In surface micromachining, material is deposited on a working substrate in either structural or sacrificial layers. The final structure is composed of the structural layers, while the

1960's	- First Silicon Pressure Sensor
	- Westinghouse Resonant Gate Transistor
1970's	- Stanford Gas Chromatograph
	- Inkjet Printheads
1980's	- Polysilicon Surface Micromachining
	- Electrostatic Micromotors
	- Capillary Electrophoresis, Lab-on-a-chip
1990's	- Stanford Gas Chromatograph
	- Optical MEMS, Computer Projectors

Table 3.1: Microfabrication Milestones

sacrificial layers serve as a support during intermediate steps in the process and are etched away when they are no longer needed. Some examples of bulk and surface micromachined devices are shown in Figure 3-1.

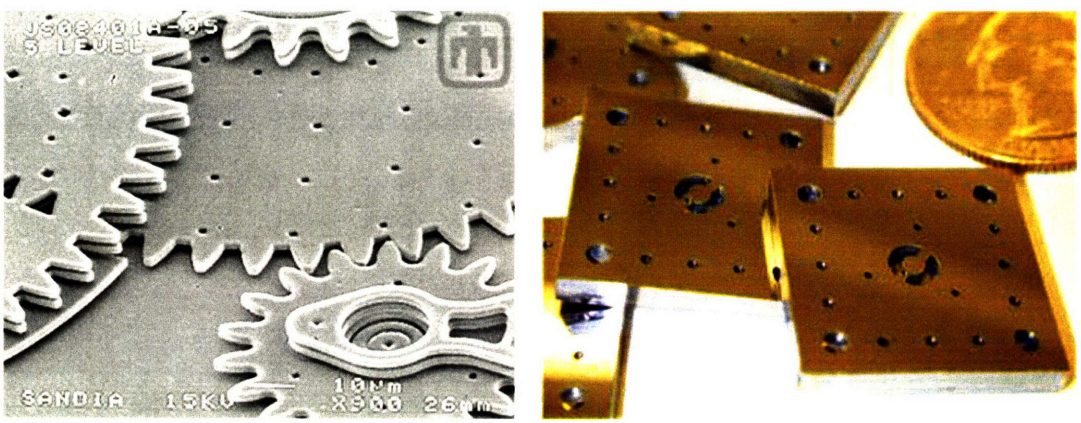

Figure 3-1: Sample MEMS Devices Including a Surface Micromachined Device (left) and a Bulk Micromachined Device (right)

The major processes in the MEMS toolbox can be divided into roughly four categories:

1. Adding Material
2. Removing Material
3. Transferring Geometry
4. Bonding Components

3.1.1 Adding Material

The process of adding material to a substrate, deposition, is an integral part of both surface micromachining and bulk micromachining. The four types of deposition commonly used are: physical vapor deposition, chemical vapor deposition, electro-deposition and spin casting.

Physical Vapor Deposition

Physical vapor deposition is the term used for both sputtering and evaporation. Sputtering is the process by which plasma is used to strip atoms of the deposition material from a source surface and deposit them evenly on the working surface. It is commonly used with both metal and non-metal materials. Evaporation is the process where a metal is heated by an incident electron beam causing a metallic vapor which is then allowed to come into contact with the working piece. The nature of the directional electron beam allows for the deposition to be directional so that certain faces can be preferentially covered.

Chemical Vapor Deposition

Chemical vapor deposition is a process by which a working piece is chemically acted on in a heated furnace at low temperatures. For example, when silicon is placed in the presence of high temperature silane (SiH_4), a reaction occurs that creates silicon directly on the surface of the working piece with hydrogen gas as the byproduct.

Electro Deposition

Electro-deposition (also known as electroplating) is the process where metallic ions dissolved in solution are deposited on a substrate through an applied voltage. This technique is primarily used for the deposition of very thin layers of metal.

Spin Casting

Spin casting involves placing a small amount of liquid material on the surface to be coated. The sample is then spun to use centrifugal forces to spread an even layer. Layer depth can be controlled by the spin rate and duration. This method is primarily used for the deposition of thin photoresist layers.

3.1.2 Removing Material

The process of selectively and precisely removing (called etching) material is a fundamental aspect of microfabrication. The four most common methods are wet etching, electrochemical etching, plasma etching, and reactive ion etching.

Wet Etching

This process involves the selective chemical removal of material from exposed areas of the working piece, while protected areas are preserved. Most wet etches are ideally isotropic, which means that the removal rate is the same in all directions normal to the exposed surface. Some etch chemistries are non-isotropic and preferentially etch some crystallographic directions faster than others as shown in Figure 3-2. Wet etching is used to remove large quantities of material in most bulk micromachining processes and is largely used to remove sacrificial layers in surface micromachining.

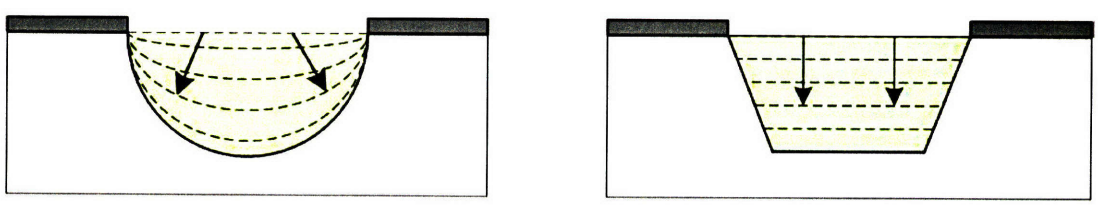

Figure 3-2: Isotropic etch (left) and anisotropic etch (right) shape evolution

Electrochemical Etching

Electrochemical etching involves the removal of material through the use of electrochemistry and is essentially the reverse process of electro-deposition. The working piece is biased to a positive voltage and in the presence of a salt solution controlled metal removal is initiated. Electrochemical etch chemistries exist for most metals and the process can be controlled by the applied voltage and distance from the cathode. The process is ideally isotropic for a smooth geometry, but localized etching rates are

significantly higher at sharper features due to the geometry enhanced electric fields. More detail will be given to the subject of electrochemical etching in a later section.

Plasma Etching

Plasma etching is a process in which the material to be etched is placed in a low pressure plasma. In some forms of plasma etching, the plasma comes into direct contact with the substrate and ions in the plasma directly impact the substrate and cause material removal through sputtering. A second form of plasma etching relies on the chemical reactivity of ions that react with the ionic species of the exposed surface causing material removal. One special form of this technique is called Deep Reactive Ion Etching (DRIE) and consists of a series of chemical plasma etching combined with polymer deposition to create structures with high aspect ratios.

3.1.3 Transferring Geometry

Two methods of transferring geometry are typically used in microfabrication including photolithography and soft contact lithography. The photolithography process is shown in Figure 3-3. In photolithography, a photo sensitive substance called photoresist is spin casted to an even coat on the material that is to be etched. The photoresist is covered by a printed mask which allows only certain areas to be exposed to ultraviolet light. When exposed, the photoresist either breaks down and is susceptible to the developer (positive photoresist) or hardens to be resistant to the developer (negative photoresist). The sample is then immersed in the developer solution to dissolve away the weakened photoresist, leaving the intended pattern. In the soft contact lithography process, a soft material (usually Polydimethylsiloxane [PDMS]) is poured into a pre-formed mold and, when allowed to cool, the geometry is made permanent.

3.1.4 Bonding Components

The most common way to bond components in MEMS application is through the use of wafer bonding. First the wafers are aligner in a bond aligner and then the

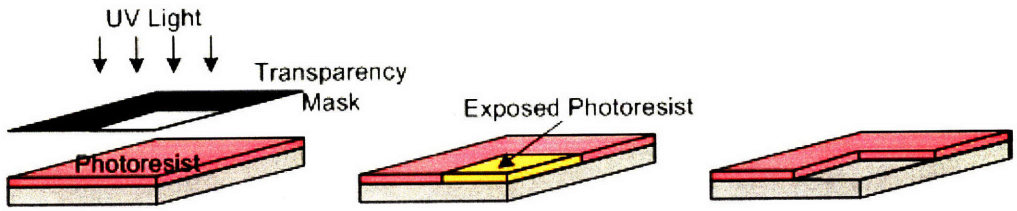

Figure 3-3: Photolithography Process

wafers are brought together under vacuum. The alignment is usually on the order of 1 μm or less[26]. There are three main bonding techniques including: direct or fusion bonding, anodic bonding and glue bonding. In direct bonding, the samples are fused together using very high heat (1000° C) which reduces the surface energy of the material, and can produce bond strengths on the order of the bulk silicon strength. Anodic bonding can be accomplished at much lower temperatures (500° C) and uses voltages from 300 to 700 volts to repel sodium ions from the surfaces to be bonded to create a strong silicon to silicon bond. The third type of bond uses either soft materials for thermocompression, or epoxy layers to create adhesion. This process is not limited to use with silicon.

3.2 Electrochemical Etching Theory

In the process of electrochemical etching or electropolishing, material is removed from the anode and added to the cathode through oxidation and reduction reactions respectively. The general process takes place in an electrochemical cell, like that shown in Figure 3-4, with two electrodes immersed in an electrolyte solution. Metals in the presence of an electrolytic solution have an affinity to give up their electrons and become ions and the measure of this tendency is called the electrochemical potential. The standard electrochemical potential is given relative to a sample hydrogen electrode and is sometimes referred to as the normal hydrogen electrode (NHE). If the electrochemical potential of the sample is positive (greater than hydrogen) then the reaction will take place in an acid, otherwise an oxidizing agent will be necessary.

Anodic Half-Reaction	Standard Potential (V)
$Au \rightarrow Au^{3+} + 3e^-$	-1.520
$Pt \rightarrow Pt^{2+} + 2e^-$	-1.188
$Ag \rightarrow Ag^+ + e^-$	-0.799
$Cu \rightarrow Cu^{2+} + 2e^-$	-0.340
$H_2 \rightarrow 2H^+ + 2e^-$	0.000
$Sn \rightarrow Sn^{2+} + 2e^-$	0.137
$Ni \rightarrow Ni^{2+} + 2e^-$	0.257
$Ti \rightarrow Ti^{3+} + 3e^-$	1.210
$W + 8OH^- \rightarrow WO_4^{2-} + 4H_2O + 6e^-$	1.259
$Al \rightarrow Al^{3+} + 3e^-$	1.676

Table 3.2: Standard Electrode Potentials for Anodic Reactions[40]

Electrochemical Potentials relative to the NHE of some selected elements is shown in Table 3.2.

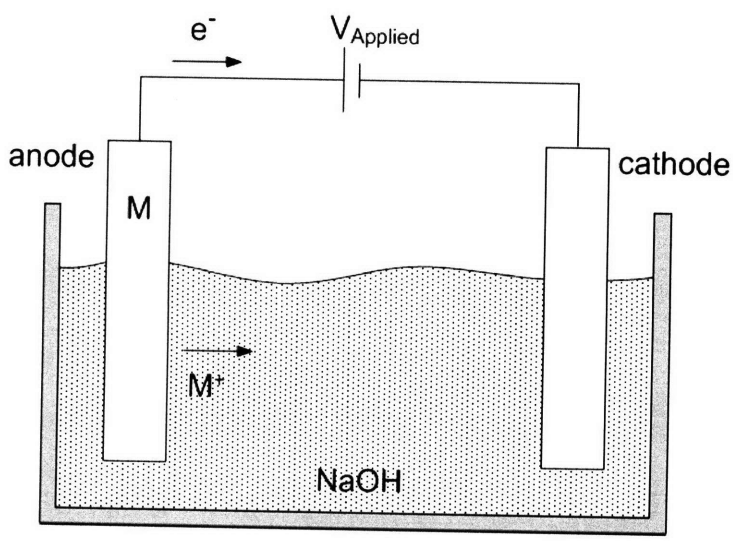

Figure 3-4: Electrochemical Cell

Lets consider a case in which the anode and cathode are composed of the same material. For a general reaction the oxidation reaction at the anode can be represented by the following half cell reaction equation.

$$M = M^{n+} + ne^- \tag{3.1}$$

Where M is the reduced state of the metal, M^{n+} is the ionized metal with oxidation state n and ne^- are the released electrons from the reaction. The reduction reaction at the cathode is the opposite of the oxidation reaction and is written as:

$$M^{n+} + ne^- = M \tag{3.2}$$

Using concepts of statistical thermodynamics we will be able to calculate the equilibrium reduction potential from the standard electrode potential and the reaction species' concentrations. The free energy of a system can be written as:

$$\Delta G = \Delta G_0 + NkT \ln Q_0 \tag{3.3}$$

Where Q_0 is the reaction quotient which, when written as concentrations, is given in our case for the anodic reaction as:

$$Q_0 = \frac{[M^{n+}]}{[M]} \tag{3.4}$$

In addition, the electrical work is equal to the product of the total charge moved and the cell potential and since the free energy of a system is a measure of the energy available to do work, we can write the change in free energy as being:

$$\Delta G = -nFE \tag{3.5}$$

Where n is the number of moles of electrons, E is the cell potential and F is the Faraday constant which is equal to the net charge of 1 mole of electrons. Substituting equation 3.5 into equation 3.3 we arrive at the Nernst Equation:

$$E = E^o - \frac{NkT}{nF} \ln Q \tag{3.6}$$

Since the Nernst equation assumes thermodynamic equilibrium, it does not account for many other effects including catalytic effects, kinetic processes, overvoltages and reaction inhibitions[41]. Section 3.2.1 will explain some of the kinetic processes that are important for our application.

3.2.1 Electrochemical Etching Kinetics

Faraday's Law states that "The amount of substance consumed or produced at one of the electrodes in an electrochemical cell is directly proportional to the amount of current that passes through the cell." This means that the rate of which metal is dissolved at the anode is proportional to the local current density at the anode. This local current density is then the driving factor in determining shape progression during the etch. The local current density is a function of the overall electric potential distribution and of mass transfer effects[20]. For the case of bulk etching through a masking layer, mass transport effects seem to be the limiting factor in etch rates. Madore et. al.[35] gives a good description of how to model the shape evolution during electrochemical etching. The etch rate normal to the anode surface is given by equation 3.7.

$$\delta = \left(\frac{M}{n_v} F \rho\right) \tilde{i}_n \hat{\mathbf{n}} \tag{3.7}$$

Where n_v is the valence of dissolution of the dissolving metal, M is the molecular weight of the dissolving metal and ρ is the density of the dissolving metal. The local current density $(\tilde{i}_n)$ is given through Fick's Law as:

$$\tilde{i}_n = \frac{n_v F D}{\theta} \nabla c \tag{3.8}$$

Where θ is the current efficiency and D is the diffusion coefficient. Madore et. al. then went on to construct a numerical simulation of the shape evolution using a two dimensional boundary element scheme. The results shown in Figure 3-5 show that

the etching is almost isotropic and that it agrees well with actual titanium samples.

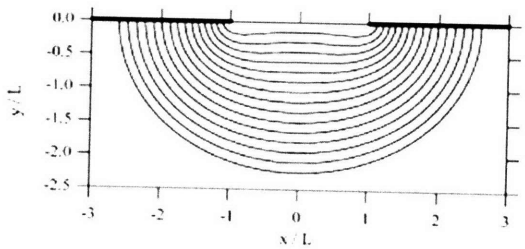

Figure 3-5: Shape Evolution of Through Mask Electrochemical Etching[35]

3.2.2 Electrochemical Etching of Tungsten

The electrochemistry of tungsten is much more complicated than the model that we proposed earlier. Due to tungsten's affinity to oxygen, it will never be able to form a metal-metal system but always a metal-metal to metal-oxide system[22]. In addition there are no pure tungsten cations in solution. Instead tungsten exists in monomer and dimer form bonded with oxygen. Luckily for electrochemical etching, all we care about is how the tungsten is removed from the anode.

The anodic process of elemental tungsten involves the electrolytic dissolution of tungsten through the oxidation process given stoichiometrically in equation 3.9.

$$W + 8OH^- \rightarrow WO_4^{2-} + 6e^- + 4H_2O \tag{3.9}$$

This relatively simple process, like most anodic reactions[41], is the net result of many partial processes for each of the oxidation states as given below[22]:

$$\begin{aligned}
W(s) + 2OH^- &\rightarrow WO^+(s) + 3e^- + H_2O \\
WO^+(s) + 2OH^- &\rightarrow WO_2(s) + e^- + H_2O \\
WO_2(s) + OH^- &\rightarrow WO_3H(s) + e^- \\
WO_3H(s) + OH^- &\rightarrow HWO^{4-}(aq) \\
HWO^{4-}(aq) &\rightarrow WO_4^{2-}(aq) + H_2O
\end{aligned}$$

(3.10)

The cathodic process in $NaOH$[25] or KOH with a stainless steel cathode produces hydrogen gas and is represented by:

$$2H_2O + 2e^- \rightarrow H_2 + 2OH^- \tag{3.11}$$

3.2.3 Electrochemical Etching of Titanium

The anodic process of elemental titanium involves the electrolytic dissolution of titanium through the oxidation process given stoichiometrically in equation 3.12.

$$Ti \rightarrow Ti^{4+} + 4e^- \tag{3.12}$$

A passive oxide layer forms on the titanium surface from the following reaction:

$$Ti + 2OH^- \rightarrow TiO + H_2O + 2e^- \tag{3.13}$$

The cathodic reaction produces oxygen and water:

$$4OH^- \rightarrow O_2 + 2H_2O + 4e^- \tag{3.14}$$

Titanium electrochemical etching can be carried out in a variety of electrolytes shown in Table 3.3. It is interesting to note that the least hazardous etch solution (5M $NaCl$ in H_20) does not perform as well as the more toxic solutions like $3MH_2SO_4$ in Methanol[20].

Composition	Cathode Material	Applied Voltage
$3MH_2SO_4$ in Methanol	Pt	20
1:10 $HCl0_4$ and Perchloric Acid	Pt	20-30[38]
5M $NaCl0_4$ in H_20	-	35 - 50[20]
5M $NaCl$ in H_20	-	20 - 50[20] height

Table 3.3: Titanium Etching Chemistries

Chapter 4

Emitter Fabrication

4.1 Previous Work

This section provides an overview of the previous research conducted in the area of externally wetted emitter arrays at MIT. Simple experiments attempting to hold multiple tungsten needle emitters together, sparked interest in creating large emitter arrays to provide more current. One of these devices contained 31 individual flat needle emitters and is shown in Figure 4-1. While the emitter array succeeded in producing more current, the method was not only tedious to implement, but also suffered from difficult extractor alignment. Additionally, the method could not be practically miniaturized to further increase the current density.

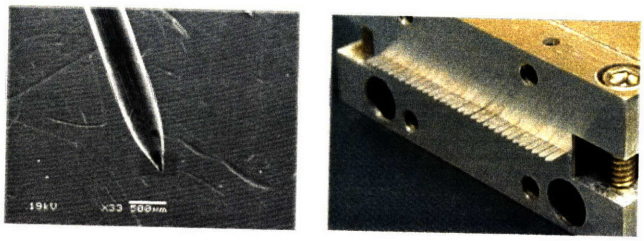

Figure 4-1: A picture of a single needle emitter (left) and of an 31 individual ribbon emitter array (right)

One solution to the alignment problem was to create multiple emitters on a common substrate. This method provides automatic alignment for the emitters as well

as significantly simplified assembly. In addition, the approach, combined with proper microfabrication techniques, has the potential for significant miniaturization. Since the traditional mask-less electrochemical etch techniques for creating needle emitters would no longer work for an array, new methods were explored including laser cutting and through mask electrochemical etching. Figure 4-2a shows emitters formed on a porous silver membrane using a laser cutting technique. The technique produced emitters with very rough edges, which could then be electrochemically smoothed before operation. The method creates uniform emitters with the potential for miniaturization, but the laser cutting process is extremely slow.

Through-mask electrochemical etching was also tested to fabricate emitter arrays. The first attempts used mechanically attached hard masks such as acrylic and kapton to define the emitter geometry. An acrylic clamping mechanism was cut to size using a laser, and clamped to the emitter substrate. This method failed to produce emitters due to the inadequate protection provided by the mask, and the emitters, shown in Figure 4-2c, were etched away before the intended geometry could be formed. To provide better contact between the sample material and the mask, an adhesive kapton tape was then used. Kapton tape was cut to the correct geometry using a laser and attached to the substrate. The resulting emitters (Figure 4-2d) show good transfer of the emitter geometry, but the process cannot be miniaturized because of the need to manually transfer the kapton tape to the substrate.

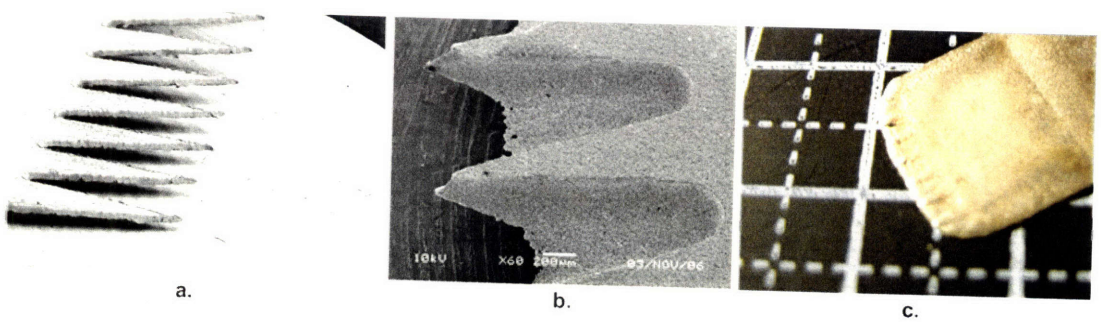

Figure 4-2: Previous Emitter Arrays

The ideal solution would directly pattern a mask on the surface of the tungsten and then use electrochemical etching to create the emitter geometry. This process is

explained in detail in Section 4.4.

4.2 Emitter Material

Tungsten was selected as the emitter material because of prior experience working with it and because it does not react with ionic liquids. The process will work with any material that is able to be electrochemically etched, able to be created with controlled porosity, and that is compatible with the ionic liquids used in electrospray sources (see Section 2.4). Sheets (0.6 mm thick) of sintered porous tungsten with 0.5 and 2.0 μm porosity (Figure 4-3) were obtained from American Elements and a diesaw was used to section the sheets into pieces.

The process that is outlined in the following sections is not limited to tungsten, all that is required is adequate electrochemical etching properties, including mask selectivity and uniformity. Other candidate materials include: titanium, stainless steel and molybdenum, which have been shown to be compatible with ionic liquids. The use of titanium would significantly decrease the thruster mass, and is a good candidate for actual flight hardware. Additionally, all of these materials are able to be sintered to provide porous substrates. The results in this thesis are limited to emitters fabricated from tungsten.

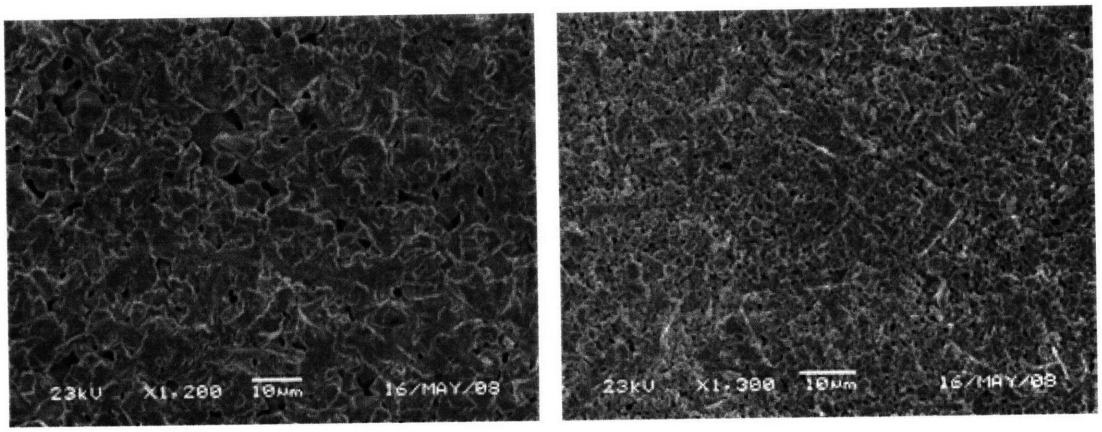

Figure 4-3: Porous Tungsten with 2 μm pores (left) and 0.5 μm pores (right)

4.3 Fabrication Considerations

The desired fabrication process would have to meet the following criteria:

1. Must be compatible with porous media
2. Must be able to create repeatable, uniform emitters
3. Must be able to produce dense arrays at the desired small scales
4. Must leave the emitters clean (particularly in the bulk)

Since common microfabrication techniques rely on the substrate to be planar (or near planar), the process must accommodate the porosity, which is so important to the ultimate application of the emitter arrays. In addition, the process must have the ability to create repeatable and uniform emitters (especially near the emitter tip) so that they all emit at roughly the same voltage. This becomes more and more important as the array sizes get larger. The desired process must have the potential for miniaturization after the initial proof of concept on larger emitters. Also, the process must leave the finished emitters in a clean state where they would be able to function as electrospray emitters. This means that the bulk porosity would have to be clear to allow sufficient fluid flow to the emitter tip and that the surface of the emitters would need to be clear of any intermediate materials used.

4.4 Fabrication Process

The method of fabrication presented here allows for the creation of single emitters as well as larger emitter arrays. Tungsten emitters were fabricated using electrochemical etching with a polyimide film masking layer. Mask fabrication was carried out at the Microsystems Technology Laboratories (MTL) at MIT while etching was conducted at the Space Propulsion Laboratory at MIT. Figure 4-4 shows the main steps in the process. First, the porous media is filled with photoresist, exposed on both sides with UV light, and then developed to create a porous tungsten sample with the porosity

blocked (Step 1). Next, a layer of polyimide is added to the front side and is prebaked to drive off solvents (Step 2). Polyimide was chosen as the masking material for its resistance to Sodium Hydroxide[47] and ability to be precisely patterned using standard photolithography techniques. Additionally, a layer of photoresist is added on top of the polyimide (Step 2). A transparency mask is placed on the photoresist, followed by ultraviolet light exposure (Step 3). The sample is then developed to remove the exposed parts of the positive photoresist and to etch the underlying polyimide thereby transferring the pattern (Step 4). The photoresist is cleaned off the sample and the polyimide is cured in an oven to harden it against the electrochemical etch chemistry. The sample is then electrochemically etched in Sodium Hydroxide until the excess tungsten is removed and the emitter geometry is formed (Step 5). The polyimide is then removed and the emitters are complete (Step 6).

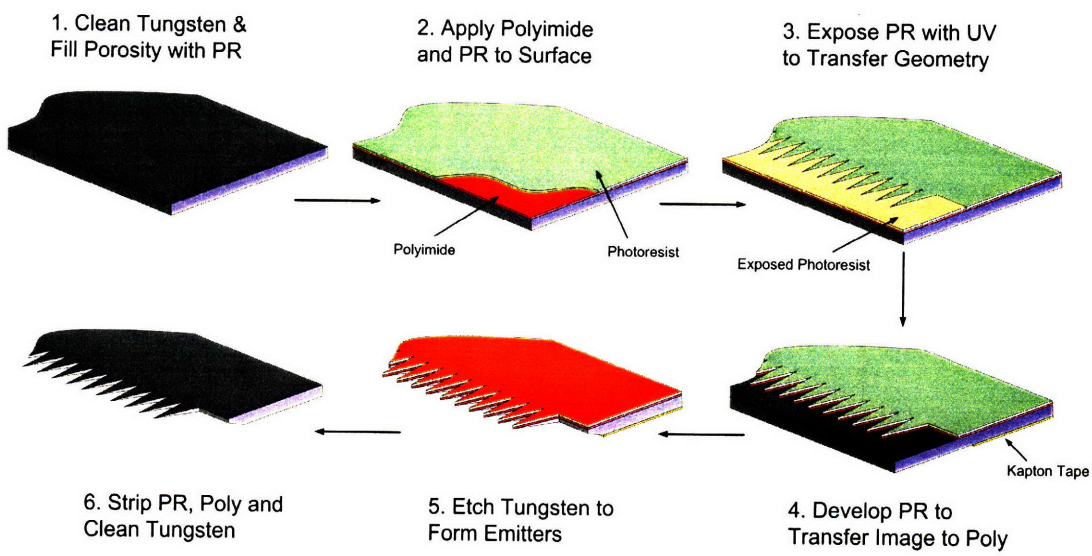

Figure 4-4: Fabrication Process Overview

4.4.1 Blocking the Porosity

One of the largest problems associated with microfabrication on porous substrates is dealing with the porosity itself. When exposed to liquids, just like a sponge, the porous media has a tendency to soak up those liquids due to capillary forces. This is

a problem for two reasons. First, the porosity ultimately needs to be free of foreign material that would inhibit fluid transport to the emitter tip or react chemically with the fluid. Second, the process requires that an even and thin polyimide masking layer be applied to the surface of the tungsten. In initial tests, polyimide was applied to the surface of the tungsten and allowed to fill the porosity during the spin step. While this provided a smooth and even layer of polyimide on the surface, the presence of polyimide in the bulk both slowed down the electrochemical etch and created anisotropic conditions, which led to uneven emitter geometry. Additionally, given the polyimide's resistance to chemical attack, it proved very difficult to remove from the bulk at the end of the process.

In an effort to solve this problem, a sacrificial material was chosen to block the porosity during the polyimide application. Positive photoresist was selected as a material to block the porosity during the application of the polyimide masking layer. It was chosen because of its ability to be removed from the surface through photolithography, while leaving the bulk filled. Following the masking layer application and patterning, the sacrificial photoresist could then be removed using acetone, although there are some problems associated with this method as explained in Section 4.5.

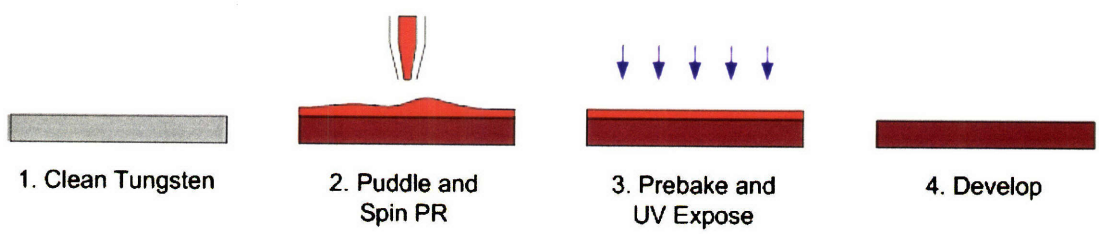

Figure 4-5: Blocking the Porosity

Figure 4-5 shows the main steps in the bulk filling process process. First, Shipley-1827 positive photoresist is applied to the clean tungsten sample using a puddle technique and is allowed to fill the porosity under capillary forces for 5 seconds (1). The sample is then spun at 2000 rpm for 40 seconds on a spincaster to create an even 5 μm layer of resist on the surface. The photoresist is then hardened to drive off solvents using the following prebake protocol: 25 seconds at 65°C on a hotplate, 25 seconds

at 75°C on a hotplate, and 60 seconds at 90°C in an oven (2). The sample is then exposed to UV light for 120 seconds in a 200 watt Karl Suss MJB3 photomask aligner (3). This step breaks down the photoresist on the surface making it susceptible to development. Following this, Microposit MF-319 developer (Rohm-Haas) is used to develop the sample and remove the exposed photoresist leaving behind the photoresist in the bulk (4). During development, the sample is agitated in the developer until bare tungsten is visible.

4.4.2 Applying the Mask

The next few steps in the fabrication process create the polyimide masking layer for the electrochemical etch and are illustrated in Figure 4-6. First, Pyralin PI2556 polyimide (HD Microsystems) was applied to the tungsten surface using a puddle technique and allowed to settle for 10 seconds (5). The sample was then spun at 500 rpm for 15 seconds and then 1500 rpm for an additional 45 seconds to produce a 1.75 μm layer on the surface. The polyimide was then hardened to drive off solvents using the following prebake protocol: 25 seconds at 65°C on a hotplate, 25 seconds at 75°C on a hotplate, 30 seconds at 90°C in an oven, and 30 seconds at 130°C in an oven (6). Next, Shipley-1827 positive photoresist is applied to the surface of the polyimide using a puddle technique (7). The sample was spun for 40 seconds at 1700 rpm to create an $8\mu m$ layer of photoresist. Following the spin, the photoresist was hardened to drive off solvents using the following prebake protocol: 25 seconds at 65°C on a hotplate, 25 seconds at 75°C on a hotplate, and 45 seconds at 90°C in an oven (8). Ideally these steps would have all been done in a programmable oven.

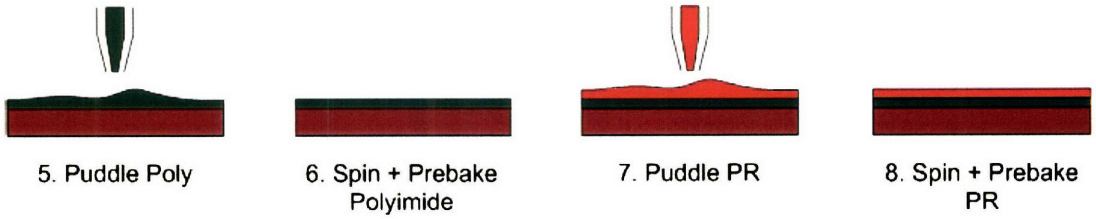

Figure 4-6: Applying the Polyimide Layer

4.4.3 Patterning the Mask

The polyimide layer was patterned indirectly by photolithography with positive photoresist, using a transparency mask to define the geometry. This approach, shown in Figure 4-7, allows the method to be used for very high density arrays with small features on the order of tens of microns. A high resolution transparency mask (obtained from PageWorks, Cambridge, MA) is applied to the surface of the sample (9). The sample is then exposed to UV light for 90 seconds at 200 watts (10). In this step, the UV light breaks down the exposed photoresist, while leaving the unexposed photoresist intact. Next, the transparency mask is removed and the sample is immersed in Microposit MF-319 developer (Rohm-Haas), which selectively removes the exposed photoresist and etches the underlying polyimide (11). Steps 10 and 11, in effect, transfer the geometry from the transparency mask to the photoresist and then from the photoresist to the polyimide.

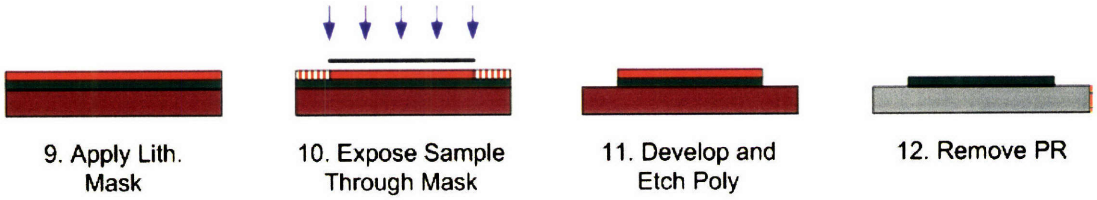

Figure 4-7: Patterning the Polyimide

With the polyimide fully patterned, the photoresist is removed in acetone using the following protocol. First, the sample is spray rinsed with acetone to remove most of the surface PR. It is then immersed in an acetone bath for 20 minutes with a 20 second ultrasonic clean every 5 minutes. This cleaning procedure is repeated four times. To ensure that the photoresist is out of the bulk, acetone is then driven out of the sample for 5 minutes using a vacuum system.

4.4.4 Etching Tungsten

Now with the polyimide masking layer fully patterned, the polyimide is hardened before etching takes place. The sample is placed into an oven with the temperature

controlled by a EuroTherm digital controller. The temperature profile used is as follows: 5 minutes at 100°C in air, 5 minutes at 150°C in air, 5 minutes at 200°C in Nitrogen, 60 minutes at 230°C in Nitrogen, followed by a 30 minute cool down period in nitrogen (13). This procedure drives off the remaining solvents in the polyimide and makes it resistant to the NaOH electrolyte.

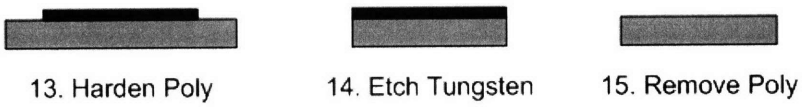

Figure 4-8: Etching Tungsten

The sample is then electrochemically etched using NaOH as the electrolyte and stainless steel as the cathode (14). Best results were obtained with an applied potential of 6 volts and a 1N electrolyte concentration. The etch takes roughly 45 minutes with a 600 μm thick sample. Following completion of the etch, the sample is rinsed with distilled water and is placed in a piranha solution for 30 minutes to dissolve the polyimide. Pirranha consists of a 4:1 mixture of 96% sulfuric acid (H_2SO_4) and 30% hydrogen peroxide (H_2O_2) in water. Fabrication of the emitters is then complete. Figure 4-9 shows images of tungsten samples at various stages in the fabrication process. For some samples a short electrochemical etch is necessary after polyimide removal to smooth out features near the emitter tip. This process is done using the same setup as the primary etching and usually lasts for only a few minutes.

4.5 Fabrication Refinements

Over the course of designing the fabrication process, many refinements were made to both procedures and equipment to address specific issues. This section will explain the most important problems that arose during emitter fabrication and how the process was altered to accommodate them.

The first problem that arose during fabrication concerned the interaction between the polyimide and photoresist. The process requires that both materials be used and

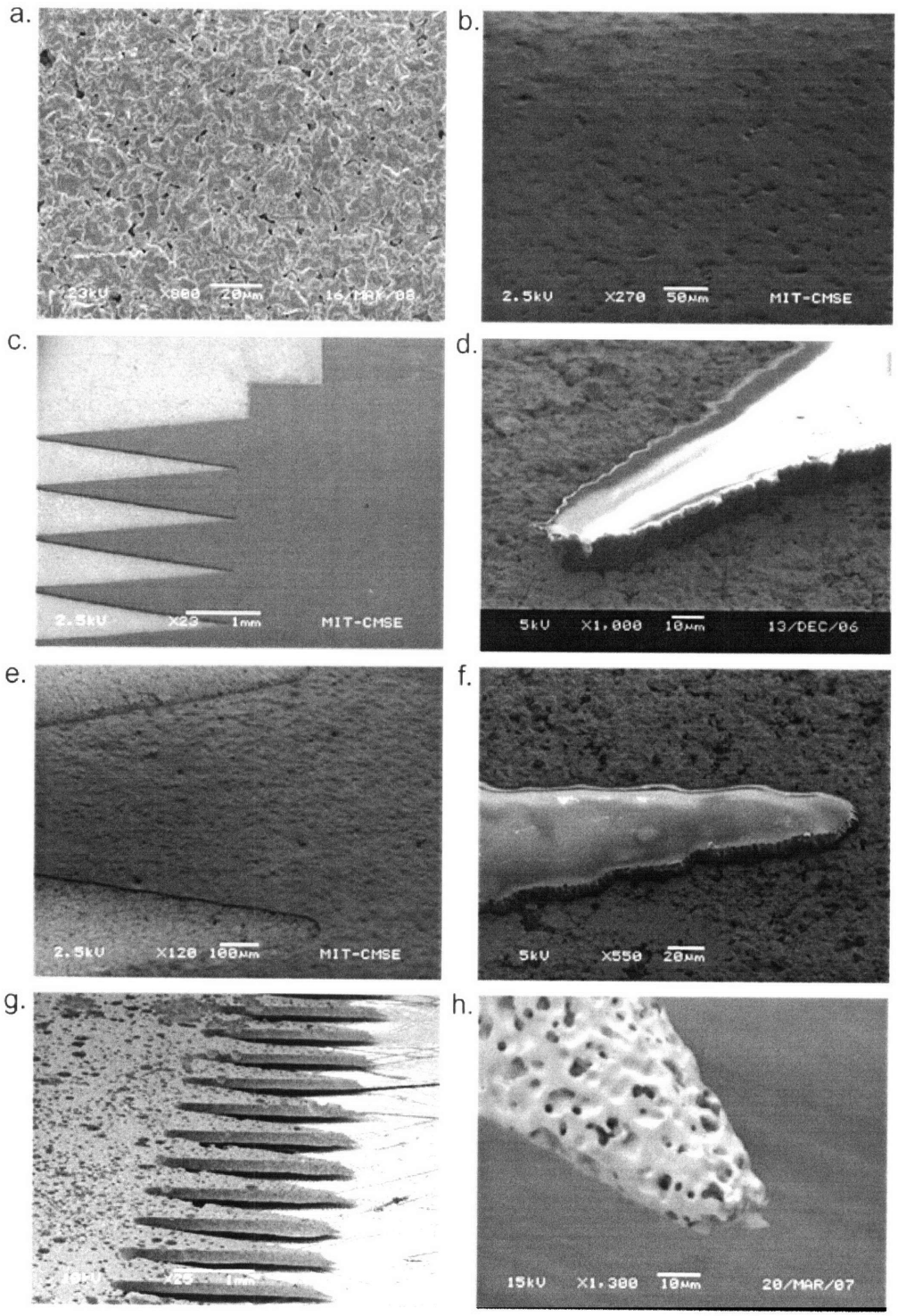

Figure 4-9: Emitter fabrication pictures including: a. clean tungsten showing 2 um porosity, b. 1.75 μm layer of polyimide (step 6), c. and d. polyimide and photoresist patterned into an emitter shape (step 11), e. and f. patterned polyimide on the tungsten surface (step 12), g. and h. finished emitters (step 15)

then selectively removed at certain times without damaging the other material. The critical factor in determining the resistance of the materials to certain solvents is the pre-bake (both duration and temperature profile). During step 6, the polyimide is spun on the sample. The polyimide is then hardened in an oven to drive off solvents and make it immiscible with the layer of photoresist that is spun on in step 8. Additionally, the photoresist is hardened slightly prior to exposure. If the polyimide is subjected to too much heat in steps 6 and 8, then it will become resistant to etching during the development in step 11 and will not be patterned. If the polyimide is not sufficiently hardened in step 6, then the layer will mix with the photoresist during its application, which results in a poor polyimide mask. Additionally, if the temperature rise in the polyimide (step 6) or the photoresist (step 8) is too rapid, then bubbles will form as the solvents try to evaporate, ultimately leaving holes in the polyimide mask. Three examples are shown in Figure 4-10 as well as Figure 4-9d. These problems are largely avoided if the gradual temperature profiles are precisely followed, as outlined in Section 4.4.

A second fabrication problem deals with the removal of the photoresist layer in the bulk (step 12) immediately after the polyimide patterning. It is necessary to remove as much photoresist from the bulk in this step because it acts to inhibit the etch and restricts the flow of ionic liquid during operation. In step 12, acetone is used to selectively eliminate the photoresist, leaving the polyimide layer intact. Photoresist is readily removed from the sample's surface, however, it is harder to remove the photoresist occupying the pores. Two factors that affect photoresist removal include: the total amount of heating of the bulk photoresist and the size of the pores. The current procedure, to a large extent, resolves the problems through careful cleaning prior to the polyimide hard bake. Further ideas to reduce or eliminate this issue, which haven't yet been experimentally verified, are explained in Section 7.2.1.

A third fabrication problem involves etch uniformity. As was explained in Section 3.2, electrochemical etching is ideally isotropic, provided the electrolyte concentration and the surface potential is uniform. During actual etching, fluidic electrolyte currents disrupt this isotropy by providing fresh electrolyte (and anodic discharge ion

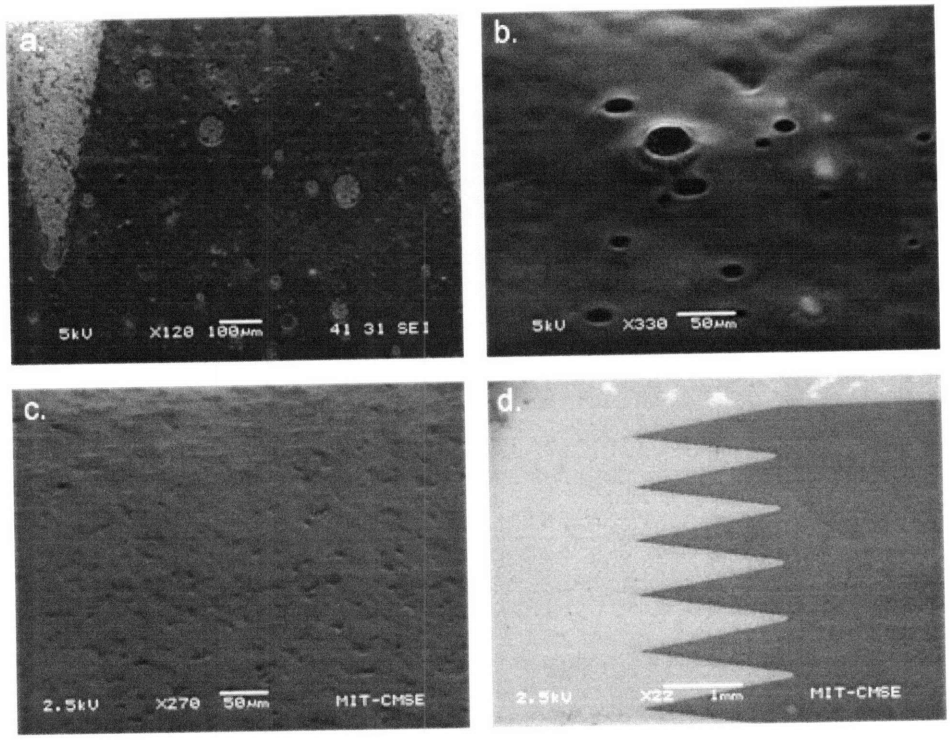

Figure 4-10: Polyimide Mask Examples: a. holes in the polyimide due to poor masking of the photoresist layer, b. holes in the polyimide due to solvents escaping when the sample was heated too rapidly, c. defect free polyimide layer, and d. defect free polyimide mask showing emitter geometry

removal) to certain surfaces, while leaving other areas stagnant. Traditionally, these currents are made insignificant by conducting the etching process in a flow chamber where the electrolyte is constantly regenerating at the etch surface[21].

Two approaches were experimented to improve emitter uniformity. The first etching setup consisted of NaOH electrolyte in a glass beaker with an acrylic cylinder separating the stainless steel cathode plate and the sample. In addition, etching was carried out in an ultrasonic bath, which also improved etching performance. This approach was easy to implement and yielded much better uniformity than conducting the experiment without the acrylic barrier. The second method utilized a flow channel where electrolyte was in constant motion, as shown in Figure 4-11. It consisted of a polyethylene circular flow container with a stainless steel electrode located upstream of the sample. The flow was driven by a DC motor connected to a propeller. This

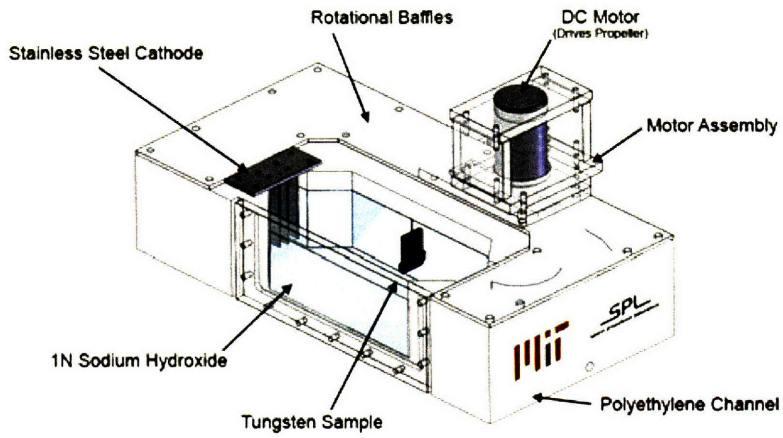

Figure 4-11: Electrolyte Flow Etch Setup

setup yielded better results than the simple beaker etch, but was not noticibly better than the beaker with the acrylic barrier.

4.6 Fabrication Examples

4.6.1 Linear Arrays of Different Packing Density

Linear arrays with varying emitter separation were fabricated to explore the effect of emitter separation on performance. Emitter arrays of three different packing densities were fabricated using the process in Section 4.4. Table 4.1 shows the measured dimensions of three samples of each linear density denoted by χ with units $[\#/mm]$.

The photolithography masks used and the corresponding finished emitters are shown in Figure 4-12.

4.6.2 Linear Array Thruster

A thruster assembly was designed to connect a few emitter sheets together to create a 2D array of emitters. The major design considerations that were considered for the

Sample #	Emitter Length (L) [μm]	Emitter Separation (d) [μm]	# Emitters	χ [$\#/mm$]
1	1138	973	20	1.00
2	1168	958	21	1.00
3	947	982	21	1.00
4	752	737	28	1.33
5	926	730	28	1.33
6	1009	763	28	1.33
7	458	500	44	2.00
8	450	471	44	2.00
9	311	490	44	2.00

Table 4.1: 1D Emitter Packing Array Characteristics

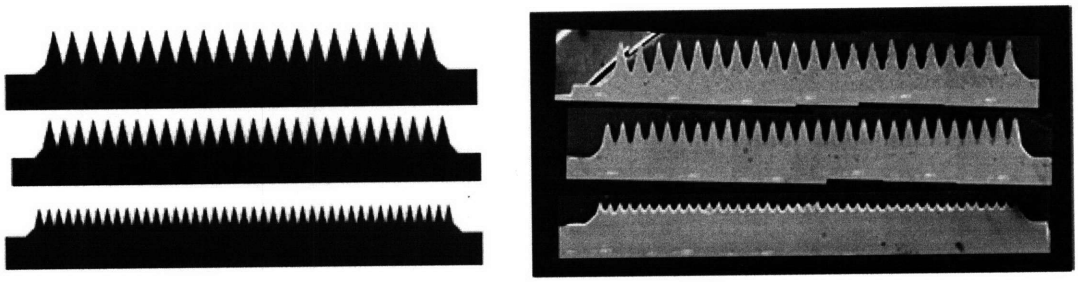

Figure 4-12: 1D Emitter Arrays with Varying Emitter Separation

device are shown below. The assembly must:

1. Provide precise alignment between the emitter sheets and the extractor grid to reduce beam impingement
2. Provide adequate insulation (both electrical and fluidic) between the extractor and emitters to reduce the risk of electrical shorting
3. Use materials which are compatible with ionic liquids for long periods of time
4. Allow for easy assembly to reduce the risk of breaking emitters

The design for the thruster is shown in Figure 4-13. The individual emitter sheets are clamped in place between two bars (50 x 7.87 x 7.87 mm stainless steel). Emitter

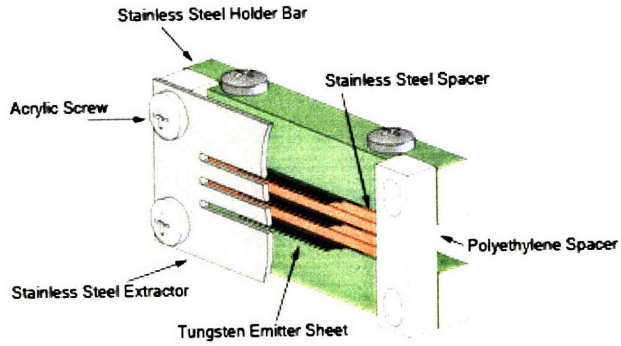

Figure 4-13: Linear Array Thruster Assembly

sheet separation is provided by 1.52 mm thick stainless steel plates cut by a waterjet. The extractor is made from a 0.635 mm thick stainless steel sheet cut by a waterjet. The individual extractor slits are 1.01 mm wide, which gives clearance for a beam spreading half angle of 51 degrees when the emitter tips are aligned to the extractor slit plane. The extractor is attached to the holder bars using two polycarbonate #6-32 screws with two polyethylene spacers. The combination of polycarbonate screws and polyethylene spacers provide electrical insulation between the extractor and emitters and will inhibit the liquid fuel from migrating to the extractor and causing a short. The fabricated thruster is an array of 3 flat needle arrays, each containing up to 18 individual emitters, giving a maximum of 54 emitters with an emitter to emitter separation of 1 mm. In practice, the thruster only had 49 working emitters due to fabrication issues. This gives an emitter density of a little under 0.5 tips per mm^2, which corresponds to an average emitter spacing of 1.5 mm for comparisons with the data in Section 1.3.1. The thruster, as tested, is shown in Figure 4-14 and is approximately 5 x 2.2 x 1 cm. Characterization of its performance was presented at the 30th International Electric Propulsion Conference[24], and is given in Section 6.3.

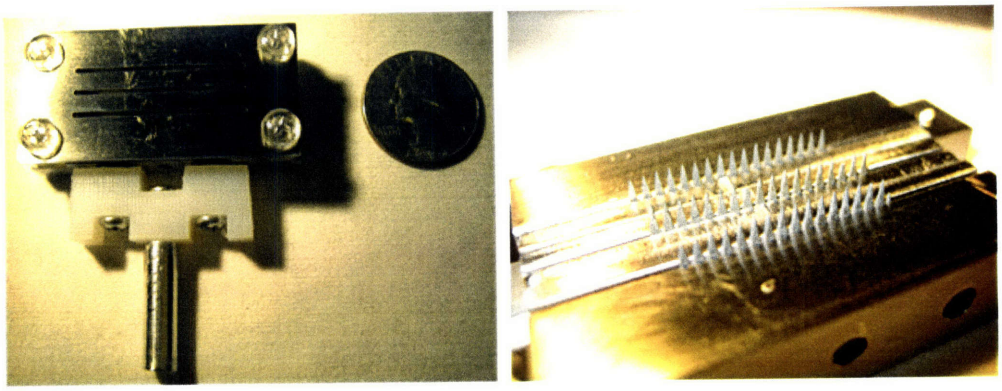

Figure 4-14: 49 Emitter Electrospray Thruster

Chapter 5

Experimental Techniques

This chapter describes some of the experimental methods and techniques which have been used to characterize electrospray emitter performance. It is important to characterize the performance of an emitter or an array of emitters by finding out:

1. What is being emitted: Single gate time-of-flight mass spectrometry is used to determine the composition of the emitted species.

2. How much is being emitted: The performance of the emitters is characterized in terms of the amount of emitted current for different extraction voltages.

3. How this corresponds to thruster performance: A combination of direct thrust measurements and analytical approximations are used to calculate the thrust of the device.

The following sections give an overview of the setup as well as the necessary calculations for such experimental measurements.

5.1 Time-of-Flight Mass Spectrometry

Electrospray thrusters emit charged species with a charge to mass ratio $\frac{q}{m}$ that is directly related to the emitted species velocity through an energy balance. In the ideal case, the kinetic energy of the beam particles after acceleration is equal to the

amount of potential energy lost while accelerating through the applied potential as shown below:

$$\frac{1}{2}mv^2 = q\phi_a \tag{5.1}$$

Where ϕ_a is the accelerating potential. In reality, there are energy losses associated with extracting the ions from the liquid and not all ions are born at the same potential, causing an energy spread in the beam. However, experiments have shown that the beam potential ϕ_B is within 99% of ϕ_a[29]. Equation 5.1 can then be solved for the charge to mass ratio of the emitted species which will be a function of the species velocity, and ϕ_B:

$$\frac{q}{m} = \frac{1}{2}\frac{v^2}{\phi_B} \tag{5.2}$$

By finding the velocity for a given accelerating potential, we can then directly calculate the charge to mass ratio of the extracted species. This allows us to identify the composition of the beam, provided we can infer what the charge of each species is. One method of determining the velocity and then the charge to mass ratio of the particles is through time-of-flight (TOF) mass spectrometry. A simple single gate TOF mass spectrometry setup is shown in Figure 5-1.

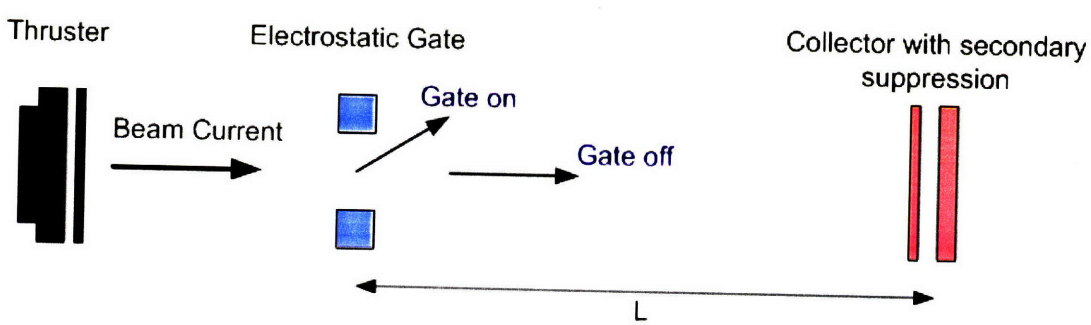

Figure 5-1: Single Gate Time-of-Flight Setup

The time of flight experiment proceeds as follows. First, the microfabricated electrospray emitters produce a beam of charged particles, which are accelerated by

a potential drop ϕ_a between the emitters and the extractor electrode. The emitter is biased to ϕ_a relative to the grounded extractor electrode using a Matsusada AMS-5B6 high voltage power supply (HVPS). The beam of charges particles then travels through an electrostatic gate. When the electrostatic gate is open, the beam passes through and strikes a collector plate located a known distance L downstream of the gate. When the electrostatic gate is closed, the beam is deflected so that none of the current is collected by the collector. The electrostatic gate potential is controlled by a BNC-555 pulse generator, which produces a voltage signal that is then amplified by a DEI PVM-4210 amplifier. The collected current is captured by a collector plate and then amplified with a high speed amplifier before being processed and characterized by an Agilent Infiniium 54835A oscilloscope. Figure 5-2 shows what the oscilloscope current profile looks like in steady state for these two cases. A more detailed description of the time of flight experimental setup can be found elsewhere[34, 30, 28].

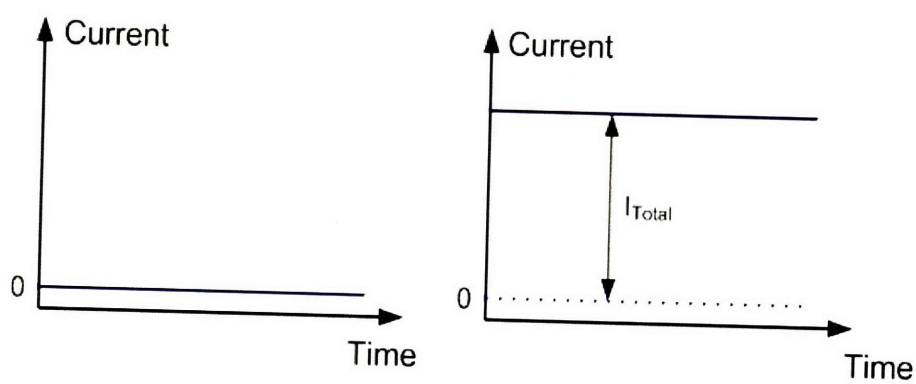

Figure 5-2: Basic Oscilloscope TOF Screens for the electrostatic gate closed (left) and the electrostatic gate open (right).

The TOF experimental procedure starts off with the emitters operating at a constant extractor voltage with the electrostatic gate closed so that no beam current is collected. At time $t = 0$, the electrostatic gate is opened, allowing the beam to proceed to the collector. The emitted species with highest velocity strike the collector first while the slower species begin to strike at progressively later times. This phenomenon is represented by incremental step increases to the current as a function of

time, from which a transit time is measured.

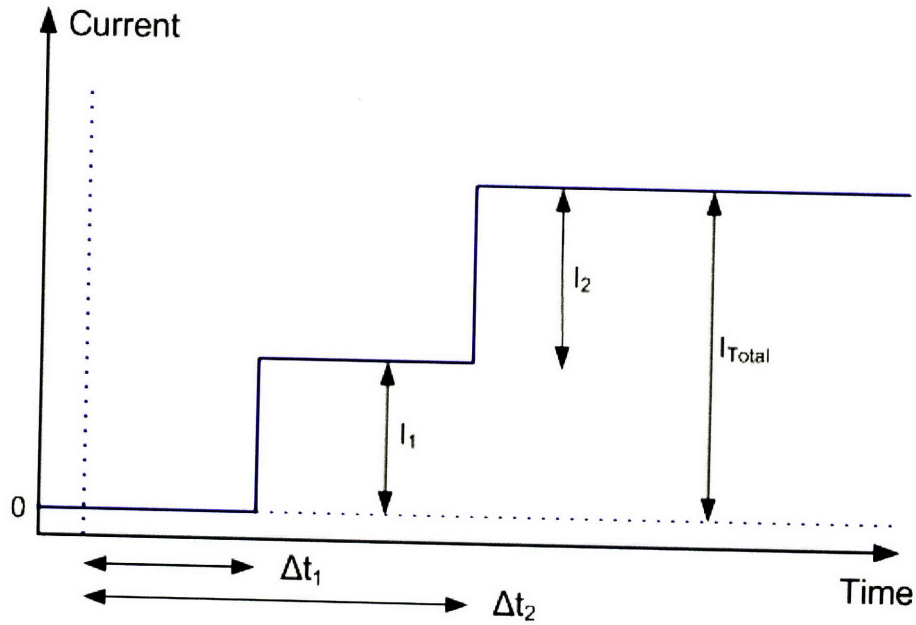

Figure 5-3: Sample TOF Experimental Results

Figure 5-3 shows the time of flight response for an emitter producing two distinct particle species, each with a different charge to mass ratio. The first step increase, which occurs with a time difference Δt_1 after the gate was opened, corresponds to the faster moving species. There is then a time delay before the slower species beam reaches the collector, with a total time delay of Δt_2 from the time that the gate was opened. The charge to mass ratio of the two species is computed using Equation 5.2:

$$\left(\frac{q}{m}\right)_1 = \frac{(L/\Delta t_1)^2}{2\phi_B} \quad , \quad \left(\frac{q}{m}\right)_2 = \frac{(L/\Delta t_2)^2}{2\phi_B} \tag{5.3}$$

Now that the charge to mass ratio is known, and if we assume the charge of the species is known, then we can calculate the corresponding mass and compare with data for the particles that we expect to be in the beam. For instance, if we say that the faster species corresponds to the singly charged ion (monomer), and the slower species is the singly charged ion attached to a neutral ion pair (dimer), then we would calculate the masses as being:

$$m_1 = \frac{2e\phi_B}{(L/\Delta t_1)^2} \quad , \quad m_2 = \frac{2e\phi_B}{(L/\Delta t_2)^2} \tag{5.4}$$

If the emitter is operating in droplet regime, or mixed ion-droplet regime, then the TOF display will be slightly different, as shown in Figure 5-4. Since the droplets have no set charge, and their masses can vary as well, they typically show up as a slow increase in current at much higher transit times than the fast moving ions. In practice it can be difficult to detect droplet emission in the mixed regime, since the current produced by droplets could be significantly less than the ion current. The detection of droplet emission, however, is very important because operating in the mixed ion-droplet emission regime is very costly in terms of emitter efficiency as is explained in Section 2.1.6.

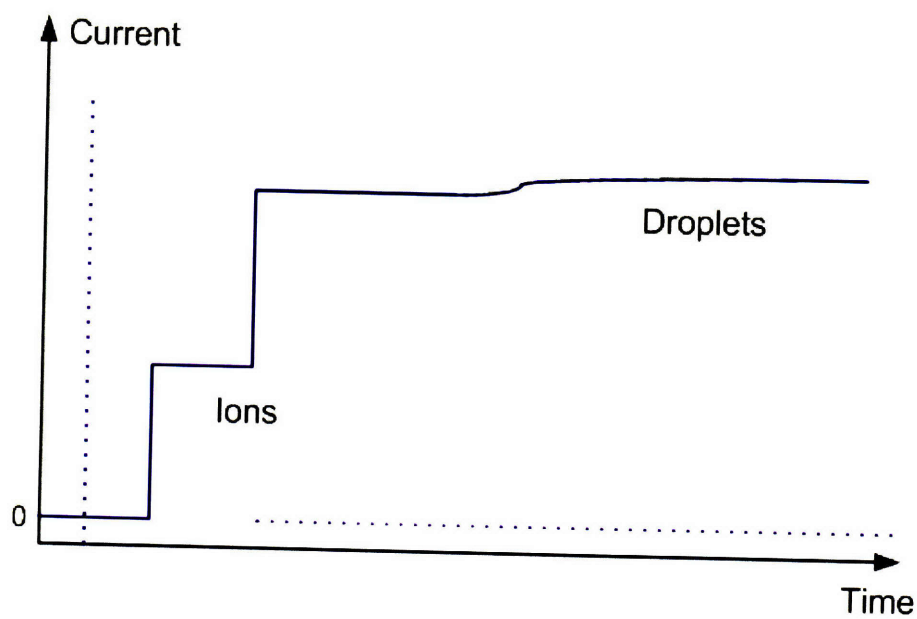

Figure 5-4: Time of Flight Showing Droplet Emission

In addition to identifying the species contained within the beam, we can calculate each species contribution to the total beam current by calculating the ratio of the individual species current to the total current, once steady state has been reached while the gate is off. This allows for the calculation of the polydispersive efficiency as explained in Section 2.1.5. The fractions are given as:

$$f_1 = \frac{I_1}{I_t} \quad , \quad f_2 = \frac{I_2}{I_t} \tag{5.5}$$

5.2 Emitted Current Measurements

Basic current measurements were conducted using the experimental setup shown in Figure 5-5. The setup consists of the emitter-extractor assembly and a collector plate. The emitter is connected to a Matsusada AMS-5B6 high voltage power supply (HVPS), capable of supplying up to 5 kV in both polarities. The output of the HVPS is controlled by a Agilent 33220A Arbitrary Waveform Generator. The extractor electrode is connected to ground, and the collector plate is connected to a Keithley 6517 Electrometer and is biased to positive 50 volts to suppress secondary electron emission. The electrometer sends current measurements to a computer through its digital GPIB interface. Additionally, the current going to the emitter is monitored my a Meterman 37XR multimeter that measures the voltage drop through a resistor. By measuring the current going to the emitter as well as the collected current, we are able to indirectly measure the amount of current that is intercepted by the extractor.

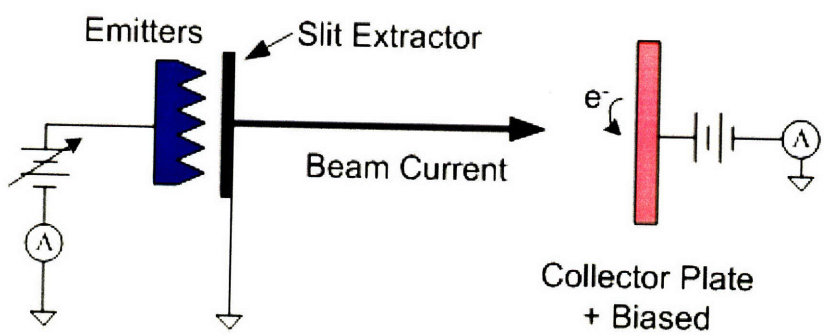

Figure 5-5: Current Measuring Setup

Some common experiments that are implemented to characterize performance are shown below. The accelerator voltage profile shown in Figure 5-6a is used to measure how much current is being emitted at various accelerating voltages. The polarity of the accelerating voltage is changed at between 1 and 0.5 Hz to avoid a buildup

of one species of ions on the surface of the emitter, which has been shown to cause electrochemical reactions[32]. The corresponding collected current profile is shown in Figure 5-6b, and consists of roughly two second steps of increasing voltage for both polarities, repeated twice. Before each voltage sweep is performed, a few initialization pulses of the highest voltage magnitude to be tested are performed to make sure that the emitters are wetted uniformly for each trial. At the lower voltages we see no measurable emission from the device, but at a critical voltage V_s, emission occurs. The emission increases with higher extraction voltages as more ions are extracted from the liquid.

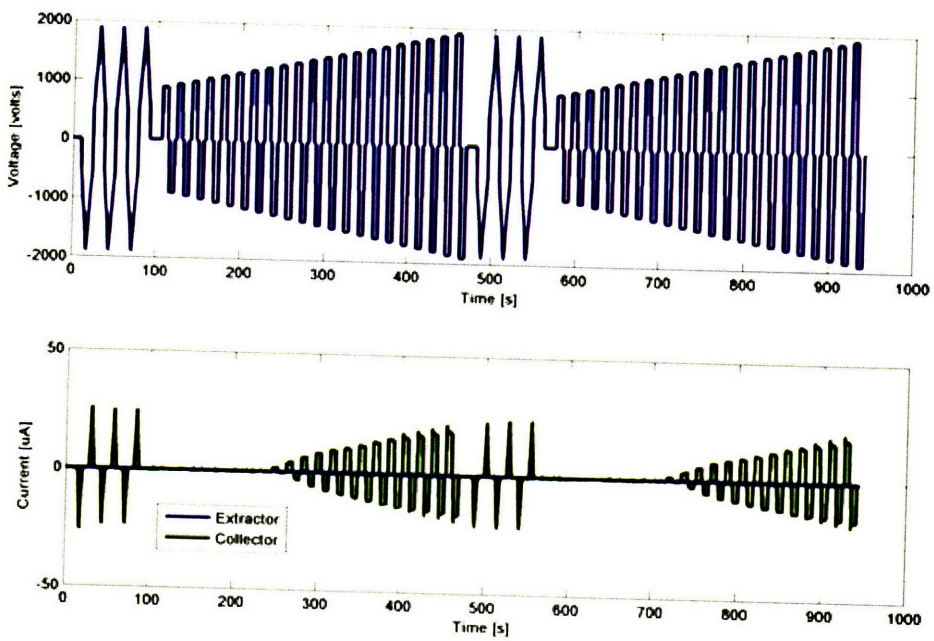

Figure 5-6: Sample Experimental Voltage Sweep Including: a. the extractor voltage profile, and b. the resulting collected current.

The emitted current data is taken from each voltage level and is averaged, excluding the initial transient. Figure 5-7 shows a sample collected current profile for a given accelerating potential, and where the data was averaged.

The experimental steady state current is averaged in such a way for each extraction voltage step and is then averaged again between the different runs.

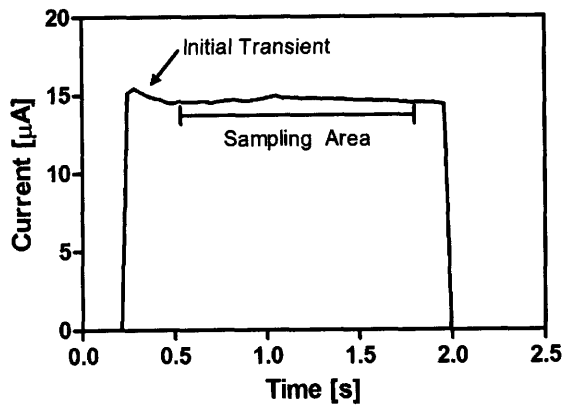

Figure 5-7: Averaging Current Measurements

5.3 Thrust Measurements

When possible, direct thrust measurements were conducted at the Busek Company, Natick, MA. The thrust measurements were performed using a torsional balance capable of measuring sub μN forces[13].

When it was not possible to conduct direct measurements, the thrust produced by the emitters was estimated using the emitted current and results from the TOF experiments. The thrust can be written as a function of the ion velocity times the mass flow rate of the device:

$$F = \dot{m}c \tag{5.6}$$

Where c is the ion velocity and is obtained through the ideal energy balance:

$$c = \sqrt{2\left(\frac{\bar{q}}{m}\right)\phi_a} \tag{5.7}$$

Where $\frac{\bar{q}}{m}$ is the average charge to mass ratio of the emitted species and ϕ_a is the accelerating potential. Using the accelerating potential for these calculations is only an approximation since there is usually some loss during extraction and acceleration. It has been previously seen that ϕ_a approximates the beam potential to within 99 %.

[29]. The final thrust equation is then given as:

$$F = \frac{I}{\sqrt{\left(\frac{\bar{q}}{m}\right)}}\sqrt{2\phi_a} \tag{5.8}$$

The specific impulse of the emitters can also easily be estimated as:

$$I_{sp} = \frac{c}{g_0} = \frac{1}{g_0}\sqrt{2\left(\frac{\bar{q}}{m}\right)\phi_a} \tag{5.9}$$

5.4 Vacuum System and Lab Facilities

The vacuum system used for all tests was a cylindrical chamber with an inner diameter of 197 mm and length 495 mm. A stainess steel extension with an inner diameter of 56 mm and a length of 365 mm was installed to increase the accuracy of TOF experiments. Roughing was provided by a Varian SD-40 mechanical pump while two Varian V-70 tubo pumps were used to ultimately reach pressures of 10^{-6} torr. Pressures were monitored using a Varian ionization guage controlled by a Varian multiguage. All experiments were conducted at less than 10^{-6} torr to avoid beam interactions with neutrals. Figure 5-8(left) shows the vacuum chamber. The chamber has one primary access hatch, a viewing window, and a variety of feed through lines including, two high voltage feeds, two coaxial feeds and numerous other pin feeds.

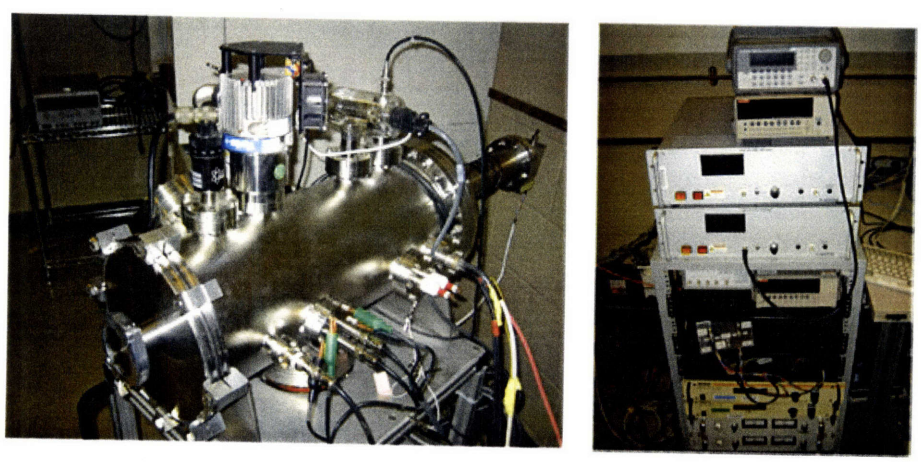

Figure 5-8: SPL Vacuum Chamber (left) and Electronics Stack (right)

Oscilloscope	- Agilent Infiniium 54835A
Function Generator	- Agilent 33220A
Electrometers	- Keithley 6517
	- Keithley 6514
	- Meterman 37XR
HV Power Supplies	- Matsusada AMS-5B6
	- Bertan 205B-05R
	- Bertan 205B-10R
Pulse Generator	- BNC-555
Pulse Amplifier	- DEI PVM-4210

Table 5.1: SPL Electronic Equipment

The electronics that were used for most experiments were all contained in the electronics rack shown in Figure 5-8(right). Table 5.1 lists the individual devices.

All experiments were conducted using in-house LabView scripts, with connections to the experimental devices provided by the digital GPIB interface or the analog NI-DAQ voltage aquisition card.

5.5 High Voltage Current Measurements

Experiments which required the monitoring of current at high voltages, such as the total current going to the emitters, was either monitored using multimeters, or was monitored using an in house high voltage to low voltage signal converter. The diagram of the device is shown in Figure 5-9. The high voltage input signal is driven across a resistor to create a voltage difference. The signal is then processed by an OPA-277 op amp and is then sent to a HCPL-7800A isolation amplifier which converts the high voltage signal to a low voltage signal. The maximum allowable voltage input to the isolation amplifier is 200 mV, which means that the load resistor will need to be selected for different expected current ranges. The signal is then processed by two more OPA-277 amplifiers to reduce noise before it is outputted as a low voltage signal with a gain of roughly 10. Figure 5-10 shows the finished device with all the components placed on the printed circuit board.

The performance of the device was tested at various biasing voltages, and the

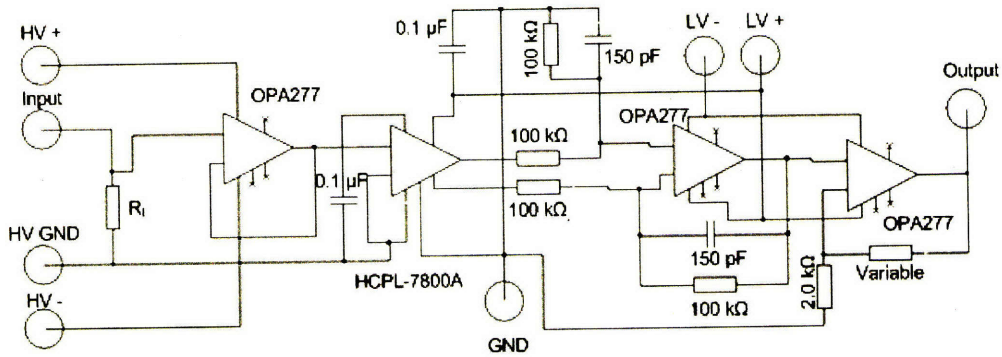

Figure 5-9: High Voltage Current Measuring Device Schematic

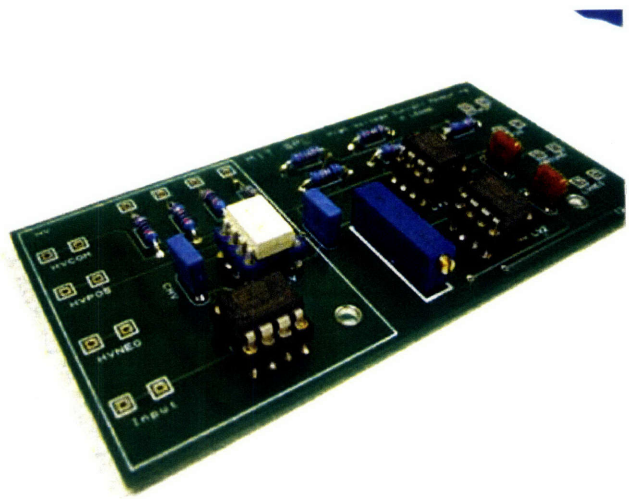

Figure 5-10: High Voltage Current Measuring Device PCB

results are shown in Figure 5-11. We see that the device gives good performance (within 2%) for for input voltages from 50 to 200 mV, with increasing accuracy as the input voltage is increased. As the input voltage is reduced below 50 mV, the accurracy drops off. The device is therefore suitable for experiments where precise current measurements at high voltages are needed, provided we stay in the 50 to 200 mV input region, which is possible by varying the load resistor. The current ranges that the device was designed for are shown in Table 5.2.

Current Range [μ A]	Load Resistor [kohm]
0.025 - 0.1	2000
0.25 - 1	200
2.5 - 10	20
25 - 100	2
250 - 1000	0.2

Table 5.2: High Voltage Current Measurement Ranges

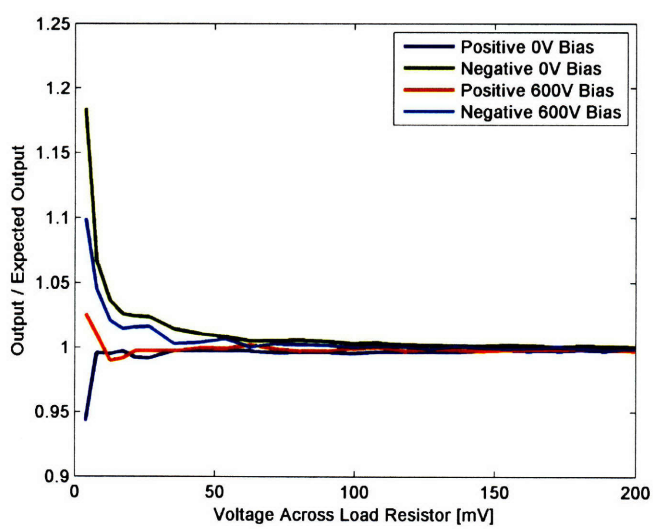

Figure 5-11: Gain Response for the HV Converter at Various Biasing Levels

Chapter 6

Experimental Results

6.1 Experimental Overview

Experimental characterization of fabricated emitters and emitter arrays was carried out in the Space Propulsion Lab at MIT, and some thrust measurements were conducted at Busek Corporation, Natick, MA. The chapter is divided into three sections. The first section provides some of the initial data obtained by testing the initial arrays fabricated. Included is time of flight mass spectrometry data for the ionic liquids EMI-BF_4 and EMI-IM. The second part of the chapter explains tests conducted on a 49 emitter demonstration thruster built to showcase the benefits of emitter clustering. The last part of the chapter presents the results of experiments performed to characterize the effect of emitter density on operation.

6.2 Initial Emitter Results

6.2.1 Emitted Current

The amount of emitted current per emitter for three arrays containing between 5 and 6 individual emitters was obtained for extraction voltages between 1.0 kV to 3.0 kV. is shown in Figure 6-1. We see that from a starting voltage of 1.1 kV to a maximum applied voltage of 3 kV, we obtain a roughly linear increase of emitted current up to

a maximum of 10 μA per individual emitter.

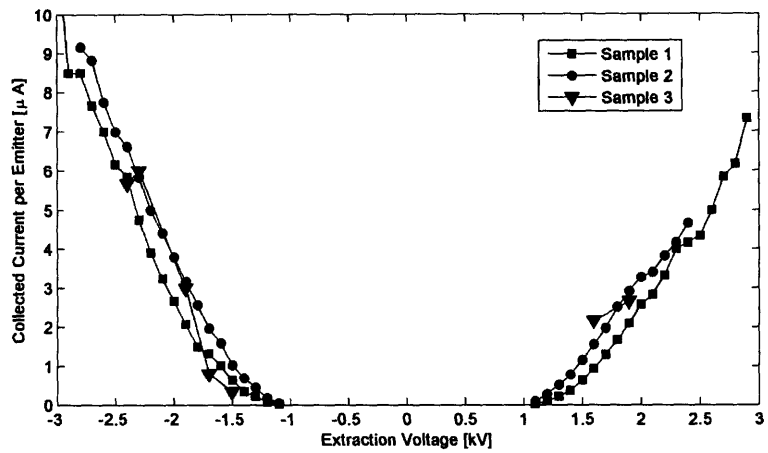

Figure 6-1: Current vs. Voltage Plots for Three Small Emitter Arrays

6.2.2 Time of Flight

The time-of-flight technique explained in Section 5.1 was used to determine the composition of the emitted beam on a single flat needle array containing 6 emitters for EMI-BF_4 as well as EMI-IM.

EMI-BF_4

The time of flight curves for positive (1915.28 V) and negative (-1898.33 V) emission are shown in Figure 6-2 for EMI-BF_4. Both graphs show two steps indicating the presence of two distinct ionic species in the beam. The presence of droplets was not seen in any of the results. From the drift time measured for the particles to travel between the given distance between the electrostatic gate and the detector ($L = 751.57mm$) we can calculate the specific charge ratio using Equation 5.3 and subsequently the mass of the species using Equation 5.4. As an approximation, the on-axis accelerating potential is taken to be equal to the extraction potential which is a fairly good approximation, as explained in Section 5.1. The results for EMI-BF_4 are tabulated in Table 6.1 and show that roughly equal current contributions are made by the monomer and dimer in each polarity.

In addition we can calculate the contribution of each ion species to the total current by looking at the relative changes in measured current during the time-of-flight tests. The results closely agree with previous time of flight experiments with EMI-BF_4 in both cylindrical needle emitters[34] and with arrays of single flat emitters[30]. The lack of an elongated increase in current following the ion steps also indicates that there is not a significant amount of droplets contributing to the emitted current, although data was only taken for 100 μs. If we assume that droplets would have a charge to mass ratio of around 10000 C/kg, then we would expect that they would have a TOF of 121 μs which would not be captured in this analysis. In future experiments, we will look for droplet emission by increasing this time.

Polarity	**TOF** (μs)	**Mass** (amu)	**% of Total Current**	$\frac{q}{m}$ C/gr	**Corresponding Ion**
Positive	13.9	112.40	42.58	430.6	$[EMI]^+$
(1915.28 V)	22.8	310.15	57.42		$[EMI\text{-}BF_4][EMI]^+$
Negative	12.4	89.49	49.13	513.9	$[BF^-]$
(-1898.33 V)	21.9	287.28	50.87		$[EMI\text{-}BF_4][BF^-]$

Table 6.1: Emitted Beam Composition for EMI-BF_4

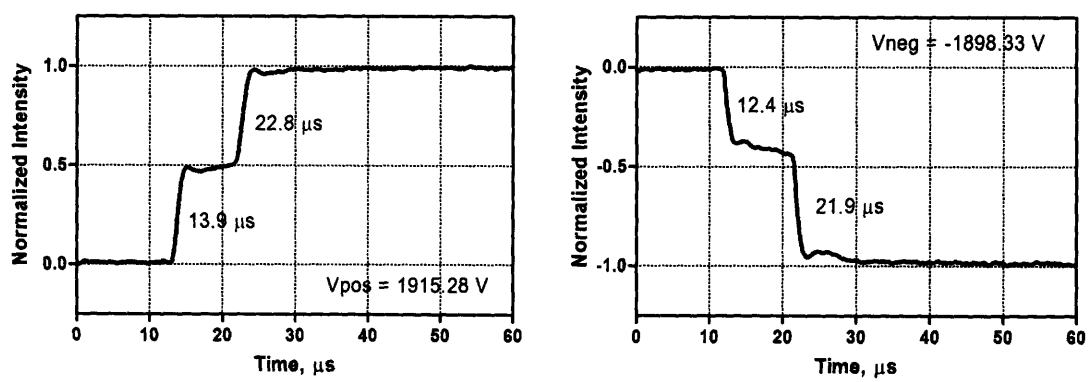

Figure 6-2: Time-of-flight spectra showing the presence of two families of ions for each polarity for the ionic liquid EMI-BF_4

Plotting the slope of the TOF curve allows us to better characterize the spread of the experimental results. Figure 6-3 shows the results for the negative mode (-

1898.33 V), while Figure 6-4 shows the results for the positive mode (1915.28 V). We see that the full width half max (FWHM) values are on the order of 1-1.5 μs and is due to either amplifier induced noise or by an actual energy spread in the emitted beam. Previous studies using an RPA have seen that the normal spread in the beam potential is on the order of 7-8 eV[29]. To solve for the expected time spread corresponding to the potential spread, we first write the ion energy balance:

$$\frac{1}{2}m_i\left(\frac{L^2}{t^2}\right)^2 = qV \tag{6.1}$$

We can then take the derivative of this expression:

$$-\frac{m}{t}\left(\frac{L^2}{t^2}\right)\Delta t = q\Delta V \tag{6.2}$$

If we then note that:

$$\frac{L^2}{t^2} = \frac{2qV}{m} \tag{6.3}$$

Then the following relationship exists to relate the spread in beam potential to the spread that we should see in the data.

$$\Delta t = \frac{1}{2}t\frac{\Delta V}{V} \tag{6.4}$$

If we say that $\Delta V \approx 8$ eV, and for an accelerating voltage of 1900 V, then we would expect:

$$\Delta t \approx 0.04\mu s \tag{6.5}$$

This means that the spread that we see in the TOF data corresponds to the bandwidth of the amplifier and not the energy distribution of the beam.

EMI-IM

Time of flight experiments were also carried out for EMI-Im in the negative polarity at an extraction voltage of -1900 V. The time of flight curve, shown in Figure 6-5, shows that there are two peaks corresponding to the monomer and dimer. The

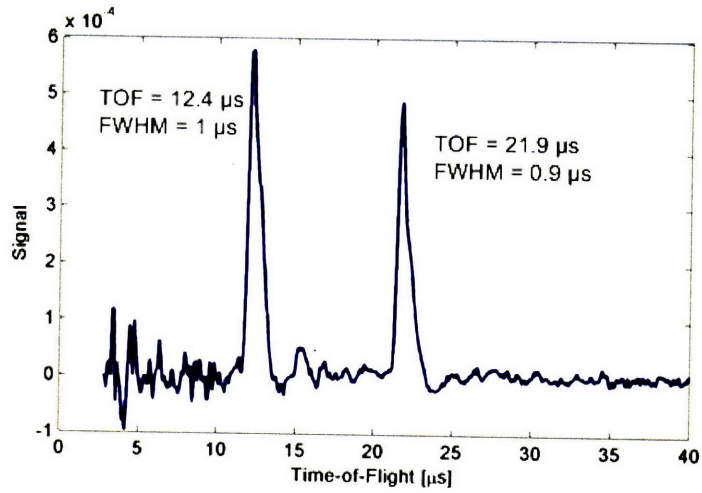

Figure 6-3: TOF Signal Spread for EMI-BF_4 in the Negative Mode

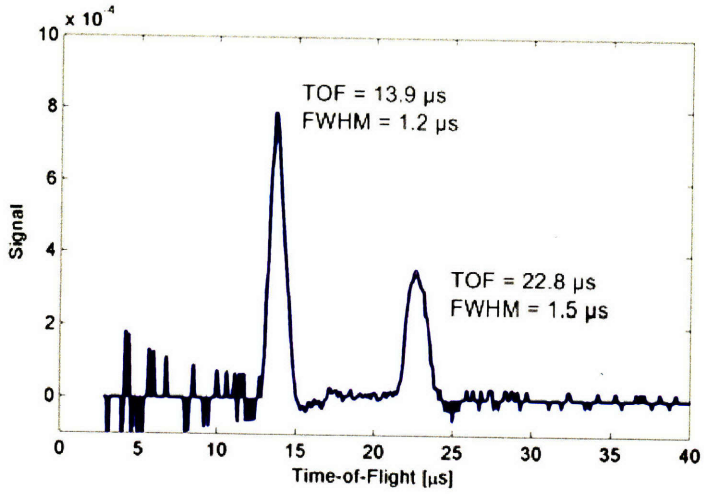

Figure 6-4: TOF Signal Spread for EMI-BF_4 in the Positive Mode

corresponding calculated values for the ionic species present in the beam current are shown in Table 6.2.

Figure 6-6 shows the derivative of the time of flight signal, where the two peaks correspond to the two different ionic species that have been emitted. We also see that the FWHM values are, again, much higher that what would be caused by a typical energy spread and is therefore caused by the bandwidth of the amplifier.

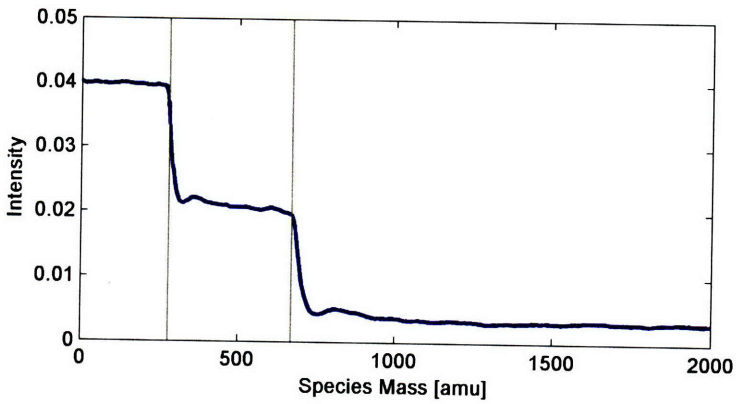

Figure 6-5: Time-of-flight spectra showing the presence of two families of ions (monomer and dimer) for the ionic liquid EMI-IM at -1900V extraction voltage

Polarity	TOF (μs)	Mass (amu)	% of Total Current	$\frac{q}{m}$ C/gr	Corresponding Ion
Negative	21.4	280.13	52.43	466.38	[IM$^-$]
(-1900 V)	33.1	693.96	47.57		[EMI-IM][IM$^-$]

Table 6.2: Emitted Beam Composition for EMI-IM

6.3 One-Dimensional Demonstration Thruster

A 49 emitter demonstration thruster was created from three linear emitter arrays to demonstrate the capabilities of grouping many electrospray emitters together. Some of the work in this section was presented at the 2007 International Electric Propulsion Conference in Florence, Italy[24].

6.3.1 Thrust and Current Measurements

Thrust measurements were conducted at the Busek Company, Natick, MA. The measurements were performed using a torsional balance capable of measuring sub micro newton forces[13]. The results, shown in Figure 6-7, show that the thruster produced from $0.82\mu N$ to $2.33\mu N$ in the -1282 to -2088 V negative extraction voltage range and from $1.08\mu N$ to $5.67\mu N$ in the 1391 to 2437 V positive extraction voltage range. This corresponds to a thrust per emitter tip of $0.048\mu N$ at -2088 V and $0.116\mu N$ at 2437 V. The leveling off of thrust in the negative mode is potentially due to the

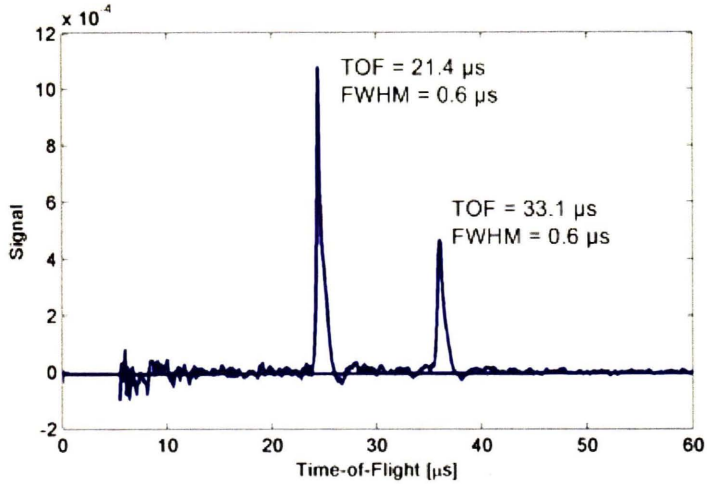

Figure 6-6: TOF Signal Spread for EMI-IM in the Negative Mode

thruster approaching the limit of its ability to transport liquid to the tip, although the results from Section 2.3 show that this would not be a problem with transport through the bulk porosity. It could, however, be an issue with the liquid reaching the base of the emission region for the emitters.

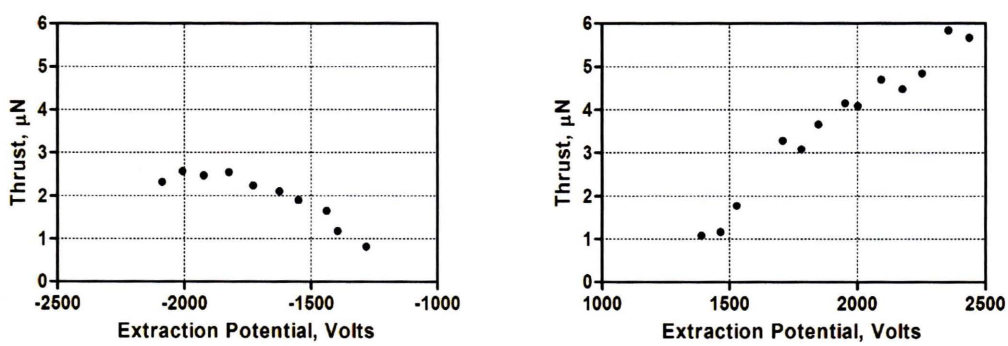

Figure 6-7: Thrust Produced by a 49 Emitter Thruster

The current as a function of extraction voltage was also monitored during the experiments. Figure 6-8 shows the beam current, current leakage to extractor and collected current as a function of extractor voltage. It is seen that a small fraction of the beam current is lost to the extractor which is due to beam impingement. Current that is lost to the extractor is not used for making thrust, and in future designs the extractor geometry may be changed and a better system of alignment will be tested

to reduce impingement. The amount of current that is in the beam corresponding to the direct thrust measured, can be analytically calculated using Equation 6.6).

$$\frac{F}{I_B} = \sqrt{\frac{2\phi_B}{(\hat{q}/m)}} \tag{6.6}$$

Where $(\hat{q}/m)$ is known from the TOF experiments and the beam potential (ϕ_B) is approximately equal to the applied potential. The results are plotted in Figure 6-8 and show that the measured beam current is somewhat different than expected. In addition, most noticeably in the positive mode, there is some beam current that is not accounted for in the extractor current and collected current. This is likely due to the effect of secondary electrons caused by the high energy ions hitting the extractor and the collector since the setup at Busek did not include a biased collector plate. These electrons migrate back to the emitters and cause the beam current to be artificially increased.

The specific impulse of the device calculated from the thrust measurements can be computed using the following relation:

$$I_{sp} = \frac{F}{g_0 I_t}\left(\frac{\bar{q}}{m}\right) \tag{6.7}$$

Where I_t is the current that is going to the emitters. Figure 6-9 shows this specific impulse as well as the specific impulse if there was no current hitting the extractor $(I_B = I_t)$. We see that the specific impulse in the negative mode is around 3000 seconds while the specific impulse in the positive mode is between 4000 and 5000 seconds.

6.4 One-Dimensional Packing Density

The work in this section was presented at the 2008 Space Propulsion Conference in Heraklion, Greece[23]. To characterize the performance of electrospray arrays when the spacing between emitters is reduced, and the emitter density is increased, tests

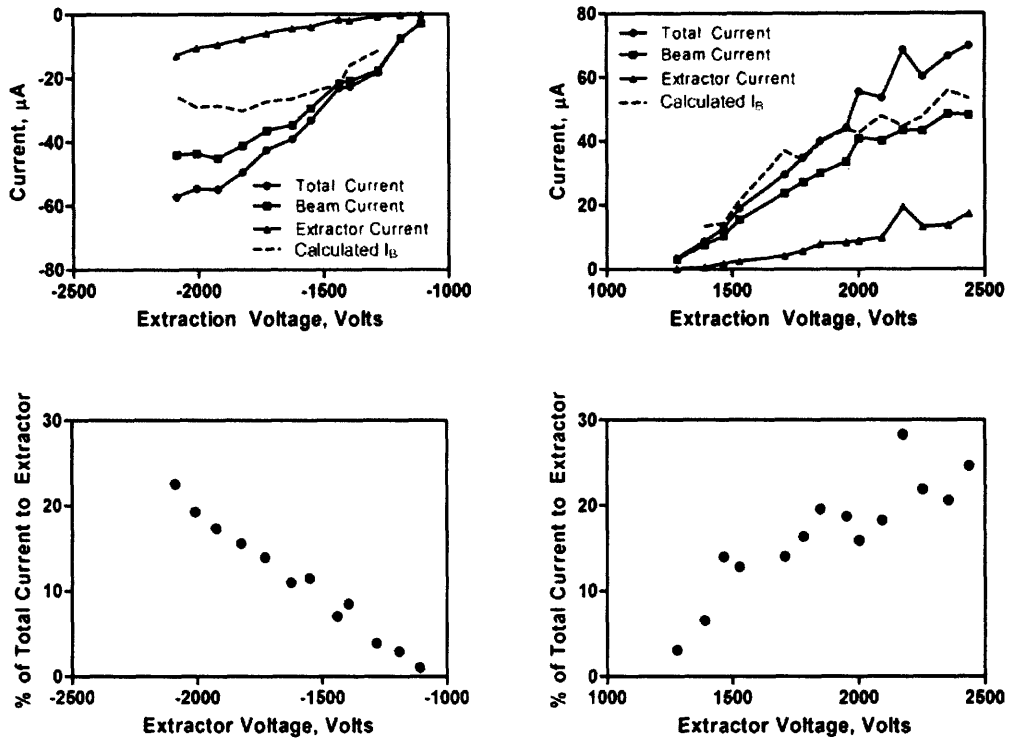

Figure 6-8: Current vs. Extraction Voltage

were performed on linear emitter arrays of different packing density. The emitter arrays were fabricated using the process outlined in Section 4. Details of the geometry for the emitter arrays are also provided in Section 4.6.1. The emitter density χ is measured in the number of emitters per mm.n Experimental results are provided for samples of each emitter density and show that the emitter arrays produce between 0.5 to 1.5 μA of current per emitter. A normalization scheme is then implemented to directly compare data between emitters with different geometry and emitter densities. Numerical simulation results were used to account for reductions in the electric field at the emitter tip due to close emitter packing. The normalized data shows that each sample emits similar current per emitter. This result highlights the potential for electrospray clustering and miniaturization.

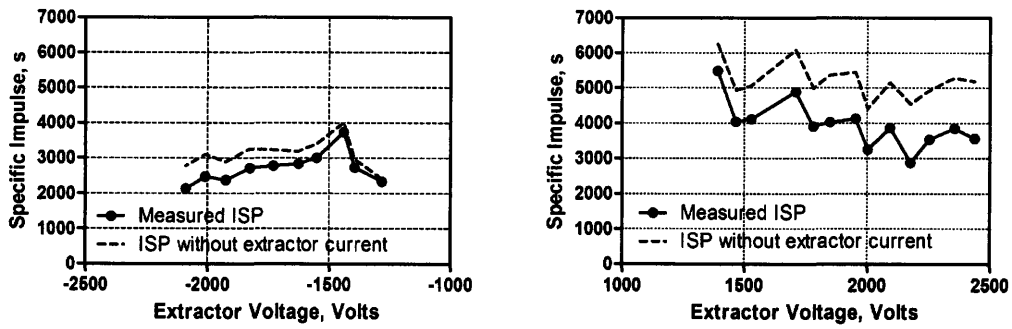

Figure 6-9: Specific Impulse

Sample	# Emitters	Max Current $[\mu A]$	Voltage $[kV]$	Thrust $[\mu N]$	I_{sp} $[s]$
1	20	17.9	2.2	1.7	4850
2	21	32.0	1.9	2.8	4500
3	21	18.5	2.2	1.7	4850
4	28	31.6	2.1	2.9	4740
5	28	41.7	2.2	3.9	4850
6	28	22.1	1.7	1.8	4260
7	44	46.8	1.9	4.0	4500
8	44	18.8	1.9	1.6	4500
9	44	26.7	2.2	2.4	4850

Table 6.3: 1D Emitter Performance Characteristics

6.4.1 1D Emitter Array Performance

Table 6.3 shows some characteristic performance indicators for each emitter array tested. Included are the maximum current values obtained and the extraction voltage. Also included is an estimate of the thrust of the device at the given current level and the specific impulse, computed using Equations 5.8 and 5.9, respectively.

6.4.2 Normalization of Data

Three arrays of each emitter density were characterized during this experiment. Of the three arrays, one was selected from each density for comparison based on similarities in tip geometry. The current per emitter vs. applied voltage plots, displayed in Figure 6-

10, show that each emitter array produced between 0.5 to 1.5 μA per emitter at the higher applied voltages. To appropriately compare the data, a non-dimensionalization scheme is implemented by defining a characteristic voltage (V^*) and a characteristic current (I^*) which are functions of emitter geometry.

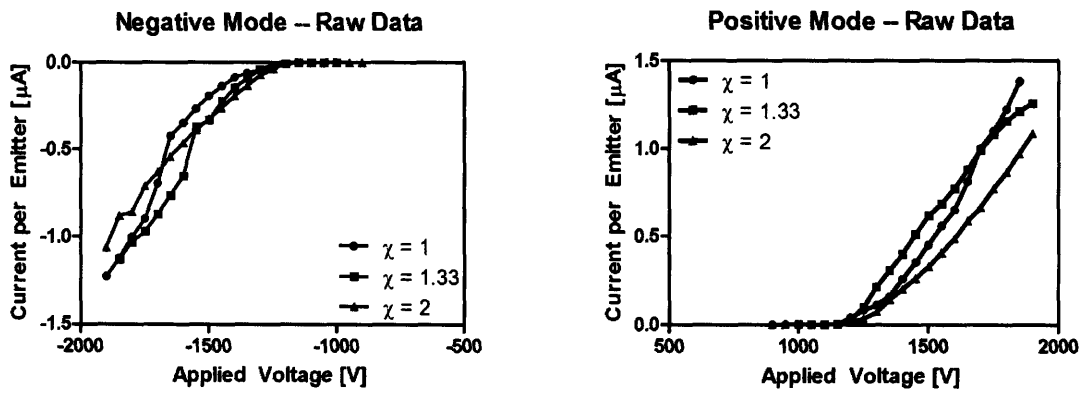

Figure 6-10: Current vs. voltage profiles for three different samples of different linear emitter density (χ) for both positive and negative modes

The characteristic voltage is selected as the voltage required to create an electric field to overcome the surface tension pressure at the emitter tip. The balance pressure is:

$$\frac{1}{2}\epsilon_0 \left(\frac{V^*}{\bar{R}_c}\right)^2 = \gamma\kappa \tag{6.8}$$

Where (κ) is the curvature of the emitter tip and $\bar{R}_c$ is the average radius of curvature, and γ is the surface tension. The curvature is expressed in terms of the two principal radii of curvature (r_{c1},r_{c2}) for the emitter tip:

$$\kappa = \frac{r_{c1} + r_{c2}}{r_{c1} r_{c2}} \tag{6.9}$$

The characteristic voltage is then given as:

$$V^* = \sqrt{\frac{\gamma}{2\epsilon_0}\frac{(r_{c1}+r_{c2})^3}{r_{c1}r_{c2}}} \tag{6.10}$$

The characteristic current is related to the conduction of ions to the base of the ion emission site, which is located at the tip of the emitter. The current that is pulled towards the emission site is equal to:

$$I^* = \sigma A E_l \tag{6.11}$$

Where σ is the conductivity of EMI-BF_4 (1.618 S/m), E_l is the electric field inside the liquid and A is the characteristic area. If we take the area to be a hemispherical control surface, as shown in figure 6-11, then we can write I^* as:

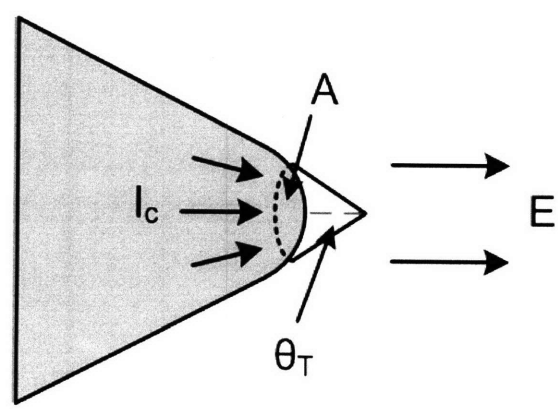

Figure 6-11: Ion transport is modeled as conduction through a control surface located at the tip of the emitter

$$I^* = 2\sigma\pi r_{c1}r_{c2}\left(1 - cos\theta_T\right)\frac{E_0}{\epsilon} \tag{6.12}$$

Where θ_T is taken as the Taylor cone angle (49.29deg), ϵ is the permittivity of EMI-BF_4 (around 100), and E_0 is the electric field at the tip, outside of the liquid.

The electric field at the tip of a single emitter as a function of extractor voltage has been computed using numerical simulation for the three cases. This electric field is then adjusted to account for the close proximity of other emitters. The amount of adjustment necessary is a function of the emitter spacing (d) to emitter-extractor

distance (h), and is computed using numerical simulations. The electric field at the emitter tip when other emitters are far away is equal to the electric field of a single emitter. The electric field when other emitters are very close can be approximated by solving for the electric field of a sheet. In order to find what happens in between, numerical simulations were conducted by varying the d in relation to h. To simplify the analysis, the simulation was two dimensional, using infinitely long pointed sheets, which would approximate the worst case scenario of real 3-dimensional emitters. The result, plotted in Figure 6-12, shows the reduced field over the single emitter field, designated ψ, as a function of h. We see that the field is substantially reduced, for (d/h) ratios under 3. For ratios above 3, the adjacent emitters have little effect on the local electric field at the tip.

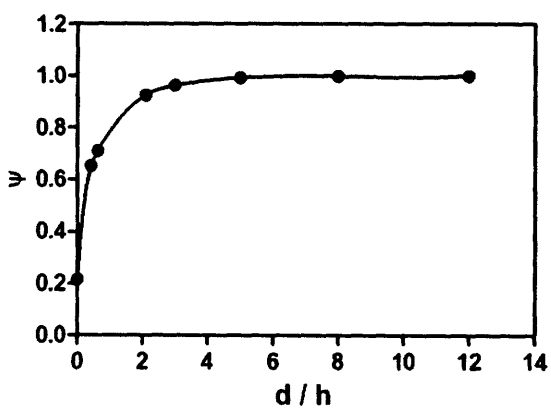

Figure 6-12: The reduced field to single emitter field as a function of emitter separation

The parameters for computing the characteristic current and characteristic voltage, corresponding to the different emitters displayed, are shown in Table 6.4. Included are: the two principal radii of curvature, the field reduction parameter (ψ), and the characteristic voltage (V^*). The characteristic current (I^*) depends on the applied voltage.

Figure 6-13 shows the data plotted using this normalization scheme. We see that in the normalized data is better grouped than the raw data and that we are seeing roughly the same emitted current per emitter as a function of voltage for each

Sample	r_{c1} [μm]	r_{c2} [μm]	ψ	V^* [V]
2	15	4	0.908	580
5	14	5	0.834	537
7	14	4	0.784	551

Table 6.4: 1D Emitter Properties and Non-Dimensionalization Parameters

emitter packing density. This suggests that the emitters can be clustered together to produce more current, and more thrust. It is interesting to note that the normalization scheme seems to have collapsed the results from the two least dense emitter arrays ($\chi = 1, \chi = 1.33$) onto a common line, especially for low currents. The densest array, while it did move closer to the other results with normalization, remains separate and does not collapse neatly onto a common line. It is not clear at this time whether this is just caused by a difference in emitter tip geometry, or if these results signify that the performance of the denser array is fundamentally different. A more detailed study is needed to characterize this effect.

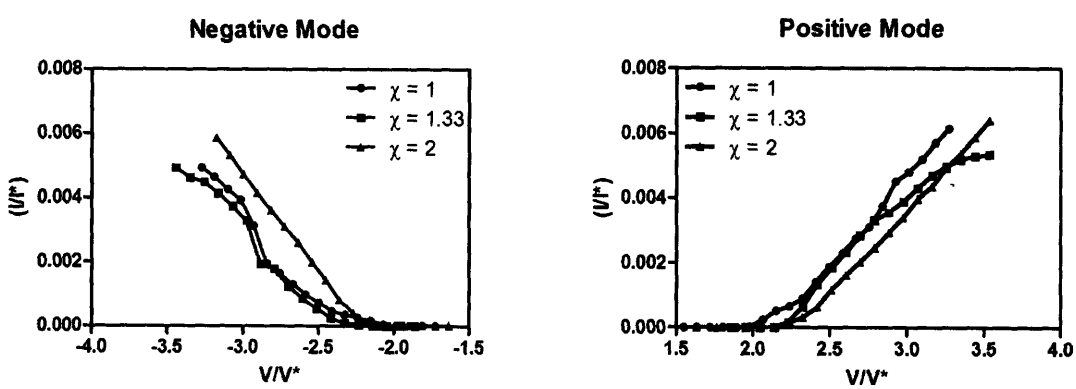

Figure 6-13: Normalized data showing the three emitter arrays with differing packing density (χ)

6.4.3 Long Duration Testing

Extended length tests were also carried out to see if the emitted current would diminish as a function of run duration for the emitters. After an initial decrease in performance attributed to the buildup of ionic liquid on the surface of the emitters near the emission region, most arrays eventually reached a steady state performance. Figure 6-14 shows a characteristic run where the emitted current stays roughly constant over a period of just over 2 hours of continuous operation.

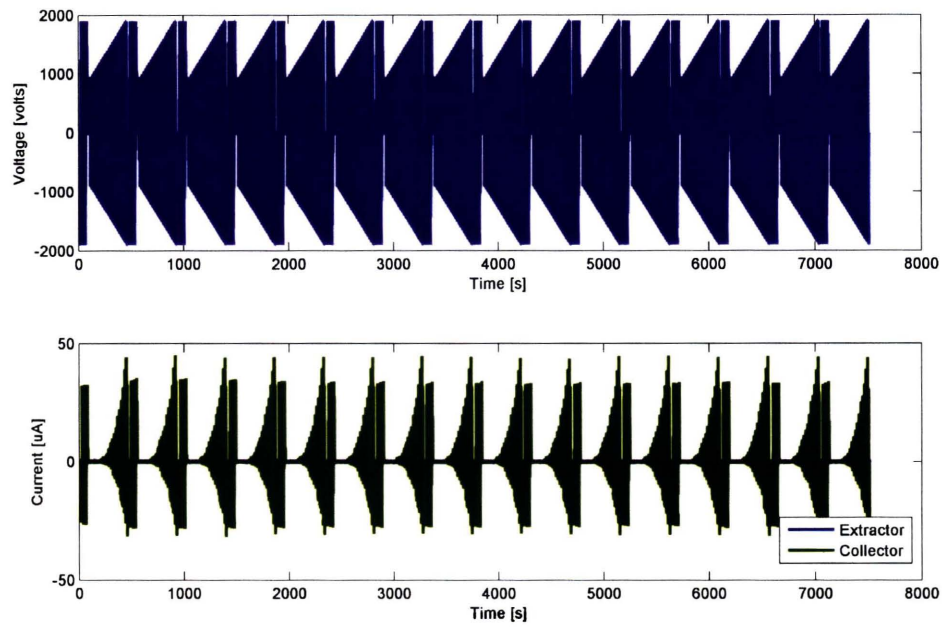

Figure 6-14: 2.1 hour long duration test of an Emitter Array showing the applied voltage profile (top) and the corresponding collected current (bottom)

For some emitter arrays, the amount of emitted current decayed slowly as a function of time as shown in Figure 6-15. These losses amounted to about 30% over the course of 2.3 hours of continuous operation. One possibility is that the ionic liquid is reacting with material left in the bulk porosity after fabrication, and that this is causing a reduction of performance.

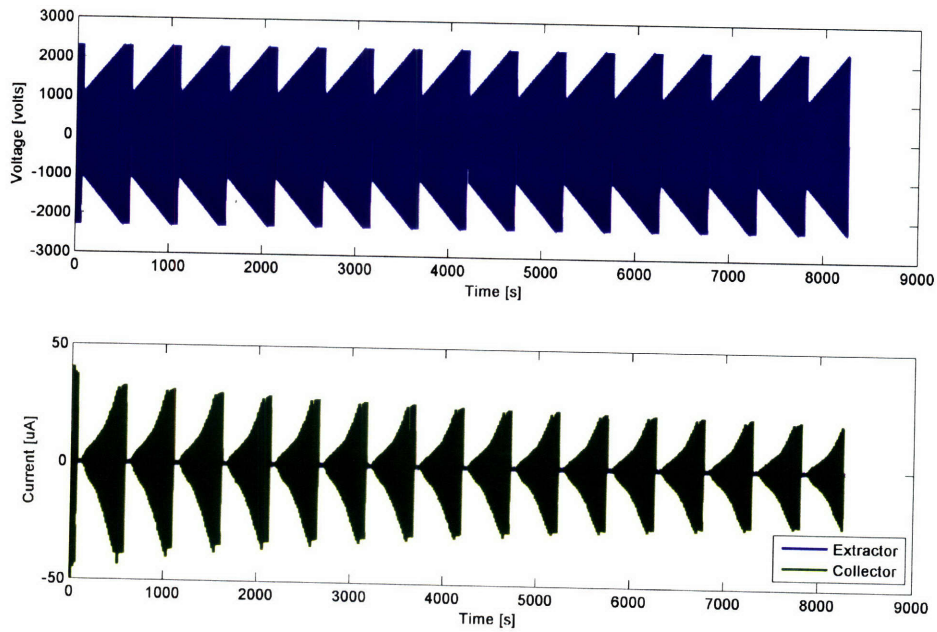

Figure 6-15: 2.3 hour long duration test of an Emitter Array showing the applied voltage profile (top) and the corresponding collected current (bottom), which slowly decays over time

Chapter 7

Conclusions and Future Work

This section will provide an overview of ongoing research concerning the fabrication of two-dimensional emitter arrays and a plan for future research including the characterization of ultra dense two dimensional electrospray arrays. Additionally, comments concerning the improvement of existing fabrication techniques will be discussed and a variety of alternative steps and processes, which have not yet been explored, will also be explained. The section will end with a summary of the thesis and some concluding remarks.

7.1 Two Dimensional Arrays

The fabrication process explained in Chapter 4, was designed so that emitter miniaturization and clustering would be possible. The previous experiments with one dimensional emitter arrays, including the characterization of arrays with different packing densities, showed that performance does not diminish significantly with dense emitter clustering, provided proper extractor designs are implemented. This work paves the way for a new class of ultra dense arrays, capable of increasing the thrust density of electrosprays beyond that of ion or hall thrusters as was seen in Section 1.3.1.

The thruster comprised of three one dimensional emitter arrays, containing a total of 49 emitters (Section 4.6.2), hinted at the future of dense electrospray emitter arrays. However, the difficulty in aligning multiple one dimensional emitter sheets set

a practical limit on the maximum emitter density possible, and subsequently on the total thrust of the device. The logical solution to the miniaturization problem is to fabricate emitters out of plane on a single porous substrate to create two dimensional arrays with automatic emitter to emitter alignment. In this case tolerances would be set by the microfabrication method and not physical alignment between emitters, although emitter-extractor is still an issue. The following sections give an overview of the current status of two dimensional array fabrication as well as some preliminary ideas of the future research required to produce such devices.

7.1.1 Emitter Array Fabrication

The fabrication process for two dimensional arrays is the same as was used earlier with linear arrays, and is specified in detail in Chapter 4. Porous tungsten material (2.54 mm x 19 mm x 19mm) of 0.5 μm porosity was obtained from American Elements and was used as the array substrate. An SEM image of the substrate is shown in Figure 7-1 showing the 0.5 μm porosity. Figure 7-2 shows the two masks used in the initial emitter fabrication experiments, with emitter separations of 300 μm for the left mask and 230 μm for the right mask. This packing density corresponds to a total of 2880 and 5984 emitters for our 19 x 19 mm sample piece.

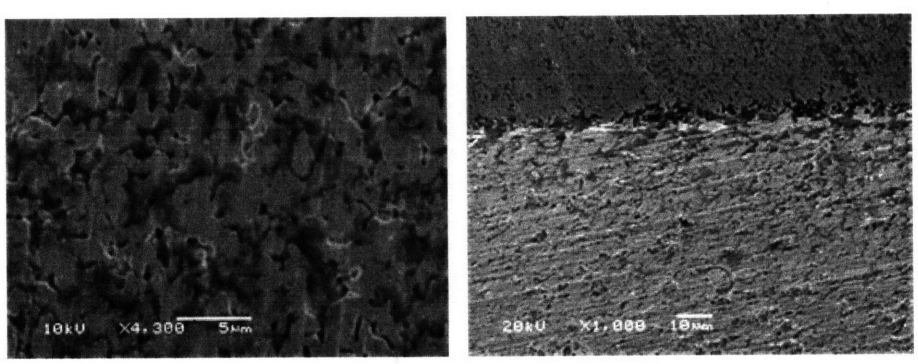

Figure 7-1: 2D Emitter Array Tungsten Media showing the 0.5 μm porosity

The finished polyimide masks, after hardening are shown in Figure 7-3. The polyimide masking layer is approximately 4 μm thick, and provides a very uniform layer on top of the tungsten substrate, with good contact with the tungsten surface.

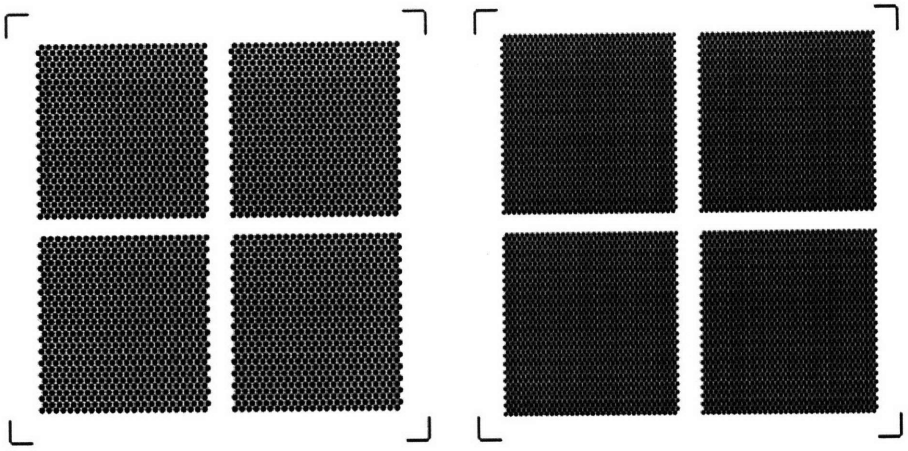

Figure 7-2: Transparency Masks for a Two Dimensional Emitter Array with 2880 emitters (left) and 5984 emitters (right)

This is important since the electrochemical etch is best done in an ultrasonic bath where localized conditions can be quite harsh. In addition, as the emitter geometry forms, the area of tungsten that is in contact with the polyimide layer is reduced, making good contact between the tungsten sample and the polyimide mask essential.

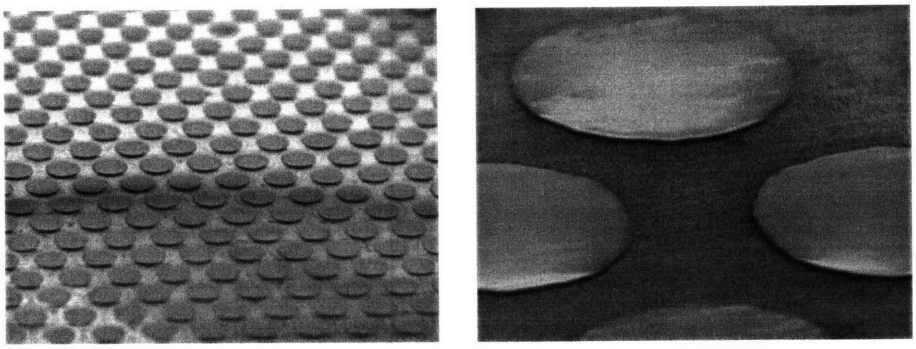

Figure 7-3: Polyimide Masking Layer for a Two Dimensional Emitter Array (300 μm diameter masks)

Initial etching was performed using the flow chamber setup shown in Section 4.4.4. Figure 7-4 shows the polyimide masks on top of the forming emitter at various stages in the etching process.

Figure 7-5 shows the shape evolution of a single emitter with the polyimide mask removed for imaging purposes. During emitter formation, an hourglass shape forms

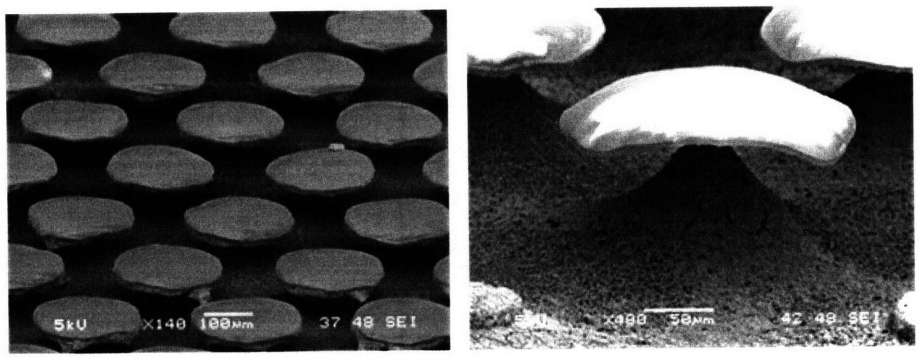

Figure 7-4: Polyimide Masking Layer During Etch Showing and Array of Emitters (left) and a Single Emitter (right)

(Figure 7-5a). As the etching process continues, the neck region diameter is reduced (Figure 7-5b) until a pointed emitter is formed (Figure 7-5c). In this way, emitters with very sharp tips ($R_c < 10\mu$m) are formed. The etching process can be continued further to increase the radius of curvature to the desired value after initial emitter creation. Because many performance aspects of an electrospray emitter depend on the emitter tip geometry, it is important that all emitters in the array have similar geometries, which requires overall etch isotropy (Section 7.2.1).

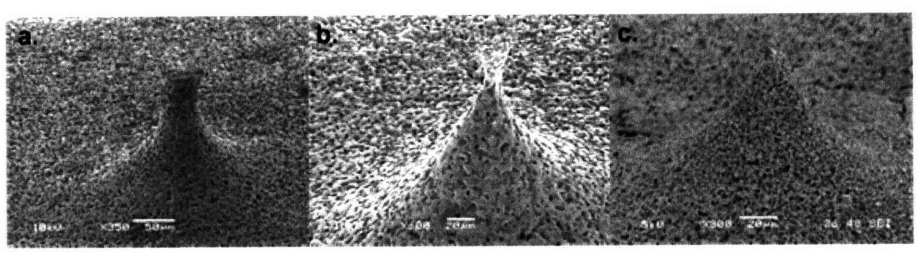

Figure 7-5: 2D Emitter Shape Evolution

Finished emitters in two-dimensional arrays are shown in Figure 7-6. The finished emitters are roughly 100 μm high with a 100 μm base and tip radius of curvatures around 10 μm.

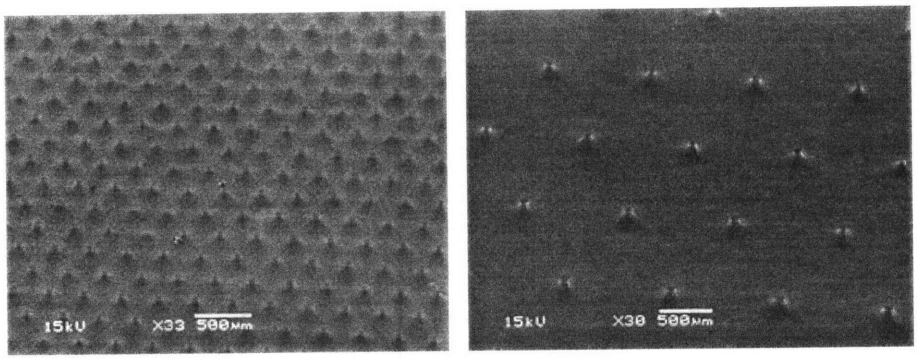

Figure 7-6: Fabricated 2D Emitter Arrays

7.1.2 Initial Extractor Fabrication

As the emitter packing density increases and the emitter separation distances decrease, the emitter to extractor distance must also be reduced to avoid significant electrostatic interactions between emitters to keep the starting voltage low, as was explained in Section 6.4. Additionally, a small emitter to extractor distance reduces beam impingement on the extractor and increases the space-charge limit as was explained in Section 1.3.2. Due to this reduction of the emitter to extractor distance, in addition to the smaller extractor apertures required for for smaller emitters, emitter-extractor alignment becomes very difficult. Because of this difficulty, microfabrication is an ideal way to create extractor aperture arrays with precise alignment between apertures. Additionally, the same fabrication process used to create the emitters can also be used for the extractor.

Solid Tungsten foil, 50.8 μm thick was obtained from ESPI Metals, Inc. and cut into 19 x 19 mm pieces with a diesaw. A polyimide masking layer was created using the same process as was used with emitter fabrication, as outlined in Chapter 4. The transparency masks for the photolithography process corresponding to individual hole emitters (right) and slit emitters (left) are shown in Figure 7-7. Figure 7-8 shows the patterned polyimide layer on the solid tungsten foil for the hole extractor case. Hole emitters are not that much more difficult to align, and they allow for closer emitter packing provided by a staggered triangular emitter grid.

We see that there is variation in the diameter of the mask holes, which will lead

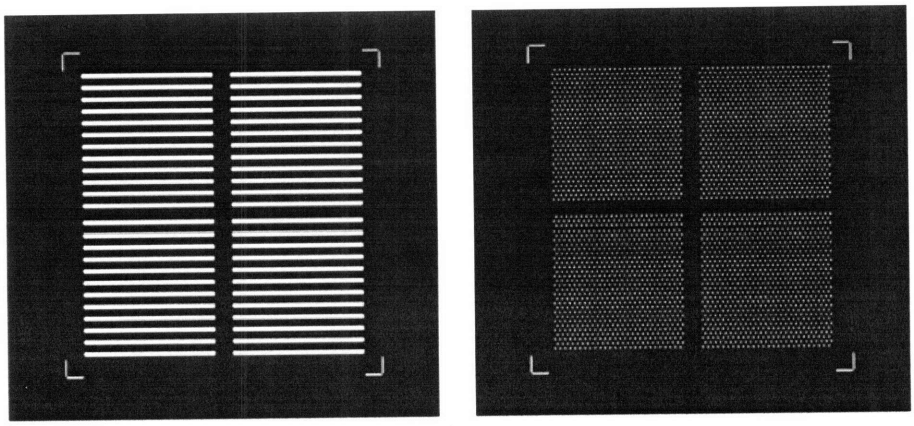

Figure 7-7: Transparency Masks for Slit (left) and Hole (right) Extractors

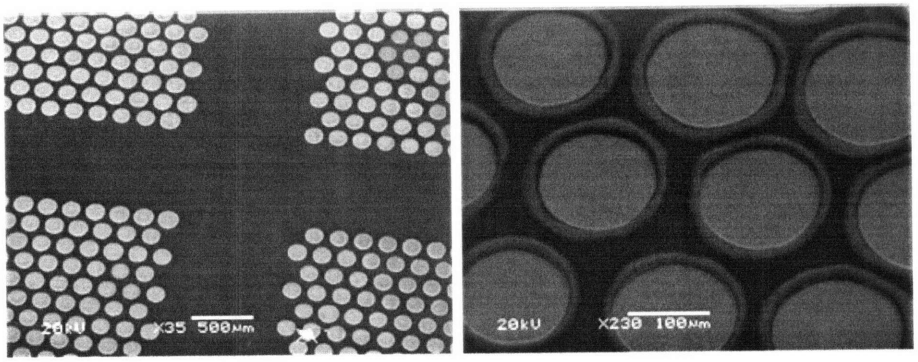

Figure 7-8: Polyimide Masks For Tungsten Extractors

to extractor apertures with varying diameter. Uniformity can be incresed by using thinner layers of polyimide and with shorter UV exposure times for the photolithography process. Figure 7-9 shows the results of some initial etching tests of extractor slits. The incompletely etched samples highlight etch non-uniformity, but if the etching process was allowed to continue, the slits would eventually be created, with only slightly uneven features, due to the smoothing nature of electrochemical etching.

7.1.3 Thruster Concept

This section considers the implementation of a two-dimensional emitter array into a thruster device, complete with fuel storage and packaging. One concept is shown in Figure 7-10, which contains two individual thrusters of 12000 emitters, each in a 42

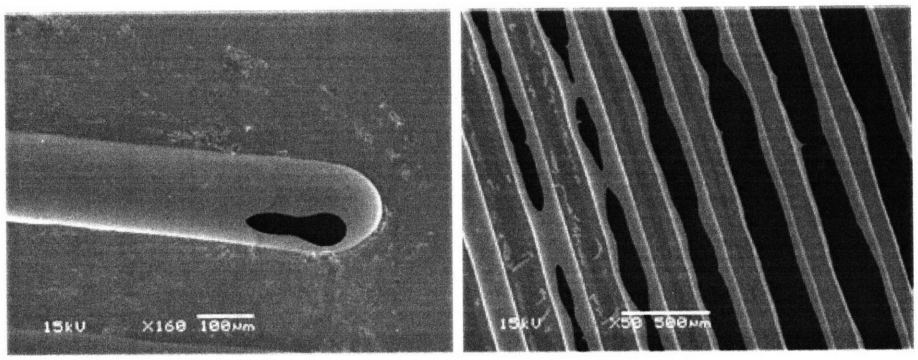

Figure 7-9: Initial Etched Extractor Samples with a Single Slit Extractor (left) and Multiple Slit Extractors of Different Width (right)

x 48 mm area, with emitter separation distances of 230μm. The concept contains the two-dimensional porous Tungsten emitter array, a microfabricated Tungsten hole extractor, a ceramic holder which aligns the extractor to the emitters and provides electrical insulation, and a porous metal fuel tank. The fuel tank has a larger porosity than the emitter array to actively move liquid toward the emitters[31]. For larger thruster designs, this fuel tank could be an empty plenum with one side open to the porous metal emitter array so that the system mass can be reduced, although propellant management devices would then be needed to ensure a high propellant utilization fraction.

The thrusters would be operated in clusters of two, to avoid the need for a dedicated charge neutralization device by having one emit in the positive mode and the other one emit in the negative mode. The thrusters would also need to operate in bipolar mode to avoid electrochemical reactions caused by the charging of the liquid double layer. The period of alternation can be estimated by the following relation:

$$\tau = \frac{C}{I}\Delta V \tag{7.1}$$

Where C is the capacitance of the double layer, ΔV is the maximum voltage difference where reactions will not occur, and I is the emitted current. The capacitance can be written as:

$$C = \frac{\epsilon\epsilon_0 A}{\delta} \tag{7.2}$$

Where A is the area of the liquid - tungsten interface and δ is the double layer thickness which is on the order of 0.5 nm. Assuming the thruster geometry shown in Figure 7-10, a total emitted current of 6 mA, and a double layer voltage difference of 2 V, then the minimum period of oscillation would be around 560 seconds for an average porosity of 0.5 μm. If we operate at an extraction voltage difference of 1900 V with EMI-BF_4, then the specific impulse would be around 4200 s and the thrust would be around 1.2 mN.

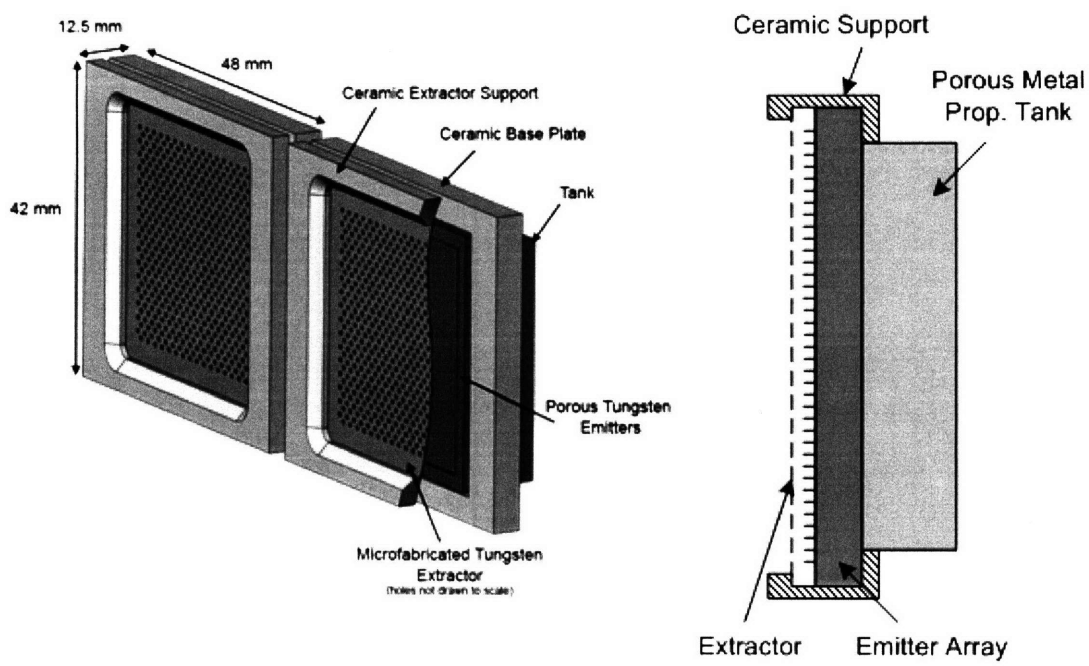

Figure 7-10: 5984 Emitter Thruster Concept.

7.2 Recommendations for Future Work

7.2.1 Emitter Array Fabrication

Further refinements as well as alternative steps should be investigated to improve emitter fabrication. There are two main areas in which further research should be carried out that include: finding a way to prevent material from contaminating and blocking the porosity, and examining the electrochemical etching process to improve emitter uniformity. Additionally, the use of other metals for emitter fabrication and the emitter to extractor alignment needs further research.

Finding alternative methods of blocking the porosity

As was mentioned in Section 4.5, one of the main problems in the current process is that it allows material to get into the porosity of the material. Various methods might be tried in the future to eliminate this problem including: finding a material that will come out of the pores more easily than photoresist, fabricating on a substrate with a solid foil layer on the surface, and creating a solid layer on the surface of the porous tungsten to stop the masking layer from entering the porosity. Figure 7-11 shows what can happen during the etching process if the porosity is contaminated. We see that the polyimide has seeped into the porosity to create extensions onto the surface polyimide masks, which will ultimately lead to non uniform emitters.

- Some materials that would effectively stop the polyimide from entering the porosity and then could be removed completely include materials that could be either boiled or removed by sublimation from the bulk porosity after initial polyimide hardening. One element that could be a candidate for this purpose is iodine. Iodine has a melting point of 386.75 K and a boiling point of 457.56 K at atmospheric pressure[1], although vapor pressures are quite high in both its liquid and solid states (Figure 7-12) and iodine has a strong tendency to evaporate even as a solid. It has a liquid surface tension of 0.054232 N/m at its melting point, and 0.035988 N/m at its boiling point.

  The proposed process flow for the use of iodine is as follows: First, the iodine

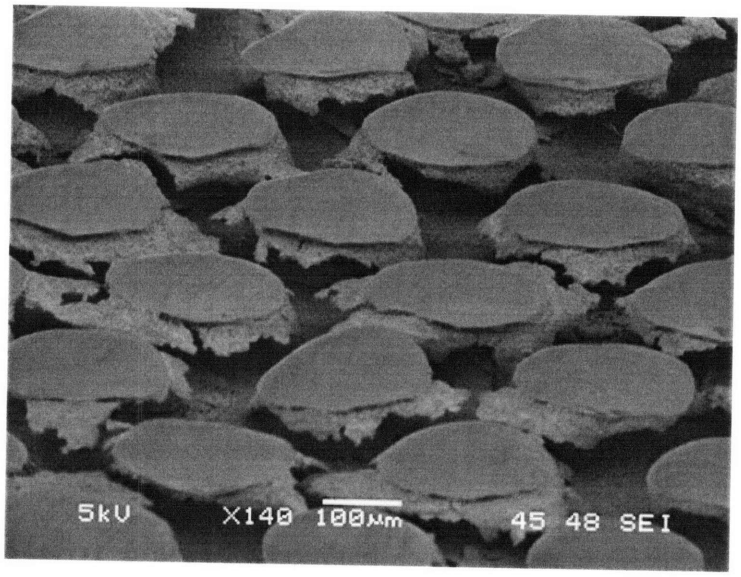

Figure 7-11: Two-Dimensional Array Showing Polyimide Contamination

is allowed to enter the porous tungsten as a liquid and is solidified. The polyimide layer is then spun onto the piece, photolithography is carried out and the polyimide mask is patterned. The iodine is then evaporated from the porosity in vacuum conditions below the vapor pressure of iodine at room temperature. Any leftover traces of iodine are then removed during the polyimide hardening step at 230°C. Some of the problems associated with this scheme are that iodine is a hazardous material to work with, it is very unstable as a liquid and that the polyimide layer and the photoresist developer might have harmful interactions with the iodine.

- Another idea for preventing the polyimide masking layer material from contaminating the pores of the emitter substrate is to have a thin solid layer of tungsten attached to the substrate surface. This would allow the same fabrication process to be utilized and the solid layer would be etched away during the normal electrochemical etch step. Substrates with this geometry could potentially be prepared by modifying the sintering fabrication method as shown in Figure 7-13. The normal sintering method might be able to be used with a thin layer of tungsten foil on one side.

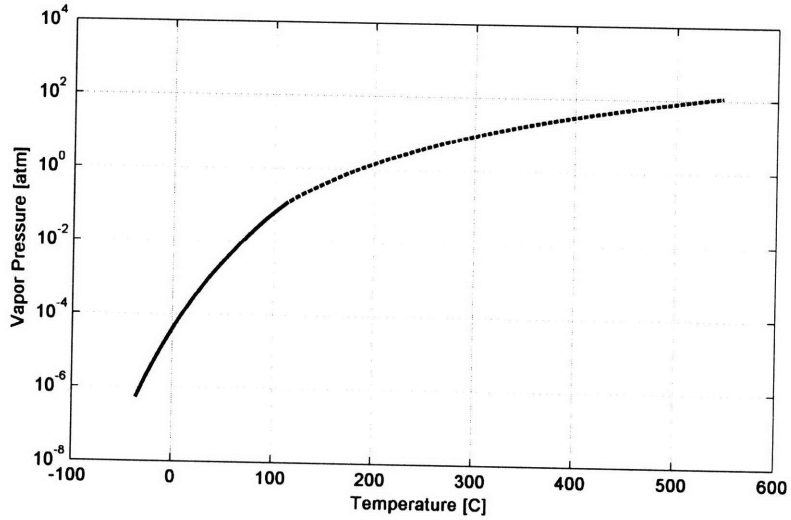

Figure 7-12: Vapor Pressure of Iodine as a Function of Temperature in the Solid State (solid line) and Liquid State (dashed line)

- The most promising idea to solve the problem of porosity contamination is to deposit a layer of Tungsten on the surface of the porous substrate by sputtering. For porosity of 0.5 μm, it would take a sputtering layer of 1-2 μm to adequately cover the porosity to create an effective barrier for the polyimide. It has previously been shown that Tungsten can be deposited by the dc magnetron sputtering process with deposition rates of 10 $\AA/s$ at a target potential of 450 V and a pressure of 10 mTorr[2]. This process has been used to create Tungsten films up to 2000 $\AA$[3], and there should be no problem with increasing this thickness since we are depositing Tungsten on Tungsten and thin film stresses should not be an issue. At this deposition rate, it would take roughly 33 minutes to create a layer of 2μm.

Improving Emitter to Emitter Uniformity

The uniformity of the electrochemical etching step is essential to creating arrays of emitters with the same geometrical dimensions. Emitters need to have similar length and tip geometry in order to have a common operating performance. As we have seen for the one dimensional arrays in Section 4 and the two-dimensional arrays

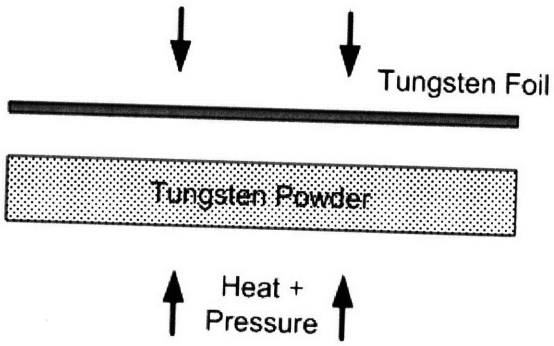

Figure 7-13: Modified Sintering Process to Eliminate Substrate Pore Contamination

in Section 7.1, there are significant non-uniformities in the current process. It is hypothesized that this is primarily caused by contamination in the bulk from either residual photoresist or polyimide, although the etching process itself may introduce small non-uniformities. Figure 7-14 shows an example of an emitter array where some areas etched faster than others, leaving some emitters intact while etching away others that had formed at earlier times.

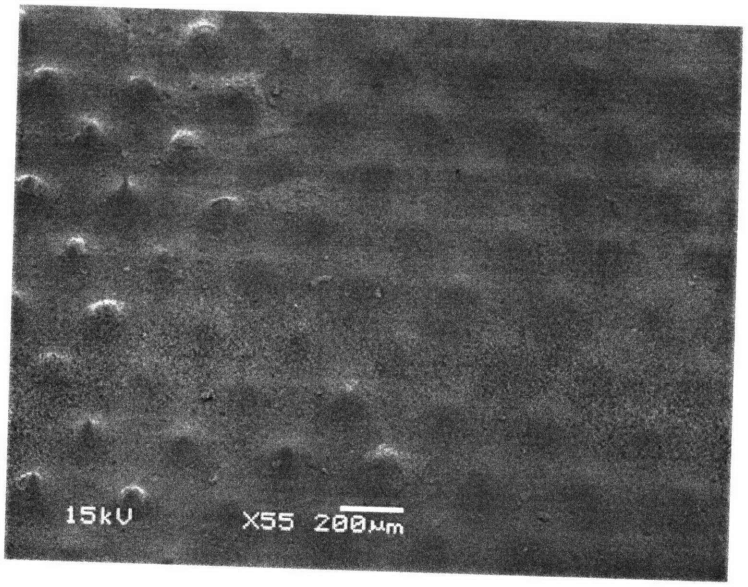

Figure 7-14: Two-Dimensional Array Showing a Non-Uniform Etch

Various changes to the etching process have been experimented with to increase uniformity including: implementing an electrochemical flow cell, performing the etch

in an ultrasonic bath to remove local contamination on the surface.

7.2.2 Other Suggested Research Areas

<u>Thruster Fabrication</u>

- Fabrication of Emitters on other porous metals including Titanium
- Extractor to emitter alignment methods for dense arrays

<u>Thruster Characterization</u>

- Characterize the performance of porous metal electrospray sources with heavier ionic liquids[18]

  Time-of-flight, RPA

- Conduct RPA analysis to verify that the beam potential is similar to the applied potential
- Characterize the spreading of the beam
- Investigate the role of fluid transport on the maximum current emission
- Long duration testing with polarity alternation

7.3 Conclusion

Porous metal electrospray sources have great promise in the future of space propulsion. It has been shown that passively-fed porous electrospray emitters can produce more current and hence more thrust than a traditional externally wetted needle emitter. Porous metal electrospray emitters also have been shown to emit in the ionic regime with little or no droplet emission as opposed to traditional capillary sources, with operation at room temperature. The devices can be set for a wide range (1000 to 5000+ s) of specific impulses to suit specific missions by introducing an accelerator electrode.

Methods of fabricating miniaturized arrays of emitters have been developed which allow for dense clustering of emitters which will ultimately allow for significant increases in the current density and thrust density of electrospray devices. It has been shown that for modest miniaturization, thrust densities comparable to conventional electric propulsion devices (Hall, Ion) can be achieved with significant decreases in the total thruster footprint on the spacecraft (roughly 100X less mass and 20-100X less volume). A device containing 49 emitters was assembled and characterized to display the technology. The device was found to emit around 1 - 1.5 μA per emitter with a maximum measured thrust of 5 μN. Further work is ongoing to dramatically increase emitter density with two-dimensional emitter arrays.

A primary advantage of miniaturized electrospray emitter clusters is that they can be scaled to suit specific spacecraft missions. Assuming that the thrust density is on the order of a Hall or Ion device, the electrospray thruster can be comprised of as many or as few emitters, giving wide flexibility on thrust levels and thruster footprint, while maintaining the same overall system efficiency. Hall and Ion devices cannot be scaled easily to suit smaller satellites, and leave a much large footprint on spacecraft than electrospray arrays. The devices also have advantages over FEEP devices because they can operate at room temperature and operate at much lower extraction voltages which simplifies the power supply system.

Further research needs to be conducted, as was mentioned earlier in this section, to make this technology feasible for space applications. However, microfabricated electrospray sources show great promise as an alternative to conventional space propulsion devices.

Bibliography

[1] Design institute for physical properties, sponsored by aiche dippr project 801 - full version. design institute for physical property data/aiche. *Knovel.*

[2] M.O. Aboelfotoh. Electrical characteristics of w-si(100) schottky barrier junctions. *J. Appl. Phys*, 66(1):262–272, July 1989.

[3] M.O. Aboelfotoh. Temperature dependance of the schottky-barrier height of tungsten on n-type and p-type silicon. *Solid-State Electronics*, 34(1):51–55, 1991.

[4] Karen LeCompte Alan B. McEwen, Helen L. Ngo and Jay Goldman. Electrochemical properties of imidazolium salt electrolytes for electrochemical capacitor applications. *J. Electrochem. Soc.*, 146(5):1687–1695, 1999.

[5] Matthew S. Alexander, John Stark, and Katharine L. Smith. Electrospray performance of microfabricated colloid thruster arrays. *Journal of Propulsion and Power*, 22(3):620–627, 2006.

[6] Adrian G. Bailey. Investigation of a single spraying site of a colloid thruster. *J. Phys. D: Appl. Phys., Vol. 6, 1973.*

[7] M.N.W. Groenendijk F. Tardaguila R.J. Koopmans J. Boscher B.T.C. Zandbergen, M.C. Louwerse and J.L.P.A. Moerel. Initial development of a miniature cold gas propulsion system for nano/micro-satellites. 5th *Space Propulsion Conference*, May 2008.

[8] J. Fernandez de la Mora C. Larriba, S. Castro and Paulo Lozano. Monoenergetic source of kilodalton ions from taylor cones of ionic liquids. *Journal of Applied Physics*, 101, April 2007.

[9] Weiwei Deng, James F. Klemic, Xiaohui Li, Mark A. Reed, and Alessandro Gomez. Liquid fuel microcombustor using microfabricated multiplexed electrospray sources. *Proceedings of the Combustion Institute*, 31.

[10] Weiwei Deng, James F. Klemic, Xiaohui Li, Mark A. Reed, and Alessandro Gomez. Increase of electrospray throughput using multiplexed microfabricated sources for the scalable generation of monodisperse droplets. *J. Aerosol Sci.*, 37:696714, 2006.

[11] A.G. Fedorov and F.L. Degertekin. Scanning mass spectrometry probe for biochemical imaging. *Electronics Letters*, 42(14), 2006.

[12] J.B. Fenn, M. Mann, C.K. Meng, S.F. Wong, and C.F. Whitehouse. Electrospray ionization for mass spectrometry of large biomolecules. *Science*, 246.

[13] M. Gamero-Castaño. A torsional balance for the characterization of micronewton thrusters. *Review of Scientific Instruments*, 74(10):4519–4514, October 2003.

[14] Blaise Gassend. A fully microfabricated two-dimensional electrospray array with applications to space propulsion. *MIT Doctoral Thesis*, 2007.

[15] Ronald W. Humble, Gary N. Henry, and Wiley J. Larson. *Space Propulsion Analysis and Design.* McGraw-Hill, 1995.

[16] A. Jaworek. Electrospray droplet sources for thin film deposition. *J Mater Sci*, 42:266297, 2007.

[17] Richard T. Carlin Joan Fuller and Robert A. Osteryoung. The room temperature ionic liquid 1-ethyl-3-ethylimidazolium tetrafluoroborate: Electrochemical couples and physical properties. *J. Electrochem. Soc.*, 144(11), November 1997.

[18] Robert S. Legge Jr. and Paulo Lozano. Performance of heavy ionic liquids with porous metal electrospray emitters, to be presented. 44th *AIAA/ASME/SAE/ASEE Joint Propulsion Conference Exhibit*, July 2008.

[19] R. Kometani, T. Morita, K. Watanabe, K. Kanda, Y. Haruyama, T. Kaito, J. Juita, M. Ishida, Y. Ochiai, and S. Matsui. Nozzle-nanostructure fabrication on glass capillary by focused-ion-beam chemical vapor deposition and etching. *Japan. J. Appl. Phys.*, 42:4107–4110, 2003.

[20] D. Landolt, P.F. Chauvy, and O. Zinger. Electrochemical micromachining, polishing and surface structuring of metals: fundamental aspects and new developments. *Electrochimica Acta*, (48):3185–3201, 2003.

[21] Dieter Landolt. Flow channel cell apparatus for high rate electrolysis studies. *The Review of Scientific Instruments*, 43(4), April 1972.

[22] Erik Lassner and Wolf-Deiter Schubert. *Tungsten: Properties, Chemistry, Technology of the Element, Alloys and Chemical Compounds.* Kluwer Academic/Plenum Publishers, 1998.

[23] Robert S. Legge and Paulo Lozano. Maximizing one-dimensional porous emitter packing density for electrospray applications. 5th *Space Propulsion Conference*, (121), May 2008.

[24] Robert S. Legge, Paulo C. Lozano, and Manuel Martinez-Sanchez. Fabrication and characterization of porous metal emitters for electrospray thrusters. 30th *International Electric Propulsion Conference.*

[25] Young-Mo Lim and Soo Hyung Kim. An electrochemical fabrication method for extremely thin cylindrical micropin. *International Journal of Machine Tools & Manufacture*, (41):22872296, 2001.

[26] Carol Livermore and Joel Voldman. 6.777 class notes. MIT Spring 2007.

[27] I. G. Loscertales and J. Fernandez de la Mora. 0. piotrowski, c. madore, and d. landoit. *J. Chem. Phys.*, 103(12):5041–5060, 1998.

[28] Paulo Lozano. Studies on the ion-droplet mixed regime in colloid thrusters. *MIT Doctoral Thesis*, 2003.

[29] Paulo Lozano. Energy properties of an emi-im ionic liquid ion source. *Journal of Physics D: Applied Physics*, 39(1):126–134, January 2006.

[30] Paulo Lozano, Benjamin Glass, and Manuel Martinez-Sanchez. Performance characteristics of a linear ionic liquid electrospray thruster. 29th *International Electric Propulsion Conference*, (192), 2005.

[31] Paulo Lozano and Robert S. Legge Jr. Porous metal electrospray emitter. *Provisional Patent Application #61050847*, 2008.

[32] Paulo Lozano and Manuel Martinez-Sanchez. Ionic liquid ion sources: Suppression of electrochemical reactions using voltage alternation. *Journal of Colloid and Interface Science*, (280):149–154, 2004.

[33] Paulo Lozano and Manuel Martinez-Sanchez. Efficiency estimation of emi-bf_4 ionic liquid electrospray thrusters. *41st AIAA/ASME/SAE/ASEE Joint Conference and Exhibit*, July 2005.

[34] Paulo Lozano and Manuel Martinez-Sanchez. Ionic liquid ion sources: characterization of externally wetted emitters. *Journal of Colloid and Interface Science*, (282):415–421, 2005.

[35] C. Madore, O. Piotrowski, and D. Landolt. Through-mask electrochemical micromachining of titanium. *Journal of The Electrochemical Society*, 146(7):2526–2532, 1999.

[36] Manuel Martinez-Sanchez. 16.522 class notes. MIT Spring 2007.

[37] Manuel Martinez-Sanchez and J.E. Pollard. Spacecraft electric propulsion-an overview. *Journal of Propulsion and Power.*

[38] J.B. Mathieu and Dieter Landolt. Electropolishing of titanium in perchloric acid-acetic acid solution. *J. Electrochem. Soc.*, 125(7):1044–1049, 1978.

[39] J. Fernandez De La Mora and I.G. Loscertales. Current emitted by highly conducting taylor cones. *Journal of Fluid Mechanics*, 260:155–184, 1994.

[40] Pradyot Patnaik. *Deans Analytical Chemistry Handbook.* McGraw-Hill, 2004.

[41] E. Raub and K. Mueller. *Fundamentals of Electro Deposition.* Elsevier Publishing Company, 1963.

[42] I. Romero-Sanz, R. Bocanegra, M. Gamero-Castaño, and J. Fernandez de la Mora. Source of heavy molecular ions based on taylor cones of ionic liquids operating in the pure ion evaporation regime. *Journal of Applied Physics*, 94(5):3599–3601, September 2003.

[43] Stephen D. Senturia. *Microsystem Design.* Springer Science and Business Media, Inc, 2001.

[44] JaeKon Choi SungCheal Moon and Richard J. Farris. Preparation of aligned polyetherimide fiber by electrospinning. *Journal of Applied Polymer Science*, 109:691694, April 2008.

[45] George P. Sutton and Oscar Biblarz. *Rocket Propulsion Elements, Seventh Edition.* John Wiley and Sons, INC, 2001.

[46] G.I. Taylor. Disintegration of water drops in an electric field. *Proceedings of the Royal Society of London*, 280.

[47] Kirt R. Williams, Kishan Gupta, and Matthew Wasilik. Etch rates for micromachining processes - part ii. *Journal of Microelectromechanical Systems*, 12(6):761–778, December 2003.

[48] John Zeleny. The electrical discharge from liquid points, and a hydrostatic method of measuring the electric intensity at their surfaces. *The Physical Review 3.*